NASA/TM–2006–214147

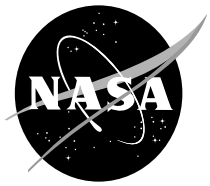

BOUSSOLE: A Joint CNRS-INSU, ESA, CNES, and NASA Ocean Color Calibration and Validation Activity

David Antoine, Malik Chami, Hervé Claustre, Fabrizio d'Ortenzio, André Morel, Guislain Bécu, Bernard Gentili, Francis Louis, Joséphine Ras, Emmanuel Roussier, Alec J. Scott, Dominique Tailliez, Stanford B. Hooker, Pierre Guevel, Jean-François Desté, Cyril Dempsey, and Darrell Adams

December 2006

The NASA STI Program Office … in Profile

Since its founding, NASA has been dedicated to the advancement of aeronautics and space science. The NASA Scientific and Technical Information (STI) Program Office plays a key part in helping NASA maintain this important role.

The NASA STI Program Office is operated by Langley Research Center, the lead center for NASA's scientific and technical information. The NASA STI Program Office provides access to the NASA STI Database, the largest collection of aeronautical and space science STI in the world. The Program Office is also NASA's institutional mechanism for disseminating the results of its research and development activities. These results are published by NASA in the NASA STI Report Series, which includes the following report types:

- TECHNICAL PUBLICATION. Reports of completed research or a major significant phase of research that present the results of NASA programs and include extensive data or theoretical analysis. Includes compilations of significant scientific and technical data and information deemed to be of continuing reference value. NASA's counterpart of peer-reviewed formal professional papers but has less stringent limitations on manuscript length and extent of graphic presentations.
- TECHNICAL MEMORANDUM. Scientific and technical findings that are preliminary or of specialized interest, e.g., quick release reports, working papers, and bibliographies that contain minimal annotation. Does not contain extensive analysis.
- CONTRACTOR REPORT. Scientific and technical findings by NASA-sponsored contractors and grantees.
- CONFERENCE PUBLICATION. Collected papers from scientific and technical conferences, symposia, seminars, or other meetings sponsored or cosponsored by NASA.
- SPECIAL PUBLICATION. Scientific, technical, or historical information from NASA programs, projects, and mission, often concerned with subjects having substantial public interest.
- TECHNICAL TRANSLATION. English-language translations of foreign scientific and technical material pertinent to NASA's mission.

Specialized services that complement the STI Program Office's diverse offerings include creating custom thesauri, building customized databases, organizing and publishing research results . . . even providing videos.

For more information about the NASA STI Program Office, see the following:

- Access the NASA STI Program Home Page at http://www.sti.nasa.gov/STI-homepage.html
- E-mail your question via the Internet to help@sti.nasa.gov
- Fax your question to the NASA Access Help Desk at (301) 621-0134
- Telephone the NASA Access Help Desk at (301) 621-0390
- Write to:
  NASA Access Help Desk
  NASA Center for AeroSpace Information
  7115 Standard Drive
  Hanover, MD 21076–1320

NASA/TM–2006–214147

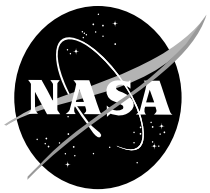

BOUSSOLE: A Joint CNRS-INSU, ESA, CNES, and NASA Ocean Color Calibration and Validation Activity

David Antoine, Malik Chami, Hervé Claustre, Fabrizio d'Ortenzio, André Morel, Guislain Bécu, Bernard Gentili, Francis Louis, Joséphine Ras, Emmanuel Roussier, Alec J. Scott, and Dominique Tailliez
Laboratoire d'Océanographie de Villefranche, Villefranche-sur-Mer, France

Stanford B. Hooker
NASA Goddard Space Flight Center, Greenbelt, Maryland

Pierre Guevel and Jean-François Desté
ACRI-in, Sophia Antipolis, France

Cyril Dempsey and Darrell Adams
Satlantic, Inc., Halifax, Canada

National Aeronautics and
Space Administration

Goddard Space Flight Center
Greenbelt, Maryland 20771

December 2006

Available from:

NASA Center for AeroSpace Information
7115 Standard Drive
Hanover, MD 21076-1320

National Technical Information Service
5285 Port Royal Road
Springfield, VA 22161

Preface

The *Bouée pour l'acquisition de Séries Optiques à Long Terme* (BOUSSOLE) Project is a continuous activity, which evolves over time to deal with the multitude of activities associated with long-term oceanic deployments. This report is to be seen as a snapshot of the present state of the activity and achievements[1]. An overview of the different technical aspects is provided; it is out of the scope of this report to provide all details of all activities. It is directed at providing basic information that is needed for an overall understanding of what has been done and what is presently being done in all segments of the project. More detailed analyses of specific technical aspects of the project will be the subject of other, more detailed, reports. BOUSSOLE is a joint effort involving multiple organizations, which are combining the work of a lot of people, and is funded and supported by the following agencies and academic or governmental institutes:

- *Centre National de la Recherche Scientifique*[2] (CNRS),
- *Institut National des Sciences de l'Univers*[3] (INSU),
- European Space Agency (ESA),
- *Centre National d'Etudes Spatiales*[4] (CNES),
- National Aeronautics and Space Administration (NASA),
- *Université Pierre et Marie Curie*[5] (UPMC), and
- *Observatoire Océanologique de Villefranche-sur-Mer*[6].

The resources these organizations have provided were critical in establishing BOUSSOLE as a field site for ocean color calibration and validation activities, but they were not the only ones who needed to cooperate. Indeed, a very important *participant* was never consulted, but luckily, decided to send a representative anyway. Before entering into the details of this technical report, it seems appropriate to add this silent partner to the introductions provided here, particularly because the task for this recently hired team member is to remain on site day and night to survey the mooring and provide daily status reports. After this page is turned, hopefully the revulsion of isolating a team member in the unforgiving environment of the open sea will be replaced with an appreciation for the beauty of submarine life and the largely unseen world oceanographers strive to understand. Incidentally, this is also recognition of the vital and hard work the technical staff associated with BOUSSOLE are continuously doing at sea. And, who knows, maybe you will meet this new staff member the next time you are at sea. This might very well reassure you—a scientist or engineer inevitably focused too much on the problem at hand (our common fate)—that you still possess an open mind capable of seeing what is happening around you and being pleasantly surprised by what is revealed as the layers of a problem are peeled away ...

[1] Additional details are available on the BOUSSOLE Web site `http://www.obs-vlfr.fr/Boussole`.

[2] National Center for Scientific Research

[3] National Institute for Science of the Universe

[4] National Center for Space Studies

[5] University of Pierre and Marie Curie

[6] Oceanographic Observatory of Villefranche

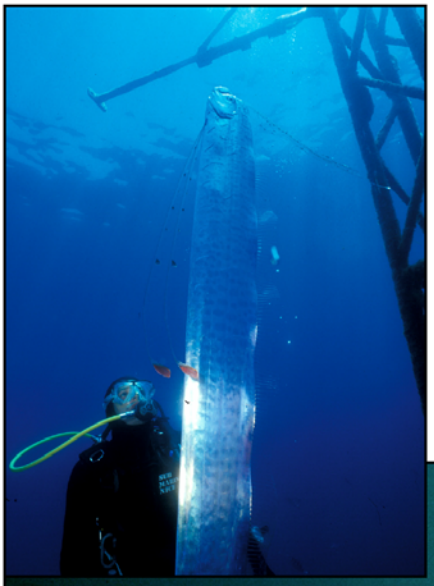

This is the regalec, or as it is also known, the *oarfish*, king of the herring, or ribbonfish (actually *Regalecus glesne*). The oarfish is a widely-distributed marine fish having a slender silvery body up to 11 m (36 ft) in length, a dorsal fin running the entire length of the body with red-tipped anterior rays rising above the head, and ventral fins reduced to long filaments. It swims by rhythmically undulating the dorsal fin (a motion resembling that of a snake), while keeping the body itself straight. It's large size and snake-like appearance is believed to be the source of ancient mariner tales of sea serpents. The specimen—or rather, *team member*—shown here is about 4 m long. The oarfish is rarely observed *in situ*, but this one exhibits a keen interest in the status of the BOUSSOLE buoy.

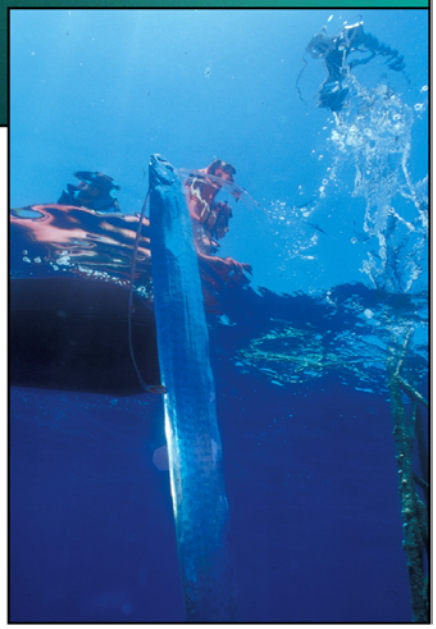

Note also the clarity of the seawater at the BOUSSOLE site. The details of the in-water superstructure and one of the support arms where the in-water instruments are mounted (Sect. 5.2) are clearly visible in the top-left picture, whereas in the bottom-right picture, two of the divers in their small service boat and the above-water part of the upper superstructure are easily discerned. Oarfish, like this one, have been observed swimming in a vertical orientation, with their long axis perpendicular to the ocean surface. In this posture, the downstreaming light silhouettes prey, making them easier to spot.

Photographs: David Luquet, *Observatoire Océanologique de Villefranche-sur-Mer*

Abstract

This report presents the *Bouée pour l'acquisition de Séries Optiques à Long Terme* (BOUSSOLE) project, the primary objectives of which are to provide a long-term time series of optical properties in support of a) calibration and validation activities associated with satellite ocean color missions, and b) bio-optical research in oceanic waters. The report starts with an introduction to the rationale for the establishing the project, including a definition of vicarious calibration and the specific requirements that are attached to it. The organization of the project is presented, and the characteristics of the measurement site, which is located in the northwestern Mediterranean Sea, are discussed. A qualitative overview of the collected data are provided, followed by some details about the new type of buoy that has been specifically designed and built for this project. Then, the data collection protocols, as well as the data processing techniques, are presented. The report continues with a quantitative summary of the collected data, as well as with a discussion of some sample results, including match-up analyses for the currently operational ocean color sensors, namely the Medium Resolution Imaging Spectrometer (MERIS), the Sea-viewing Wide Field-of-view Sensor (SeaWiFS), and the Moderate Resolution Imaging Spectroradiometer (MODIS). Finally, preliminary results of the vicarious radiometric calibration of MERIS are presented, including a tentative uncertainty budget. The results of this match-up analysis are in agreement with similar experiments carried out on other sites, and they allow a comparison of the performance of various ocean color sensors to be performed. They ultimately demonstrate the ability of the BOUSSOLE activity, which is combining a dedicated platform and commercial-off-the-shelf instrumentation, to provide data qualified to monitor the quality of ocean color products on the long term.

1. INTRODUCTION

A prerequisite to building a long-term (decadal) archive of ocean color, in response to the need for assessing the response of the oceanic biota to climatic changes, is to accurately calibrate the top-of-atmosphere (TOA) satellite observations, then to validate the surface geophysical parameters derived from these observations, and finally to develop and maintain this capability over long periods of time. Ensuring coherence between the geophysical products derived from different sensors is also an important aspect to consider.

When ocean color observations from different remote sensors are considered as part of the task of data merging, their intercalibration and validation might be facilitated if it could be *anchored* on continuous long-term *in situ* stations, as recommended by the International Ocean Color Coordinating Group (IOCCG 1999). Deploying and maintaining moorings or other types of fixed stations that operate in a continuous way is, however, a difficult proposition. Successful examples are provided by the Marine Optical Buoy (MOBY) program (Clark et al. 1997 and 2003), which has maintained an optical mooring near Hawaii since 1995, and by the Coastal Atmosphere and Sea Time Series (CoASTS) project maintained near Venice (Italy) since 1995 (Berthon et al. 2002 and Zibordi et al. 2002a).

In response to these concerns, a project was started in 2000 with the objective of establishing a time series of optical properties in oceanic waters to support the calibration and validation of ocean color satellite sensors. This activity has been named the *Bouée pour l'acquisition de Séries Optiques à Long Terme*† (BOUSSOLE) Project. This report is an attempt to provide the necessary basic information so that the rationale of the project and the various activities that are carried out are properly documented.

1.1 General Objectives

A new type of buoy has been specifically designed for the acquisition of radiometric quantities, and has been deployed in the Mediterranean Sea between the French Riviera coast and Corsica. One general objective is to perform match-up analyses and vicarious calibration experiments for ocean color satellite sensors, based on the data set that is being built from this new buoy. The primary objective of the first deployment, which took place in July 2000 and lasted for three months, was to validate the mooring concept. The first operational data collection occurred in May 2002, but the entire buoy was lost because of a flaw in the construction of the primary flotation sphere. A redesigned buoy was deployed at the beginning of September 2003, which resulted in three months of successful data collection. In 4 March 2004, a third data collection sequence was begun and lasted until July 2004, when a rotation of the buoy upper superstructure (i.e., the one that hosts instrumentation) was carried out. Then, the data collection continued until June 2005, when a rotation of the entire

† Literally translated from French as the "buoy for the acquisition of a long-term optical series." "*Boussole*" is the French word for "compass."

buoy and mooring line was accomplished. This was actually the beginning of a nearly uninterrupted succession of deployments.

Another objective of the BOUSSOLE activity is to perform vicarious calibration experiments. They should allow the TOA radiance to be simulated and compared to the satellite measurements, in particular for the European Medium Resolution Imaging Spectrometer (MERIS) sensor (Rast et al. 1999). In this way, the need for a change in the preflight calibration coefficients for a given sensor might be evaluated, and its amount quantified. From this data set, match-up analyses shall be also possible for chlorophyll *a* (Chl *a*) concentration and water-leaving radiances, as well as algorithm evaluation (atmospheric correction and pigment retrieval). Because of a certain commonality in the band sets of the new generation of ocean color sensors, the data acquired with the buoy might be used for several of these sensors, and then contribute to the international effort of intercalibrating them and of cross-validating their products, which were amongst the basic goals of the Sensor Intercomparison for Marine Biological and Interdisciplinary Ocean Studies (SIMBIOS) project (McClain 1998). In addition, some protocol issues (measurements) are specifically linked to the use of buoys, while others, of general concern to marine optics measurements, may find specific answers when buoys are used. These aspects are examined, which, to the best of the project knowledge, have not been thoroughly investigated up to now.

In parallel to these *operational* objectives (i.e., the calibration and validation activities), the assembled data set will be used for more fundamental studies in marine optics and bio-optics. Among the questions and topics that might be addressed are the diurnal cycles of optical properties, the response to abrupt environmental changes (storms and so-called *red rain* events), the relationships between chlorophyll concentration and the inherent optical properties, the role of a fluctuating interface in establishing the radiative regime, the bidirectionality of the radiance field, the annual cycles and interannual variations of the optical properties, the use of these properties as indicators of other biogeochemical properties, and the interpretation of the natural fluorescence signal.

1.2 Vicarious Calibration

The need to vicariously calibrate an ocean color satellite sensor was first demonstrated for the Coastal Zone Color Scanner (CZCS), which was a proof-of-concept mission with an operational capability spanning 1979–1986. On one hand, this instrument was not equipped with the necessary onboard devices for the monitoring of the long-term degradation of the instrument response sensitivity (internal lamps suffered a rapid degradation), and, on the other hand, the mission did not include an extensive vicarious calibration program. In the end, the calibration of the CZCS was never based on a robust scientific capability and has never been sufficiently confirmed.

The converse situation is illustrated by the Sea-viewing Wide Field-of-view Sensor (SeaWiFS) mission (Hooker et al. 1992). The instrument is equipped with a solar diffuser and has the capability of viewing the full moon, both of which are used to track the temporal stability of the instrument; and, in addition, an extensive vicarious calibration and algorithm validation program was set up prior to launch (McClain et al. 1992). The vicarious calibration portion of the latter is based on the deployment of a permanent optical buoy, the MOBY program (Clark et al. 1997), which is moored in Case-1 waters near the island of Lanai in Hawaii. In parallel to this central and key element, extensive campaigns are conducted around the world ocean, in order to collect radiometric measurements and ancillary data in a variety of environments (e.g., Robins et al. 1996, Aiken et al. 1998, and Barlow et al. 2003). These data are used to permanently evaluate the quality of the level-2 products and improve, whenever possible, the applicable bio-optical algorithms.

Without ground-truth data—more properly sea-truth data—it is impossible to maintain the calibration of a satellite sensor at the desired level over the full course of the mission, which is generally designed to be on the order of about five years (although many satellites operate for longer periods of time as evidenced by SeaWiFS, which was launched in 1997). This is not caused by any weakness in the sensor nor in the onboard calibration devices; it is simply because of unavoidable physical considerations: *the goal of modern ocean color sensors is to provide the water-leaving radiance in the blue with a 5% accuracy over oligotrophic, chlorophyll-depleted, waters* (Gordon 1997), which can be expressed as well as an uncertainty of 0.002 in terms of reflectance (Antoine and Morel 1999). Because this marine signal only represents about 10% (at most) of the TOA radiance (i.e., the radiance directly measured by the spaceborne sensor), achieving this goal requires the instruments involved are calibrated to better than 0.5%, or approximately 1%. This is extremely challenging considering the present technology, and probably will remain an elusive accomplishment.

A successful strategy for ensuring high-quality observations from an ocean color satellite mission is based on a rather pragmatic approach and consists of a) making the best possible effort when initially characterizing and calibrating the spaceborne instrument on the ground, b) using onboard calibration devices or maneuvers to track sensitivity changes over time while on orbit, and c) adjusting individual channels to force agreement with the sea-truth data—the basis of the vicarious calibration procedure—which produces a final adjustment for the whole (instrument plus algorithms) system.

1.3 Moorings as Long-Term Data Sources

Maintaining a permanent optical mooring is a costly, but pertinent, solution to the problem of how best to col-

lect a significant number of the needed sea-truth observations for the vicarious calibration process. This is easily demonstrated by comparing this option to the usual oceanographic practice of deploying research vessels to various parts of the world ocean.

Past experience has demonstrated that a one-month cruise is able to produce a maximum of a dozen of match-up points when conditions are extremely favorable. This is simply because of the number of conditions that must be simultaneously fulfilled for a measurement to be usable for the calibration and validation process (clear sky, low wind speed, acquisition within a maximum of 1 h of satellite over pass, nominal operation of the instruments, etc.).

A permanent mooring is well adapted to maintaining a consistent time series of *in situ* measurements over a long period of time, because the needed personnel, equipment, and methodologies remain mostly fixed once they are established. Although the latter is a demonstrable advantage, ensuring the same level of consistency between the people, equipment, and protocols from different cruises inevitably adds some extra uncertainties in the overall enterprise of data collection and processing. A permanent station is also well suited for developing and testing new instrumentation as well as new algorithms, and therefore, to permanently improve the quality and the variety of products that can be derived from the ocean color observations at the TOA level. It is also a unique opportunity to establish the cross calibration between different sensors by anchoring them to the same *in situ* time series.

A criticism that is often made of the mooring option is the uniqueness of the measurement site. This is actually not an argument, because the vicarious calibration process is a physical process, which does not require that data from a variety of different environments are collected. It requests, however, that the maximum of information (quantitatively as well as qualitatively) are collected at the selected site so that the reconstruction of the TOA signal through radiative transfer calculations is performed with the best possible accuracy. This does not preclude, however, that data are collected in other environments for validation of level-2 products and for verification of the calibration obtained at the initial mooring site.

The scheme briefly exposed above (i.e., a permanent calibration site and a parallel program of validation from ships) was adopted by the SeaWiFS Project. It has been a success, and this sensor is probably the best-calibrated ocean color sensor the community has ever had, at least until next-generation sensors such as MERIS and MODIS are operational over a similar time span and demonstrate their full potential.

1.4 Specific Protocol Requirements

It has just been said that moorings are adapted to provide large numbers of *in situ* data points, however, *what would be the advantage in case these data are not of the desired quality*? The question arises, because the measurement conditions on a mooring may degrade the final quality of the data. Buoys are often moving a lot, because the sea is rarely totally flat, so the instruments are (at some level) in an unstable situation. They are often made of a large floating body with the equipment installed underneath, so the light sensors can be significantly shaded. The prolonged immersion of the instruments is favorable to the development of biofouling. Finally, the number of calibrations that can be performed, which is particularly important to track the temporal stability of the radiometers, is dependent on the frequency of maintenance visits (during which instruments can be exchanged). The servicing interval might be insufficient in some cases, either because it is inherent to the project organization or because of severe weather. Consequently, the qualification of a given mooring program with respect to the ocean color calibration and validation requirements should consider the above points and evaluate whether or not they have been accounted for through a protocol. The data collected by the moored instruments should be, for instance, compared to the same data derived from ship-deployed instrumentation.

2. STRATEGY

The BOUSSOLE Project is composed of three basic and complementary elements: a) a monthly cruise program, b) a permanent optics mooring, and c) a coastal Aerosol Robotic Network (AERONET) station. Each of these three segments is designed to provide specific measurements of various parameters at different and complementary spatial and temporal scales. When combined, they provide a comprehensive time series of near-surface (0–200 m) oceanic and atmospheric inherent optical properties (IOPs) and apparent optical properties (AOPs), required to accomplish several objectives:

- Performing the vicarious radiometric calibration of satellite ocean color sensors (i.e., the simulation of the TOA radiances recorded by the sensor in various spectral bands, including the visible and near infrared (NIR) domains);
- Performing the validation of the level-2 geophysical products that are produced from the observations of these satellite ocean color sensors, including the normalized water-leaving radiances, the pigment concentrations, and the aerosol optical thickness (AOT) and types;
- Performing both of these operations on a long-term basis (i.e., at least for the duration of the MERIS mission, for which the BOUSSOLE project has been primarily set up); and
- Making progress in several domains of ocean optics and bio-optics, as already stated earlier (Sect. 1).

A basic description of the three elements and the operations carried out there is given below.

2.1 Monthly Maintenance Cruises

From July 2001 to December 2003, the BOUSSOLE optics cruises were planned with a duration of three consecutive days distributed on a near-monthly basis within the budget of 30–31 sea days per year aboard the research vessel (R/V) *Tethys II*. In these first two and a half years, some cruises were unsuccessful in data collection because of bad weather preventing ship departure or scientific work for the entire three days. For this reason, for 2004 the cruise duration during the seasons with characteristically unsettled conditions, October to April, were increased to up to five days with a subsequent reduction in the overall number of cruises per year. The same logic is followed since 2005, yet without reduction of the number of cruises (i.e., 12 cruises per year).

The so-called *optics day* (defined as the period during which the Sun is at an angle greater than 20° above the horizon) commences and ends with a 400 m conductivity, temperature, and depth (CTD) profile. The CTD sensors are mounted on a rosette equipped with 11 Niskin bottles. Spectral absorption and attenuation, $a(z, \lambda)$ and $c(z, \lambda)$, respectively (z indicates depth and λ denotes wavelength), is measured at nine wavelengths using a Western Environmental Technology Laboratories (WETLabs), Inc. (Philomath, Oregon) 25 cm pathlength AC-9 with enhanced data handling (AC-9+) mounted in the twelfth bottle position. Additional sensors are the CTD and O_2 sensors, a colored dissolved organic matter (CDOM) fluorometer, a chlorophyll fluorometer, and a backscattering (b_b) sensor (Sect. 6.2).

For at least one CTD cast each day, the bottles are fired at selected depths during the ascent of the CTD over the 0–400 m depth range. The collection depths are decided during the descent of the CTD after observation of the fluorescence profile, thus optimizing the representation of any features in the water column. For other casts, triplicate samples are collected from 5 and 10 m. In the summer, when the optics day is longer or when there are ideal satellite match-up conditions, an additional CTD profile is performed around solar noon or in time with a SeaWiFS or MODIS overpass.

Seawater samples (2.8 L) are filtered through Whatman GF/F filters using a low pressure vacuum and stored in liquid nitrogen. Back in the laboratory, the filters are later analyzed by high performance liquid chromatography (HPLC) and spectrophotometry for pigments and particulate absorption, respectively (Sect. 7.1 and 7.2).

Multispectral upward and downward irradiance profiles, $E_u(z, \lambda)$ and $E_d(z, \lambda)$, respectively, are performed with the objectives of providing synchronous *in situ* SeaWiFS and MERIS calibration and validation profiles, characterizing the light field throughout the day at the BOUSSOLE site, and providing a support data set for observations from the BOUSSOLE buoy. During these profiling sessions, multiple profiles are performed with a SeaWiFS Profiling Multichannel Radiometer (SPMR), if possible, to improve the quality of the data by replicates. The first SPMR session of the day begins after the first CTD profile, and continues ideally until the end of the optics day, before the final CTD profile. A gimbaled 4π photosynthetically available radiation (PAR) sensor positioned on the foredeck and operated from the CTD computer serves as a light field stability indicator during SPMR profiling.

For the satellite passes, whenever possible, SPMR profiling is performed within 1 h of satellite overhead passes of SeaWiFS and MERIS and around solar noon. Optimal conditions for these measurements are low humidity, blue skies and flat, calm sea surface. If the sky is clear and sea conditions are calm, a second-generation Satellite Validation for Marine Biology and Aerosol Determination (SIMBADA) measurements are performed consecutively where possible with SPMR profiles (only carried out from July 2001 to July 2003). If sea conditions are poor but the sun is clear of clouds, SIMBADA sun photometer measurements can be made at intervals throughout the day to measure atmospheric optical thickness.

When sea surface conditions are calm, a low-volume (small shadow) surface float is used to suspend the SPMR in a vertical position with the E_u sensor submerged approximately 20 cm below the surface. The SPMR is held in this orientation for a duration of at least 3 min and is released when the light field is expected to be stable. This decision is a judgement call based on sky observation and monitoring of the PAR sensor. To start the descent, an electronic trigger mechanism is fitted to the surface float, which can be controlled from inside the lab. Multiple descents ideally will be started in this way and the data will be used to assess near-surface upwelled radiance (L_u) extrapolation model calculations.

For each cruise, at the end of the on-site optics measurements, there is a CTD and IOP transect between the BOUSSOLE site and the port of Nice (France) consisting of six fixed locations. The aim is to have a representative profile of the water column on either side of the boundary to the Ligurian Current. The approximate time of day that this transect is performed is kept similar for each cruise, whenever possible, to minimize the influence of diurnal variability.

A study of the spatial variability at the BOUSSOLE site was performed once on each cruise until the middle of 2005. A fixed square mile quadrilateral grid based on Global Positioning System (GPS) data is covered by the ship at a speed of 7–8 kts. During transit around this grid, water is continuously being pumped from an inlet beneath the ship's hull, and directed to the thermosalinograph and a fluorometer. Samples are collected at three equidistant points along this grid, for subsequent HPLC analyses, in order to convert dimensionless fluorescence measurements into chlorophyll concentrations.

On other uninterrupted transits between Nice and the BOUSSOLE site, particularly when there is a high sun angle and clear skies, CIMEL Electronique (Paris, France)

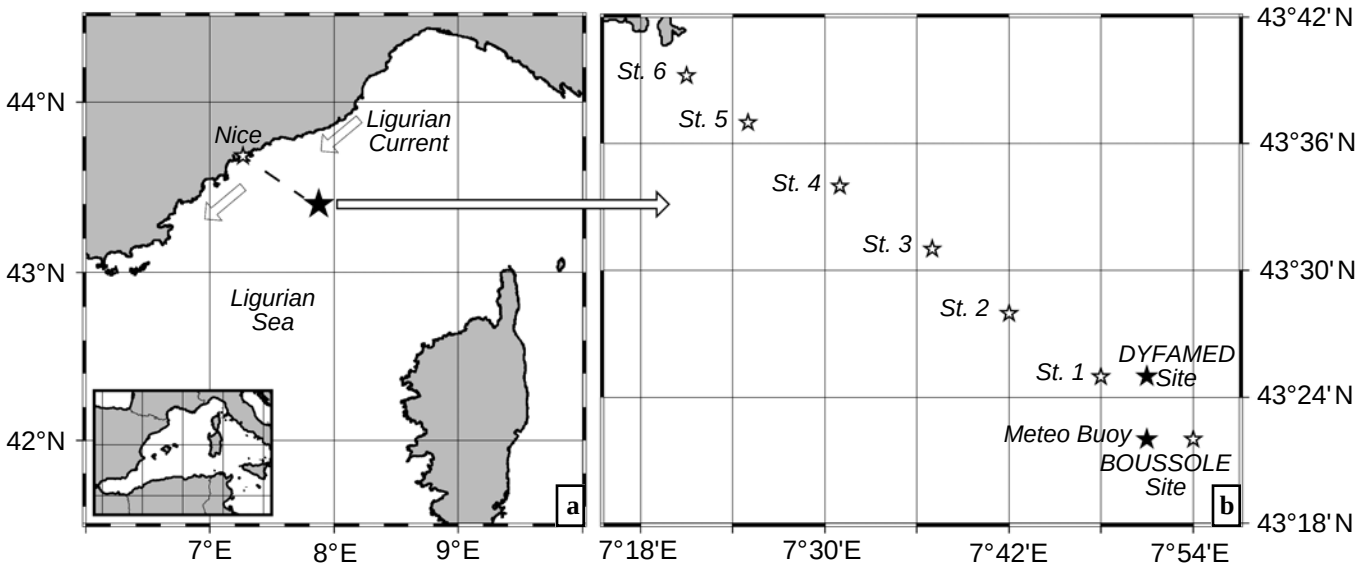

Fig. 1. The coastal area of the northwestern part of the Mediterranean Sea showing **a)** the southern coast of France and the island of Corsica, plus the generalized work area in the Ligurian Sea (black star) for the BOUSSOLE activity; and **b)** a magnification showing the position of the BOUSSOLE mooring plus the *Dynamique des Flux Atmosphériques en Méditerranée* (DYFAMED) site and the Meteo buoy maintained by the French weather forecasting agency (Meteo France). The positions of the six stations, which are sampled once a month during transits from Nice to the BOUSSOLE site, are also displayed.

model 317 (CE-317) sun photometer measurements are taken at 30 min intervals (approximately 5 nmi) to characterize the variability in atmospheric optical thickness between the *Cap Ferrat* sun photometer site and the BOUSSOLE site.

2.2 The Mooring Site

The mooring site is equipped with a new type of buoy, specifically designed for collecting optical data (Sect. 5) with two specific objectives: a) obtain a near-continuous sampling at the surface (depths less than 10 m), in order to efficiently support the validation of the geophysical parameters derived from ocean color remote-sensing observations collected by a variety of satellite sensors; and b) create a high-resolution data set to support fundamental work in marine optics, e.g., bidirectionality of the radiance field emerging from the ocean, short-term changes of optical properties, response of optical properties after strong environmental forcings (red rains and storms), effect of wind-induced bubbles, near-surface behavior of radiometric quantities, etc.

The satellite sensors that have been or are being supported include MERIS from the European Space Agency (ESA), SeaWiFS and MODIS-A (on the Aqua spacecraft) from the National Aeronautics and Space Administration (NASA), plus the third Polarization and Directionality of the Earth Reflectance (POLDER-3) sensor aboard the *Polarisation et Anisotropie des Réflectances au sommet de l'Atmosphère, couplées avec un Satellite d'Observation emportant un Lidar* (PARASOL) satellite, from the French *Centre National d'Etudes Spatiales* (CNES).

2.3 The Coastal Site

Since 3 July 2002, a coastal site has been equipped with an automatic sun photometer station, introduced within the AERONET†. This site is the *Cap Ferrat*, in front of the *Laboratoire d'Océanographie de Villefranche* (LOV), by 7°19′E,43°41′N. This equipment provides a continuous record of the sky radiances (principal plane and almucantar) and of the attenuation of the direct solar beam, from which aerosol types and aerosol optical thickness will be retrieved. The annual calibration is managed by the AERONET group, as well as the inversion of the sun photometer measurements in order to get the aerosol optical thickness. This site is established in order to provide the last element of data that is needed in the process of vicariously calibrating ocean color satellite observations, namely the aerosol types and optical thickness.

3. MEASUREMENT SITES

The following three subsections describe the main characteristics of a) the offshore BOUSSOLE site (32 nautical miles from Nice), b) the sampling done on the transect from the BOUSSOLE site to the Nice harbor, and c) the AERONET station that is installed within the military premises of *Cap Ferrat*.

† Further details about AERONET sites are available at the following Web address: `http://aeronet.gsfc.nasa.gov`.

3.1 The BOUSSOLE Site

The site where the mooring is deployed and where the monthly cruises are carried out is located in the Ligurian Sea, one of the sub-basins of the Western Mediterranean Sea (Fig. 1). Water depth varies between 2,350–2,500 m in this area, and it is 2,440 m at the mooring point, which is located at approximately 7°54′E,43°22′N.

3.1.1 Bottom Depth

Accurate bathymetry data was a critical requirement for properly deploying the taut mooring used to anchor the buoy to the ocean floor (Sect. 5). The water depth at the proposed site was determined by performing several deep CTD casts, from which the measurement of the pressure (translated into depth using the simultaneous observations of temperature and salinity), was added to the measurement of an altimeter mounted on the CTD rosette (the CTD was stopped about 10 m before the bottom was reached). The water-column thickness was, therefore, determined with a less than 1 m accuracy. These measurements were used to calibrate a two-dimensional mapping of the sea bottom that was obtained from the ship echo sounder. This mapping revealed a flat bottom characterized by a weak northwest-to-southeast slope (Fig. 2).

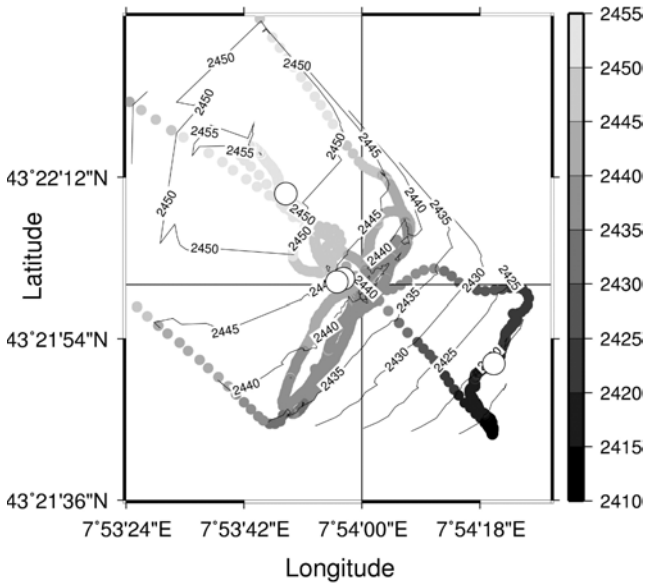

Fig. 2. The bathymetry, in meters, of the area around the BOUSSOLE site (at the crossing of the horizontal and vertical lines). The open circles indicate the location of the individual deep CTD casts that allowed the echo-sounder survey (grey dots) to be calibrated in terms of water depth (gray-scale bar to the right of the plot).

The tidal amplitude, the dynamic height changes, and the water level variations caused by atmospheric pressure changes are all less than about 50 cm for the deployment site, which is not significant for the type of mooring design envisioned here. They might become problematic in those cases wherein a similar mooring is deployed in another water mass where such changes are larger.

3.1.2 Physical Conditions

The BOUSSOLE site was selected in particular because the prevailing ocean currents are usually extremely weak. This peculiarity is due to the selected position being rather close to the center of the cyclonic circulation that characterizes the Ligurian Sea. The northern branch of this circulation is the Ligurian Current, which manifests as a jet flowing close to the shore in the northeast-to-southwest direction which, in turn, establishes a front whose position varies seasonally (closer to shore in the winter than in the summer). The southern branch of the circulation is a southwest-to-northeast current flowing north of the island of Corsica; the eastern part of the circulation is simply imposed by the geometry of the basin.

The dominant winds are from the west to southwest and from the northeast sectors (Fig. 3), and are channeled into these two main directions by the general atmospheric circulation of the region and by the topography formed by the Alps and the island of Corsica. Over the period from February 1999 to July 2003, only five days were recorded with a wind speed above 40 kts, and 34 and 100 days with wind speeds between 35–40 kts and 30–35 kts, respectively. These high wind speeds, and the associated large swells are concentrated in the late fall to early spring time periods of November to March, respectively.

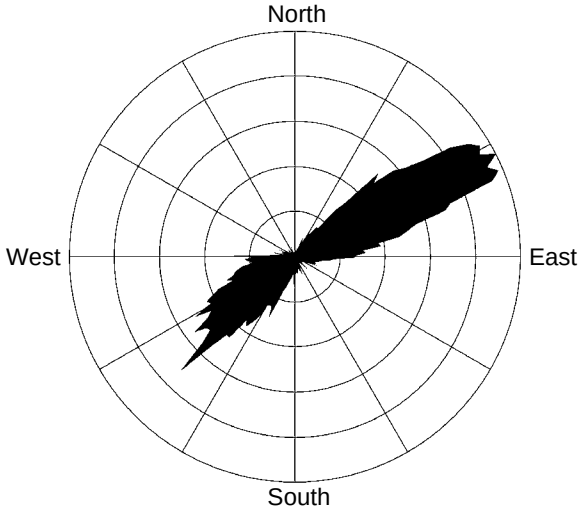

Fig. 3. A so-called *wind rose* for the BOUSSOLE site showing the dominant wind directions (the data are from the Meteo buoy).

The range of environmental parameters is also illustrated in Fig. 4, where physical conditions are displayed as a four-year record of the wind speed, significant wave height, and sea surface temperature (SST). These data are

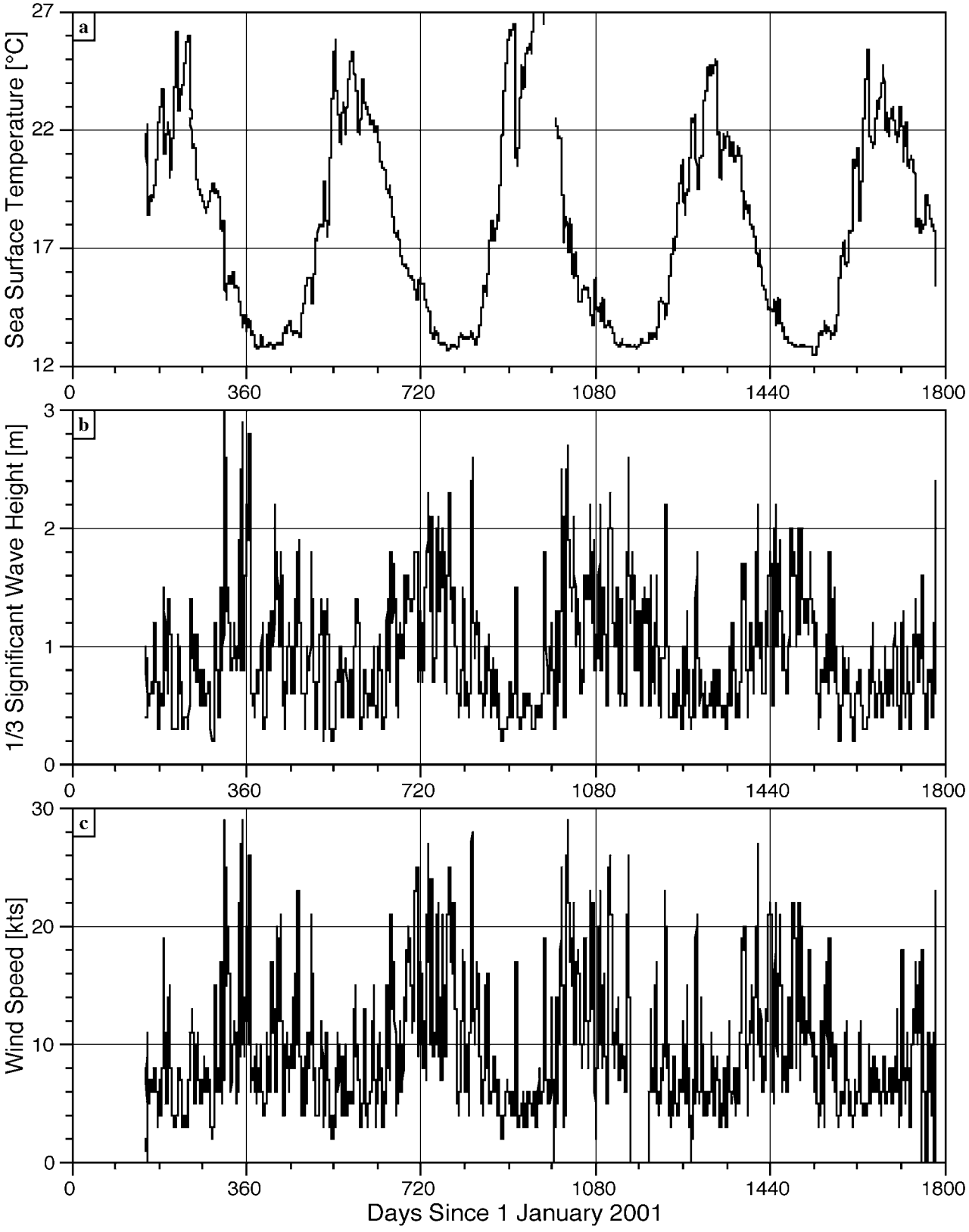

Fig. 4. An approximately five-year time series of conditions at the BOUSSOLE site showing **a)** the sea surface temperature, **b)** the swell height (the one-third most significant waves), and **c)** the wind speed.

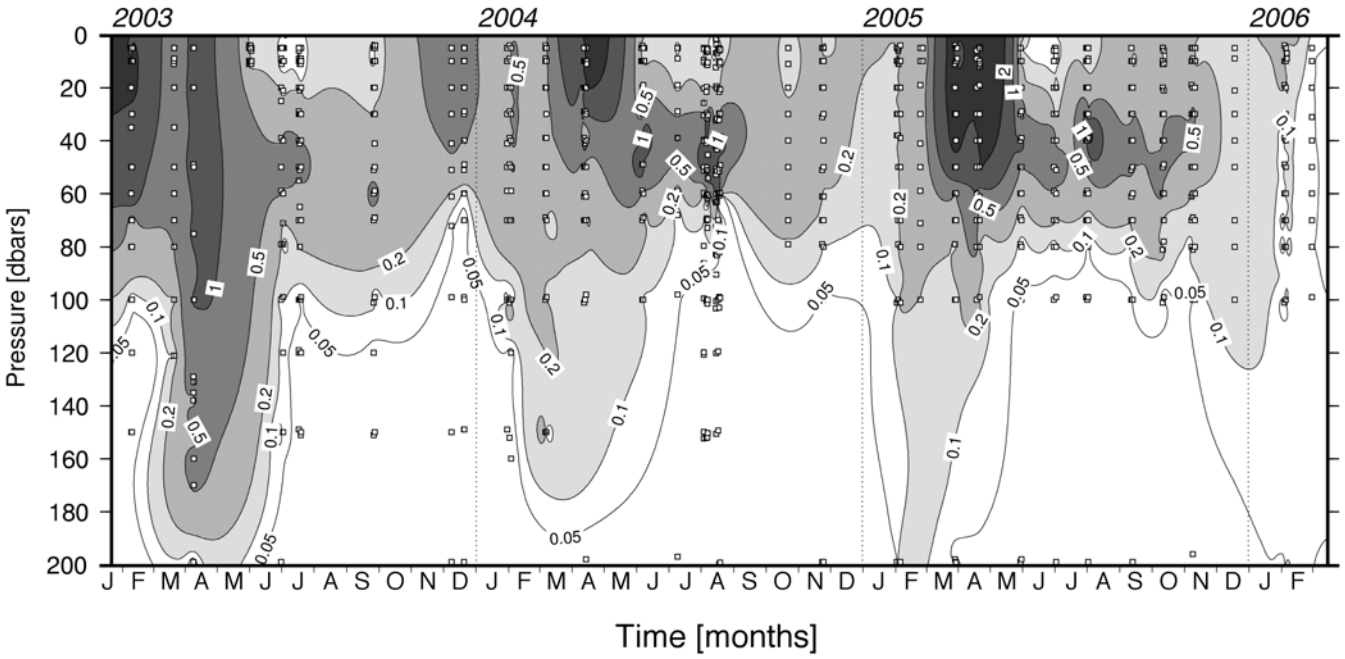

Fig. 5. A time series of the total chlorophyll *a* (TChl *a*) concentration at the BOUSSOLE site. Low to high concentrations are represented by light to dark colorations in the gray-scale palette, respectively. The calendar years for the time series are given along the top of the plot.

obtained from a weather mooring, which is aplproximately two nautical miles away from the BOUSSOLE site. The weather mooring is instrumented and maintained by Meteo France, the French weather forecasting agency.

The minimum SST is about 12.7°C (associated with a salinity of 38.4 psu), which is a constant value reached in winter when the water mass is fully mixed down to the bottom. This deep mixing contributes to the formation of the bottom waters of the western Mediterranean Sea. These data are not further discussed, as they are provided just for illustration of the typical annual cycle of the physical conditions at the BOUSSOLE site.

3.1.3 Trophic Conditions

Oligotrophic conditions prevail at the BOUSSOLE site during the summer with chlorophyll *a* concentrations below 0.1 mg m^{-3}, with minima around 0.05 mg m^{-3}. Higher concentrations, up to about 5 mg m^{-3}, occur during the early spring bloom (February to March or April). Intermittent enhancements occur in winter when sunny weather occasionally, and temporarily, stabilizes the nutrient-rich waters. Moderate concentrations, between 0.1–0.2 mg m^{-3}, characterize most of the other periods of the year. This is illustrated in Fig. 5 and later on in this report (Sect. 8).

3.1.4 Other Activities in the Area

The BOUSSOLE site (Fig. 1) is located in an area that has been defined some years ago as an area dedicated to scientific work, and where is located another site where monthly cruises are taking place in the frame of the DYFAMED observation service started in 1991 (Marty 2002†). This service collects core data that are made publicly available to the entire scientific community and includes CTD casts, HPLC pigments, nutrients, oxygen, dissolved organic carbon (DOC), and short-time ^{14}C incubation primary production. Other less permanent activities are carried out occasionally around this site [see the Deep-Sea Research special issue 49(11), 2002, Studies at the DYFAMED French Joint Global Ocean Flux Study (JGOFS) time-series station, N.W. Mediterranean Sea].

3.2 Coastal Transects

The transect from the coast (actually from the Nice harbor) to the BOUSSOLE site is characterized by a permanent front between the waters of the Ligurian Current and the more offshore waters. This front moves from near the coast (about 10 nmi) in spring and summer to near the BOUSSOLE site in winter.

In addition to classic hydrography (CTD casts), which have already been performed in the past along the Nice-to-BOUSSOLE transect (not systematically, however), the BOUSSOLE activity is documenting the IOPs (total absorption and attenuation, backscattering at three wavelengths, and CDOM fluorescence) at six fixed stations.

† Additional information is available at the following Web site: `http://www.obs-vlfr.fr/sodyf/home.htm`.

Table 1. A summary of the types of data collected in support of the BOUSSOLE activity at the coastal, buoy, and ship sites (the latter is in very close proximity to the buoy). The above- and in-water references indicate how the oceanic data are collected (for example, above- or in-water radiometers). The monthly service visits to the buoy, although systematically scheduled, only occur if weather, site conditions (e.g., wave height), and instrument functionality permit. The data acquisition rates for the coastal and buoy continuous sampling are as follows, respectively: a) variable, down to 10 min; and b) 15 min (1 min at 6 Hz every 15 min from sunrise to sunset) plus 1 min at 6 Hz each hour during nightime.

Sampling (and Site)	*Data Type*	*Instrument† or Model*	*Physical Measurements*	λ [nm]	*Data Products*
Continuous (Coastal)	Atmospheric	CE-318	Sky radiances, and attenuation of the direct solar beam	λ_6	Aerosol optical thickness (τ_a) and types
Continuous (Buoy)	Above-Water	OCI-200	Downward irradiance	λ_7	E_s
	In-Water	OCI-200	Downward irradiance at 4 and 9 m	λ_7	E_d
	In-Water	OCI-200	Upward irradiance at 4 and 9 m	λ_7	E_u
	In-Water	OCR-200	Upwelling radiance at 4 and 9 m	λ_7	L_u and L_W
	In-Water	MINITracka	Fluorescence at 4 and 9 m		F, $[\mathrm{TChl}\,a]$ proxy
	In-Water	C-Star	Beam attenuation at 9 m	660	c
	In-Water	SBE 37 SI	Hydrography at 9 m		T, S, and P
	In-Water	Hydroscat-II	Backscattering at 9 m	λ_2	b_b
	In-Water	EZ-III	Tilt and heading at 9 m		Tilt and heading‡
Monthly (Ship)	Above-Water	SIMBADA	Total water radiance and attenuation of the direct solar beam	λ_{11}	L_W and τ_a
	Above-Water	OCI-1000	Downward irradiance	λ_{13}	E_s
	In-Water	OCI-1000	Downward irradiance 0–150 m	λ_{13}	E_d
	In-Water	OCI-1000	Upward irradiance 0–150 m	λ_{13}	E_u and L_W
	In-Water	SBE 911+	Hydrography 0–400 m		T, S, P, F, and $[O_2]$
	In-Water	Rosette§	Discrete seawater samples 0–400 m		C_i, a_p, and a_ϕ
	In-Water	AC-9+	Absorption, attenuation 0–400 m	λ_9	a, c, and $b = c - a$
	In-Water	ECO-BB3	Backscattering coefficient 0–400 m	λ_3	b_b
	In-Water	C-STAR	Attenuation coefficient 0–400 m	λ_1	c
	In-Water	WCF¶	CDOM fluorescence 0–400 m		CDOM description

Notes:

† Instrument names, as well as the corresponding manufacturers, are cited here, and in other sections of this report, because they have been identified as appropriate for the particular application. This identification is not a recommendation for the use of any of these instruments; nor does it imply that these instruments are the best suited for the application or for other similar projects. In addition, the possibility of using any other instrumentation than those cited here is retained without notice.

‡ The buoy heading is used to determine the orientation of the in-water sensors, which are mounted on fixed arms, with respect to the Sun.

§ SBE 12-bottle rosette for laboratory analyses of phytoplankton pigment concentrations (C_i) from HPLC; plus particles and phytoplankton absorption coefficients (a_p and a_ϕ, respectively).

¶ WETLabs CDOM Fluorometer.

λ_1 660 nm.

λ_2 442 and 560 nm.

λ_3 470, 530, and 660 nm.

λ_6 440, 675, 870 (plus 870 polarized), 940, and 1,020 nm.

λ_7 412, 443, 490, 510, 560, 665, and 683 nm (a spare set of sensors have 443, 490, 510, 555, 560, 665, and 683 nm).

λ_9 412, 443, 488, 510, 532, 555, 630, 676, and 715 nm.

λ_{11} 350, 380, 412, 443, 490, 510, 565, 620, 670, 750, and 870 nm.

λ_{13} 412, 443, 455, 490, 510, 530, 560, 620, 665, 683, 705, 780, and 865 nm before July 2003, and 380, 412, 443, 455, 490, 510, 530, 560, 620, 665, 683, 705, and 780 nm thereafter.

The stations are approximately 5 nmi away from one another, and the survey work started in May of 2003. Documenting these properties at this series of stations is also a way to put the observations made at the BOUSSOLE site into a broader context.

3.3 The Coastal AERONET Site

Aerosol amounts and types are information of prime importance in the process of vicariously calibrating ocean color sensors (Sect. 10), but they cannot be obtained easily at the mooring site. This is the main reason for having installed an automatic scanning sun and sky photometer at *Cap Ferrat*, which is providing a continuous record (cloud permitting) of these parameters thanks to the logistics and data transmission capabilities of the AERONET.

The parallel analysis of the sun photometer and satellite observations are expected to indicate the circumstances wherein the data collected at the coast are representative of the conditions offshore. In support of this study, aerosol—and when the sky is clear—optical thickness measurements are also performed en route when steaming from Nice to the BOUSSOLE site, in order to get some idea of the spatial heterogeneity of aerosol properties.

4. DATA COLLECTION

The three subsections below briefly summarize the set of measurements that are performed offshore, either from the ship or from the buoy, and at the coastal site. They are summarized in Table 1. Details on the data acquisition protocols will be provided in Sect. 6 and data processing in Sect. 7.

4.1 Ship Measurements

The set of parameters directly derived from the measurements made by the above-water SeaWiFS Multichannel Surface Reference (SMSR) and the in-water SPMR to 200 m depth are as follows (λ_{13} denotes the 13-channel spectral band set): a) surface irradiance, $E_s(\lambda_{13})$, and b) upward and downward irradiance, $E_u(\lambda_{13})$ and $E_d(\lambda_{13})$, respectively. The wavelengths for these measurements are 380, 411, 443, 456, 491, 510, 532, 560, 620, 665, 683, 705, 779, and 865 nm

Profiles with the CTD rosette to a depth of 400 m are used to collect the following parameters: chlorophyll fluorescence, CDOM fluorescence, attenuation and absorption coefficients (412, 440, 488, 510, 532, 555, 630, 676, and 715 nm), b_b (440, 532, and 650), temperature, conductivity and derived salinity, oxygen concentration, and surface PAR. Seawater samples are collected and filtered for subsequent determination of the phytoplankton pigments and particulate absorption.

The SIMBADA above-water radiometer collects water-leaving radiance and aerosol optical thickness at 350, 380, 412, 443, 490, 510, 565, 620, 670, 750, and 870 nm.

4.2 Buoy Measurements

The set of parameters directly derived from the buoy above- and in-water measurements are as follows (λ_7 denotes the 7-channel spectral band set for the AOP sensors): a) $E_s(\lambda_7)$; b) $E_d(\lambda_7)$, $E_u(\lambda_7)$, $L_u(\lambda_7)$, $c(660)$, and chlorophyll fluorescence at 4 m; and c) $E_d(\lambda_7)$, $E_u(\lambda_7)$, $L_u(\lambda_7)$, chlorophyll fluorescence, $c(660)$, $b_b(443)$, and $b_b(560)$, conductivity, temperature, pressure, and two-axis tilt as well as compass heading at 9 m. The wavelengths for the AOP measurements are 412, 443, 490, 510, 560, 665, and 683 nm (a spare set of sensors has the 412 nm channel replaced with 555 nm).

From these measurements, various AOPs or IOPs are derived: the diffuse attenuation coefficients for upward and downward irradiance, K_u and K_d; the attenuation coefficient for upwelling radiance, K_L; the diffuse reflectance just below the sea surface, R; the nadir Q-factor, E_u/L_u; and the attenuation and backscattering coefficients, c and b_b. The absorption coefficient, a, is tentatively derived through inversion of the AOPs (using, for example, K_d and R). Here it is assumed that K_d and R can be accurately derived from the two measurement depths of the buoy, e.g., Gordon and Boynton (1997), Leathers and McCormick (1997), and Barnard et al. (1999). Table 2 shows how the data acquired on the system fits to the band sets of several ocean color sensors.

Table 2. The MERIS wavelengths, as acquired on the buoy (leftmost column), and the spectral shift of other satellite bands with respect to those of MERIS. The second row gives the channel bandwidths.

MERIS 10 nm	*POLDER-3* 20 nm	*SeaWiFS* 20 nm	*MODIS* 10 nm
412 nm		0	0
443	0	0	0
490	0	0	−2
510		0	
560	+5	−5	−9
665	+5	+5	+2
683			0

The data are derived from the IOCCG (1998) report.

4.3 Coastal Measurements

The parameters collected at the coastal site are the sun and sky radiances, using standard filters at 440, 675, 870, 940, and 1,020 nm plus a polarized filter for 870 nm, which are used to derive total column water vapor, ozone, and aerosol properties, including Angström coefficients, optical thickness, and polarization ratios†.

† These derived parameters are available at two Worldwide Web addresses: `http://www-loa.univ-lille1.fr/photons/DATA/Villefranche` and `http://aeronet.gsfc.nasa.gov`.

5. THE BOUSSOLE BUOY

The description of the BOUSSOLE buoy is presented more or less in a chronological order, starting with the design, and then continuing with the successive versions and the various tests that were performed.

5.1 Design Concept

Platforms developed for oceanographic purposes are rarely adapted to the unique problems of deploying radiometers. Accurately measuring the in-water light field is difficult, because the instruments themselves and, usually more significantly, the platform onto which they are installed, introduce perturbations (shading in particular). Other difficulties originate from the need to keep the instruments oriented as stably as possible, either because a nadir radiance or a planar irradiance is being measured. The actual measurement depth can also be difficult to accurately assess, because rapid vertical displacements of the instruments sometimes occur, which prevent any precise estimation of pressure (and, thus, depth). Considering the above difficulties (among others), a new type of platform was developed and specifically dedicated to making high-quality radiometric measurements at sea. The platform minimizes shading effects by reducing the cross-sectional area of structural components, and its wave-interaction characteristics ensure the stability of the instruments.

The design constraints for the new platform were:

1. Measure E_u, E_d, and L_u (nadir) at two depths, plus E_s at the surface;
2. Minimize the shading of the instruments;
3. Maximize the stability of the instruments; and
4. Permit deployment at a site with a water depth of 2,440 m, and swells up to 8 m (but small horizontal currents).

The basic design principle for the buoy is that of a *reversed pendulum*, with Archimedes thrust replacing gravity. A large sphere (with a diameter of about 1.8 m) is stabilized at a depth out of the effect of most surface waves, and connected at the end of a long cable anchored on the sea bottom. This sphere creates the main buoyancy of the system. A rigid, tubular, structure is fixed above the sphere, which hosts the instrumentation on horizontal arms (at 4 and 9 m depths). The resulting approximately three tons of thrust ensures the stability of the system, which is subjected to very limited forces from the so-called *transparent-to-swell* superstructure.

The taut-cable mooring is significantly different from what is usually referred to as *spar buoys*. With the BOUSSOLE design, there is no large body at the surface generating shade, and the stability of the instruments is ensured even for quite large swells. The small vertical excursions of the near-surface structure means the water level above the instruments is accurately known at all times. A schematic depiction of the buoy design is presented in Fig. 6.

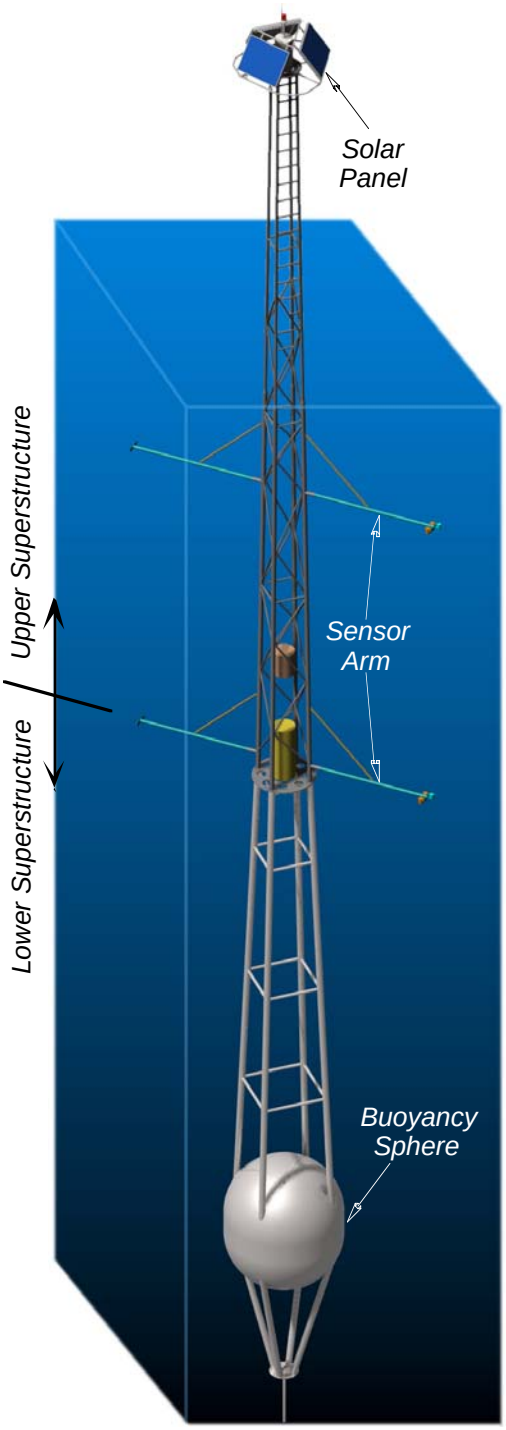

Fig. 6. A schematic of the principle BOUSSOLE components distinguished according to the upper and lower superstructure portions (total height is 25 m). The in-water radiometers are mounted at the end of the sensor arms which are located well above the buoyancy sphere (the largest perturbation to the light field; the underwater structure is entirely black, however). The above-water solar reference is sited above the solar panels, which are located 4 m above the nominal seawater surface.

Fig. 7. The complete mooring line on the deck of the *Castor–02*, before deployment. The beginning of operations started 20 July 2000, 0700 Greenwich Mean Time (GMT).

Theoretical calculations were made on the response of the proposed design to the prevailing environmental conditions, by specifying an initial and preliminary design and material for the construction, as well as a swell height of 5 m and a 7 s wave period (typical of the deployment site). The natural response frequencies of the whole mooring were determined along with the period and amplitude of the oscillations and displacements due to swell and currents. These calculations were extremely encouraging in terms of the expected tilt and oscillation parameters, so the decision was made to first build a reduced-scale model in order to perform more realistic tests.

5.2 Reduced-Scale Model

A one-tenth scale model was developed in order to verify the theoretical predictions, and it was tested in a $24\times16\times3\,m^3$ engineering pool with a 10 m shaft, by applying to it several types of swells and currents, either monochromatic or random swells, up to 5 m real scale. Results of these tests completely confirmed the theoretical predictions that were previously carried out, in terms of horizontal and vertical displacements (the latter are extremely low), as well as in terms of angular deviations from the vertical. For instance, the mean tilt of the buoy is approximately 4° (with about ±4° of pitching), for a 4.6 m swell of period 5.2 s, i.e., at the limit before wave breaking occurs.

The reduced-scale model tests also confirmed no *hidden defects* were present—which are usually undiscernible with calculations alone—so there was no reason to believe there was an unknown element that might compromise the feasibility of the overall system. The tests also showed a significant sensitivity to currents, but the deployment site is typified by rather low current velocities. The tests were considered fully conclusive and led to the construction of the first full-scale version 1 of the buoy.

5.3 Full-Scale Version 1

The version 1 buoy was built during the spring of 2000. To minimize weight, aluminum was used as the principal construction material, and the buoy was manufactured in two large parts. The lower section, which extends from 20 m to 9 m below the surface, consists of the buoyancy sphere and a central tubular support structure; the upper section, which goes from 9 m below the sea surface to 4.5 m above the surface, hosts all of the above- and in-water scientific instrumentation either within the extension of the central tubular structure or at the ends of sensor arms.

The so-called *beta* (version 1) buoy was deployed during three months (20 July to 20 October 2000), which exposed the system to a variety of meteorological situations. The buoy was equipped with two inclinometers, a pressure sensor, an ARGOS beacon, and a flashing light. The goal of this deployment was to evaluate the design concepts of the buoy so as to identify possible problems requiring modifications. Figure 7 shows the full mooring on the deck of the ship before being deployed. A full day was necessary for the deployment operations, which were

significantly different than what is usually performed for classical moorings because it is a taut mooring. The details of these operations are not given here. The results of the initial deployment are shown in Figs. 8 and 9.

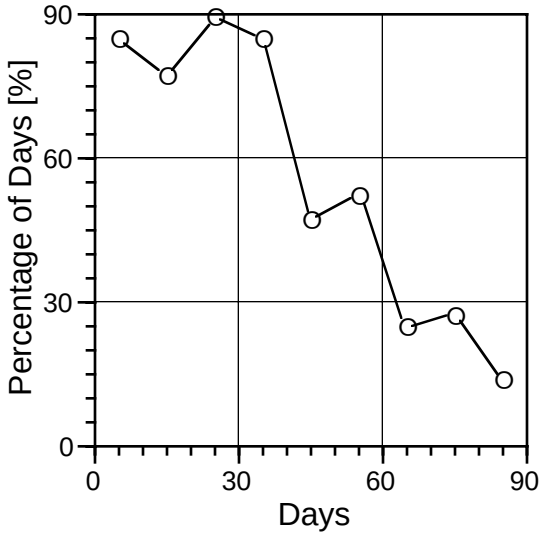

Fig. 8. The percentage of the tilt measurements that were less than 5°, as computed over successive 10-day periods of the qualification deployment.

Ignoring details beyond the scope of the initial deployment, the following points are relevant:

- From mid-September to the end of the deployment, the conditions were quite rough (mean swells up to 4 m with at least 5 m peaks).
- Until mid-September, the periods where the buoy is inclined at angles larger than 5° is small, which means that the beta version was already satisfying the requirements for meteorological conditions from calm to moderate.
- Oscillations were observed, which exactly match the inertial period of the ocean at the latitude of the site, and are most likely due to the frequency response of the water masses after the wind stress is relaxed.

In summary, the results of the qualification deployment showed some lack of righting torque, with discernible consequences on the behavior of the buoy when the swell becomes greater than about 2 m. Although not dramatic, this behavior is unsatisfactory, so slight modifications in the design and construction of the buoy were introduced in order to improve the percentage of time for which the requirements—in terms of inclination—are satisfied.

5.4 Version 2 Modifications

For the version 2 design of the buoy, the buoyancy sphere was placed at 17 instead of 18 m. Consequently, the distance from the center of the sphere to the termination point of the buoy and the mooring cable was 1 m greater (and the righting torque was, therefore, much larger). The materials used to build the upper part of the buoy (the one equipped with arms and the instrumentation) were also changed from aluminum to carbon composite. A specific study was conducted to verify the composite material was a satisfactory substitute, and this was definitely the case. This study was also used for dimensioning the material used during construction.

The impact of these changes on the upper part of the system were rigidity was improved, weight was reduced by approximately two-thirds, corrosion risks were decreased, the drag coefficient was reduced by the use of superstructure tubes with a smaller diameter, and the elastic limit was larger than it was in comparison to the forces imposed by breaking waves. In addition, a net gain of 60% in the righting torque was obtained for the full buoy.

5.5 May 2002 Deployment

The modified version of the buoy was deployed onsite with all its instrumentation on 16 May 2002. Some images of this deployment are shown in Fig. 10. Soon after this deployment, an atypical behavior of the buoy was identified, in particular, an abnormal lowering of the buoy—the exposed superstructure was too low in the water. When a clear analysis of what was happening was possible, and when the weather permitted safe at-sea operations, a ship was sent onsite.

Unfortunately the ship arrived too late, and the entire system was lost. The cause of the sinking was a leak in the main flotation sphere. The exact reason for the leak was not discovered, but most likely it was caused by a manufacturing defect.

5.6 Version 3 Modifications

After the May 2002 accident, two independent engineering studies were enacted, the objective of which was to improve the confidence in the design of the buoy and to provide advice for the construction of a replacement. These two studies were performed by the *Institut Français de Recherce pour l'Exploitation de la Mer* (IFREMER†) and the Marine Technology Research Institute‡ (MARINTEK). The results of these inquiries confirmed the feasibility of the transparent-to-swell concept, but recommended the use of either foam or steel for the construction of the

† Translated as the French Research Institute for Exploitation of the Sea and headquartered in Issy-les-Moulineaux, France. Additional details are available at the following Web address: `http://www.ifremer.fr`.

‡ Headquartered in Trondheim, Norway, MARINTEK develops and verifies technological solutions for the shipping and maritime equipment industries and for offshore petroleum production. Further information is available at the following Web address: `http://www.marintek.sintef.no`

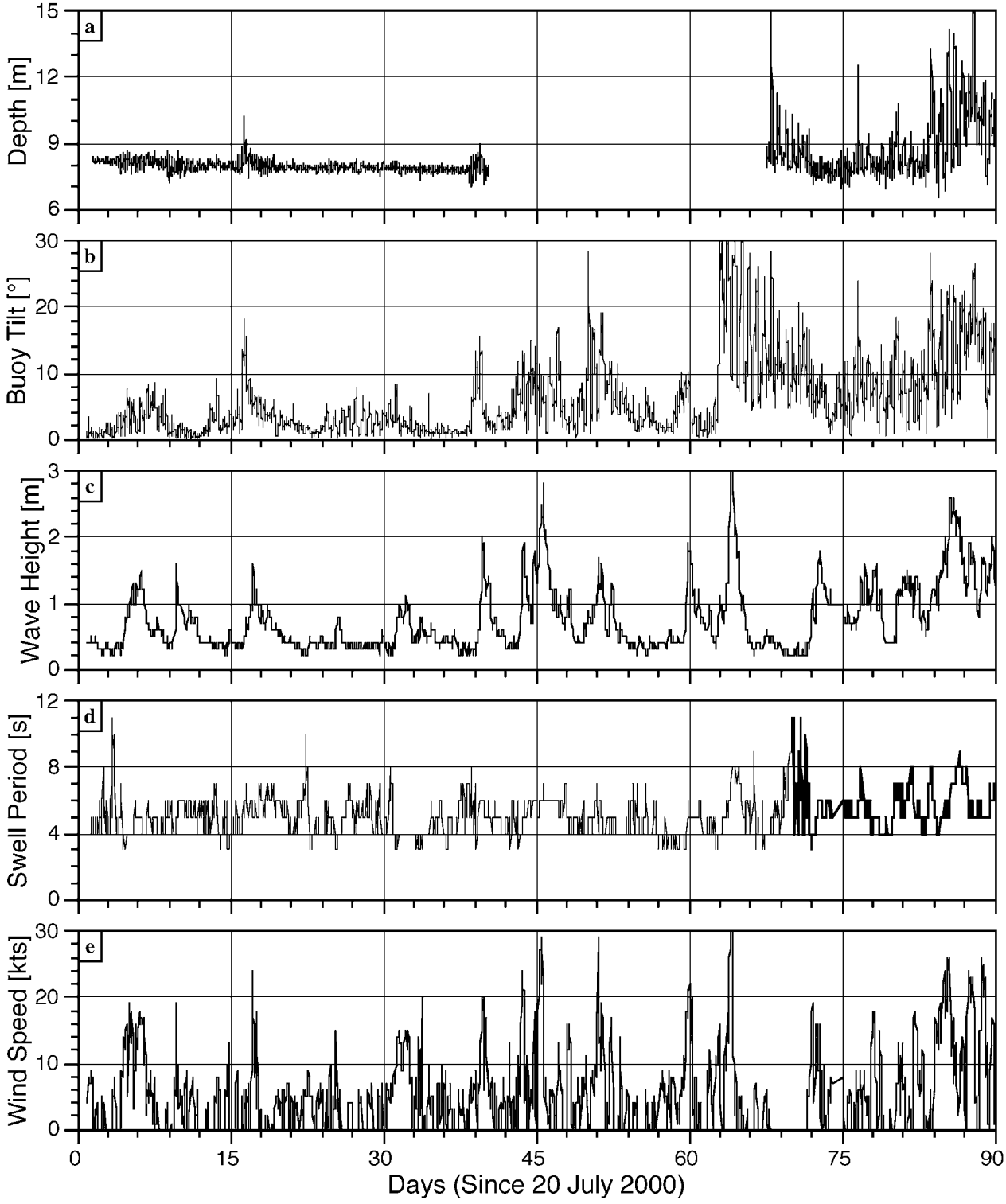

Fig. 9. The results of the qualification deployment (20 July to 20 October 2000), showing the time series of **a)** the depth of the buoy CTD (nominally at 8.3 m when the buoy is motionless and the sea surface perfectly flat), **b)** the buoy tilt, **c)** the swell height (the one-third most significant waves), **d)** the swell period, and **e)** the wind speed.

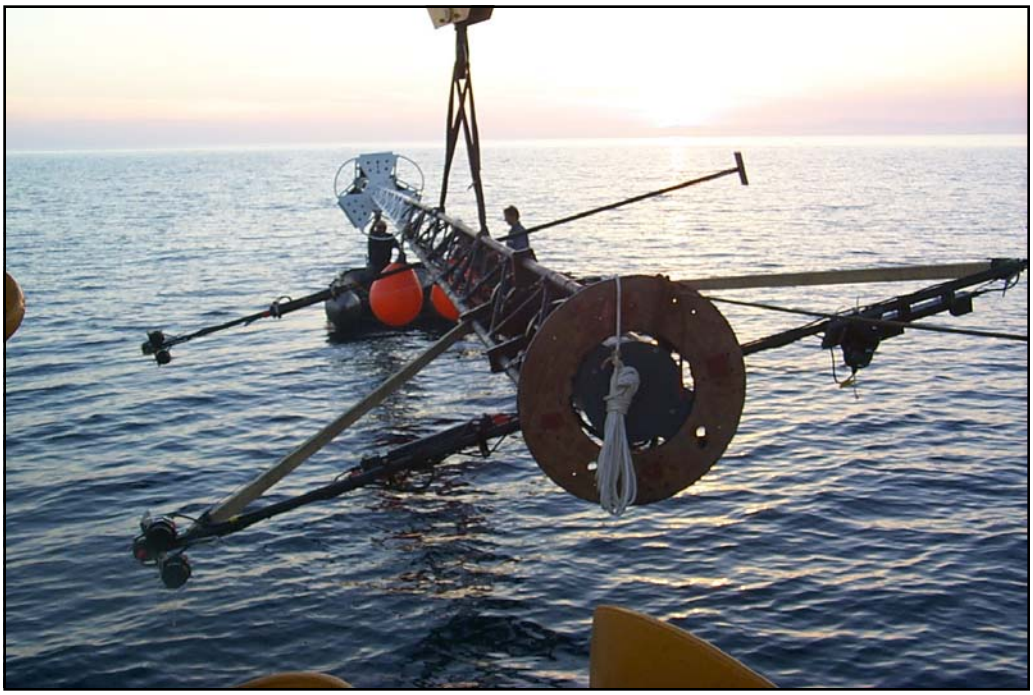

Fig. 10a. The upper superstructure of the buoy (Fig. 6) prior to it being fastened to the lower superstructure, which is done under water by divers. The optical sensors are visible at the end of the sensor arms in the left half of the picture. The two oblique arms are only used during deployment, to secure the buoy arms; they are removed after the buoy is deployed.

Fig. 10b. The buoy completely deployed with the top-most portion of the structure rising approximately 4 m above the water surface (as measured from the bottom of the solar panels).

buoyancy sphere. The second option was selected, and a special design was prepared, with a segmentation of the total volume into seven pressure-resistant and watertight compartments. This design minimizes the risk of rapidly loosing a large part of the buoyancy in case a leak occurs. The upper superstructure is still built with aluminum.

In addition, a strain gauge was installed at the base of the buoy, just at the beginning of the mooring cable. Because the tension in the cable that is recorded by the gauge is, by definition, equal to the buoyancy of the entire mooring, any change in buoyancy can be detected as a change in tension.

5.7 Fall 2003 Deployment

The new version 3 buoy and mooring were deployed 6 September 2003, and the upper instrumented part was recovered three months later (6 December). The behavior of the buoy was as expected, and the data collection was continuously operating during the three-month period, with the exception of a) the transmissometer, which flooded after about 10 days (because of a faulty o-ring seal of the pressure housing); and b) the strain gauge (which was subsequently replaced with a new sensor).

Several storms occurred during the deployment time period. In particular, one had a wind speed of 50 kts, gusts up to 65 kts, and maximum wave heights of about 8 m (such a severe sea state never occurred within the past five years). In such conditions, the strong wind-driven surface current pushes the buoy, which starts to tilt and simultaneously sinks, because the Kevlar mooring cable cannot stretch. After several hours of a strong wind, the buoy simply becomes totally submerged, with the top-most portion of the buoy reaching maximum depths of about 5 m. This situation is not risky for the instrumentation, which is designed to go even deeper, and is actually an effective *mechanism* for protecting the buoy from breaking waves, which are the only potential source of severe damage. After the wind stops, the buoy rapidly *rights* itself and goes back to its nominal position.

The upper superstructure severely suffered from corrosion, the cause of which was the use of improper sacrificial anodes. The faulty anodes were replaced by anodes specifically manufactured for aluminum structures, and corrosion was no longer a problem. The upper superstructure used for this deployment was not considered reusable, so a new one was built in preparation of the next deployment.

5.8 March 2004 Deployment

The upper superstructure of the buoy, which hosts the instrumentation, was reinstalled on 4 March 2004; this should have been done on 4 February, but a last-minute problem with the buoy computer postponed the deployment, and eventually led to a one-month delay. The deployment lasted until 23 July 2004, when the rotation of the upper superstructure took place. Indeed, during the first five months of 2004, a second buoy superstructure was built and a second suite of instrumentation was acquired, in order to allow a bi-yearly rotation of the full equipment. The rotation was performed by combining a ship and divers on site and transportation of buoys from the site to the coast (and vice versa) by helicopter.

5.9 July 2004 to June 2005 Deployment

This deployment lasted 10 months (end of July 2004 to beginning of June 2005). Only a few difficulties arose, mostly due to stops of the acquisition system, requiring replacement by divers of the main buoy computer.

5.10 Full Rotation (June 2005)

During the end of 2004 and the beginning of 2005, a second lower superstructure and a second mooring line were built, in order to prepare for a complete rotation of the entire mooring line and buoy. This operation was primarily motivated by the unknown longevity of the 2 km long Kevlar mooring cable. A 21-month deployment was deemed sufficient for a first check to be performed. Another motivation was to check the integrity of the main buoyancy sphere. The operations took place from 2–3 June (recovery of the mooring and buoy) and 15–16 June (deployment of the new system). The system has been at sea since then.

6. INSTRUMENTATION

The scientific instrumentation are categorized according to the deployment site: buoy (which includes the acquisition system), ship, and coastal. The description of the instruments are separated into sections explaining how the radiometers are characterized and how bio-fouling is minimized on the buoy sensors.

6.1 Buoy Sensor and Acquisition System

In this section, brief descriptions of the buoy sensors and the acquisition system are provided.

6.1.1 Sensors and Data Collection Scenario

Instruments on the buoy, simultaneously collecting data in a continuous way, include the following:

- Satlantic ocean color 200-series radiometers measuring E_d, E_u, and L_u (nadir) at two depths (4 and 9 m);
- A Satlantic Multichannel Visible Detector System (MVDS) 200-series radiometer measuring E_s (at 4.5 above the sea surface);
- An Advanced Orientation Systems, Inc. (Linden, New Jersey) two-axis tilt and compass sensor at 9 m (EZ-III);

- A Sea-Bird Electronics, Inc. (Bellevue, Washington) CTD at 9 m measuring conductivity, temperature, and pressure.
- Chelsea (Surrey, United Kingdom) MINItracka Mk II fluorometers at 4 and 9 m for a proxy for the TChl a concentration, $[\text{TChl } a]$.
- WETLabs C-star transmissometers at 4 and 9 m for the beam attenuation coefficient at 660 nm, a proxy of the particle load.
- A Hydro-Optics, Biology, and Instrumentation Laboratories (HOBI Labs), Inc. (Tucson, Arizona) Hydroscat-II backscattering meter at 9 m measuring a proxy to $b_b(\lambda)$ at two wavelengths (442 and 560 nm).

These data are collected every 15 min during daylight, and at hourly intervals at night. Each data acquisition sequence lasts one minute.

6.1.2 The Integrated Acquisition System

The central recording device of the buoy is the Data Aquisition and Control Network (DACNet) unit, which houses the primary computer: a PC104 Cool RoadRunner II 200 MHz 6×86 with 32 MB of random access memory (RAM) and the serial data acquisition equipment (recording to a 1 GB disk drive). These components are used in the collection, storage, and downloading of the data obtained from the instruments. The majority of the time the system is inactive, and the DACNet unit is unpowered. A small internal microcontroller is responsible for the power supervision and control, and a precision clock.

Optimization of the power budget is an important element, because of the restricted power available from the 12 VDC 105 Ah underwater battery, which is recharged using solar panels. The power managment functions can be summarized as follows:

1. An accurate real-time clock;
2. An alarm clock for powering up the system for the programmed schedule;
3. A watchdog timer that protects against draining the battery in the event of a computer malfunction; and
4. A power-fail shutdown to prevent computer startup if the battery power is too low.

The DACNet operating system runs on Red Hat Linux 6.2 kernel v2.2.19, which accommodates custom-made Java software: the Satlantic Telemetry Acquisition Manager (STAM) and the Satlantic Node Manager. These programs provide the operational, configuration, and interface requirements for the buoy to run autonomously and enable communication of data and files with the user.

A third piece of software, Satlantic Base Manager, runs on a personal computer (PC) equipped with the Windows NT or Windows 98 operating system and provides the operator with administrative tools—each with a graphical user interface (GUI). These tools enable the user to configure the Node Manager, transfer data and files, update the internal clock of the acquisition node, view data from specified instruments in real time, and completely shutdown the acquisition node for maintenance†.

6.1.3 Data Communications

The complete data stream can be downloaded through a wireless ethernet link established between the buoy and the ship (the same equipment is used aboard the buoy and the ship). This link functions with the ship positioned a few hundred meters from the buoy. The connection is driven by the buoy, with a wakeup sequence each hour of the day. This hierarchy was adopted, rather than establishing the communication from the ship, in order to minimize the time during which the buoy communication hardware is awake and consuming energy.

Data retrieval from the buoy is performed from the DACNet via a Cisco Aironet 340 series wireless bridge manufactured by Cisco Systems (San Jose, California) and is stored directly on a PC. The data is retrieved in a binary format and consists of one daily log file for each of the following seven groups: a) the instruments connected to the DATA-100 at 4 m (radiometers and fluorometer); b) the instruments connected to the data acquisition module (DATA-100) at 9 m (radiometers, fluorometer, transmissometer); c) the CTD; d) the Hydroscat-II; e) the strain gauge; f) the MVDS; and g) the two-axis tilt sensor and compass. The daily file is closed once communication through the Cisco system occurs. In this case, a new file is created starting from the next measurement taken by the DACNet system until midnight or until a subsequent link up via the Cisco system is performed. Storage space on the hard disk of the DACNet has the capacity to store up to approximately three months of data.

Part of the data stream is transmitted via the ARGOS system and is used for surveying the functioning of the system; the sample data include the tilt and depth of the buoy, the strain of the mooring cable, the battery voltage, the disk space, the spectrum of the above-water irradiance, and instrument health parameters, which are indicating whether or not instruments and the acquisition system are functioning nominally.

6.2 Shipboard Sensors

In this section, brief descriptions are provided of the instruments deployed from the ship to help characterize the BOUSSOLE site during the monthly maintenance cruises. The objective here is to have quality-assured data for the most important hydrographic, optical (AOPs and IOPs), and biogeochemical parameters.

† More details of this software can be found in Satlantic's manual *DACNet Software Overview—Villefranche Remote Optical Mooring*.

6.2.1 CTD and Water Sampling

The CTD/rosette package is based on a Sea-Bird Electronics (SBE) 911 plus, equipped with the following sensors:

- Pressure (Digiquartz Paroscientific, Inc.);
- Temperature (SBE 3);
- Conductivity (SBE 4);
- Dissolved oxygen (SBE 13 until January 2003, and then an SBE 43); and
- Altimeter (Datasonics PSA 900).

The sensors are mounted on a SBE 32 rosette with 11 12 L Niskin bottles (the 12th being replaced by an AC-9+ as discussed below).

The pressure sensor is not regularly calibrated (it was last calibrated in 1995); it is known from past experience with this type of sensor that the uncertainty is on the order of 0.5 dbar. It is acknowledged that this type of sensor only experiences a drift of the zero point, which is easy to control, and to correct for, when the sensor is at the surface.

The temperature sensor is sent once a year for calibration to SBE, which has the agreement from the National Institute of Standards and Technology (NIST) for this type of work. Figure 11 provides an example of the calibrations performed in January 2002 and January 2003 (was about the same between January of 2001 and January of 2002). The drift is on the order of 0.0025°C over one year, and it is linear. Any temperature value computed between two of these calibrations is, therefore, provided with a ±0.0025°C uncertainty.

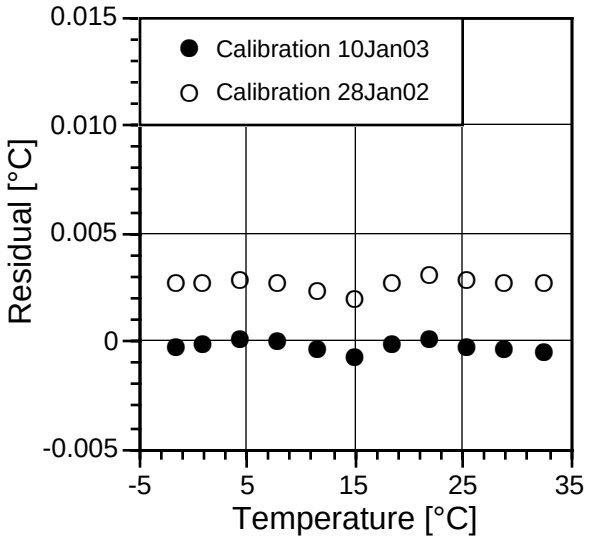

Fig. 11. The calibration drift of the temperature sensor mounted on the CTD.

The conductivity sensor is sent once a year to SBE for calibration. Additional calibration against values determined from water samples and subsequent laboratory analyses (with a laboratory salinometer) are not performed. Figure 12 provides an example of the calibration performed in 2001. The change in the calibration slope is caused by biological fouling that grow inside the sensor, modifying its geometry. The influence of this fouling is larger as the conductivity increases. Typical values of the BOUSSOLE site are on the order of 5 S m^{-1}. It is, therefore, estimated that the sensor drift over one year is on the order of 0.0005 in conductivity units, which corresponds to approximately 0.005 psu. The drift was a bit higher in 2002, around 0.001 in conductivity units, which is about 0.01 psu.

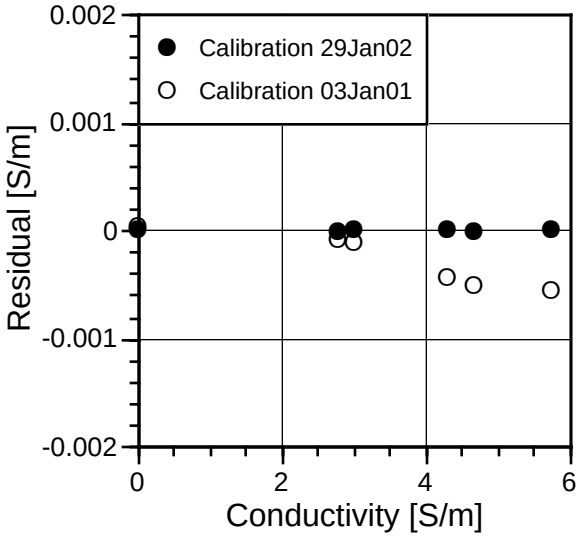

Fig. 12. The calibration drift of the conductivity sensor mounted on the CTD.

From July 2001 to December 2002, a SBE 13 sensor with a Beckman membrane was used. This sensor showed a large drift. Starting in January of 2003, a new sensor was used (SBE 43), which is provided with a nominal 5% uncertainty and a less than 2% drift. No Winkler-based calibrations are performed on these sensors.

At each cast, a first round trip down to 50 m is performed with the CTD, in order to rinse all instruments and equilibrate them in temperature. Then the package is lowered down to 400 m at a descent rate of about 0.5 m s^{-1}. The data are collected at a 24 Hz frequency, and then processed through the SeaSoft software until binned values are produced at a 1 m resolution. Each data file has an associated header file containing the necessary ancillary information (latitude, longitude, date and time of acquisition, meteorological information, etc.).

Some of the sampling depths are fixed (i.e., 5 and 10 m for surface analyses) and others are determined at the end of the rosette descent, based on the phytoplankton fluorescence profile, in order to best represent any specific features of the vertical profile. No sampling is done deeper than 200 m. Bottles are closed during the ascent of the rosette. When back on deck, 2.8 L plastic bottles are used to collect water that is used for subsequent filtration. The filters are kept in Petri slides, wrapped in aluminum and

stored first in liquid nitrogen on board and then in a −80°C freezer in the laboratory. The material collected on filters are used for HPLC analyses of the phytoplankton pigments (Sect. 7.1) and filter pad absorption (Sect. 7.2). For the surface samples, triplicate filtrations are performed for the HPLC analyses.

6.2.2 Fluorometer

A Chelsea Mk III Acquatracka fluorometer is installed on one of the analog channels of the CTD SBE 911. This instrument is equipped with an excitation filter at 430 nm and an emission filter at 680 nm. The data are provided both as voltages and chlorophyll concentrations, the latter being computed with the initial calibration coefficients provided by the manufacturer. These concentrations are just indicators. Another calibration of the fluorometer signal can be performed against the HPLC discrete chlorophyll concentration values.

6.2.3 AC-9

One of the CTD rosette bottles is replaced by a 25 cm path AC-9+ sensor. This instrument measures the absorption and attenuation coefficients of the water at nine wavelengths (Table 1). In order to visualize and collect the data in real time, the AC-9+ is linked to the surface through a 19,200 baud serial connection, which also provides power to the instrument. Although the CTD and AC-9+ can be independently controlled, only one computer is used in order to provide the same time frame and depth measurements to both the hydrographic and optics data. The connection only functions in the computer-to-AC-9+ direction, although theoretically two-way communications are possible. The choice of one-way communications is driven by the different transmission speeds (300 baud from the computer to the SBE 911 and 19,200 baud from the SBE 911 to the AC-9+).

An SBE 25 pump is installed at the entrance of the AC-9+ water circuitry, and it is coupled with the pump that provides water to the CTD conductivity sensor. Both only function when submerged, which is detected when a certain conductivity threshold is reached. The AC-9+ is programmed to start the following acquisition sequence immediately after being powered by the CTD sensor: 15 s time lag before starting acquisition, then a 60 s warming period, then a 60 s period allowing for cleaning of the plumbing components, and then a 35 min data collection period. The latter is enough for the round-trip down to 400 m, including the stops for bottle firing. Note that the starting sequence of 135 s is occurring during the initial round trip down to 50 m. This procedure ensures a progressive and full temperature rise of the electronics and a correct water circulation into the instruments. Data collection is executed using the WETLabs WetView software v5.0a (as provided by the manufacturer).

6.2.4 ECO-BB3

A WETLabs three-channel backscattering (ECO-BB3) meter is connected to one of the auxiliary ports on the AC-9+ (a serial port with a 19,200 baud rate). This sensor emits light at 440, 532, and 650 nm, and measures the backscattered light at the same three wavelengths. Power to the instrument is also provided by the CTD. The data, however, cannot be visualized in real time; they are stored in the AC-9+ memory, and then collected once the rosette is back on deck and the 35 min acquisition sequence of the AC-9+ is terminated.

6.2.5 CDOM WETStar Fluorometer

A WETLabs WETStar CDOM fluorometer is plugged into one of the analog ports of the CTD. This instrument has an excitation wavelength at 370 nm and an emission filter at 460 nm. It is supposed to provide a qualitative measure of the CDOM concentration. It is connected to the plumbing used for circulating water through the CTD sensors; the water goes from the conductivity sensor to the dissolved oxygen sensor, then to the CDOM fluorometer, and finally to the pump. The data are collected in parallel to the CTD data and processed in real time using the SeaBird SeaSoft software. The raw signal is provided as well as a CDOM concentration computed with the calibration coefficients provided by WETLabs.

6.2.6 SPMR and SMSR

The Satlantic SPMR free-fall radiometric profiler has been used at LOV since 1995, and in many other laboratories around the world. The LOV version of this instrument is equipped with two irradiance sensors, collecting the upward and downward plane irradiances (E_u and E_d, respectively) at the following 13 wavelengths: 412, 443, 456, 490, 510, 532, 560, 620, 665, 683, 705, 779, and 865 nm (the latter was replaced by 380 nm after July 2003).

The SPMR Profiler is made of a long pressure case (1.2 m long and 9 cm in diameter) that contains the majority of the system electronics, while the optical sensors are located and separately housed at either end of the cylinder and facing in opposite directions (i.e., up and down in the normal descent orientation). One end of the instrument has buoyant fins to stabilize the free-fall descent of the rocket-shaped device, and the other end has a small annular lead ballast to establish the righting moment of the instrument and to further stabilize the orientation. The amount of lead used provides for a fine tuning of the free-fall velocity.

The light sensors used for measuring irradiance (in units of milliwatts per square centimeter per nanometer), have a black Delrin plate on the end. The plate contains 13 specially-designed, diffuser-based, cosine collectors. Tilt and pressure are recorded at the same frequency as the irradiance measurements (6 Hz).

The SPMR is accompanied by a deck reference sensor (SMSR) which is equipped with the same 13 wavelengths as the SPMR and is based on the same electronics. Data acquisition is synchronized between the SPMR and the SMSR and both operate at the same 6 Hz frequency.

The absolute calibration (Sect. 6.4) of the SPMR and SMSR with respect to NIST-traceable standards is performed every six months in the Satlantic optics calibration laboratory. Temporal stability between calibrations is monitored using a portable light source (Hooker and Aiken 1998) specifically developed for that purpose by Satlantic, i.e., the second-generation SeaWiFS Quality Monitor (SQM-II). Combining these two elements allows a 3% maximum uncertainty to be maintained on the calibration of the SPMR and SMSR.

A SPMR profile starts when the instrument reaches a distance of 50 m off the stern of the ship (the ship is 25 m long and a mark on the cable indicates the 50 m distance). The instrument is then released and falls at approximately $0.5\,\mathrm{m\,s^{-1}}$. The descent is stopped when the pressure sensor indicates a depth of about 150 m (except in extremely clear waters wherein the profile is performed down to 200 m). This technique ensures data collection out of the ship shadow, and to obtain measurements with tilt angles less than 2°. The Sun is usually on the port side of the ship, which is not so important because the ship shadow is not affecting the measurements.

6.2.7 SIMBADA

The SIMBADA instrument is an above-water radiometer designed and manufactured by the University of Lille, France. It is an upgraded version of the SIMBAD (Deschamps et al. 2004) above-water radiometer. It measures both water-leaving radiance and aerosol optical thickness in 11 spectral bands centered at 350, 380, 412, 443, 490, 510, 565, 620, 670, 750, and 870 nm by viewing the ocean surface (ocean-viewing mode) and the Sun (sun-viewing mode) sequentially. The same optics (3° field-of-view), interference filters, and detectors are used in both ocean- and sun-viewing modes, but different electronic gains are used for each mode. The optics are fitted with a vertical polarizer, to reduce reflected skylight when the instrument is operated in ocean-viewing mode. A small GPS is fixed in the front panel of the SIMBADA for automatic acquisition of geographic location at the time of data collection. Viewing angles are recorded automatically.

Viewing of the ocean must be made in clear-sky conditions (3/4 of sky cloudless, and no clouds obscuring the Sun), outside the sun glint region (relative angle between solar and viewing directions of 45–90°), and at a nadir angle of approximately 45°. For those angles, reflected skylight is minimized, as well as residual ocean polarization effects. The measurements can be made on a vessel underway, so there is no need to stop the ship to make measurements. To normalize water-leaving radiance, incident solar irradiance is not measured, but computed using the aerosol optical thickness.

The operator can select, in addition to ocean- and sun-viewing modes, dark current, and calibration modes. Each series of measurements lasts 10 s. The frequency of the data sampling is approximately 8 Hz. The recorded data are stored internally and downloaded using a computer serial link at the end of the day or a cruise. The instrument is powered by batteries that can be charged using a main supply of 110–240 V, 50–60 Hz. About 2 h of charging is usually enough for one day of measurements.

The SIMBADA is used from the bow of the ship or from the upper superstructure when the weather permits, which are the two more convenient locations sufficiently high above the sea surface. This is important, because any ship perturbations (shadow or reflections) are minimized when increasing the vertical distance between the operator and the sea surface, and then the horizontal distance between the spot measured on the sea surface and the ship's hull.

The execution of a full sequence of measurements is as follows:

1. Three dark current recordings (10 s each);
2. Three sun-viewing recordings (10 s each) for derivation of the aerosol optical thickness;
3. Three or four sea-viewing recordings (10 s each);
4. Three sun-viewing recordings (10 s each) for derivation of the aerosol optical thickness; and
5. Three dark current recordings (10 s each).

6.3 Coastal Sensors

An automatic sun-tracking photometer model CE-318 constructed by CIMEL Electronique is installed at the *Cap Ferrat* coastal site (Fig. 1). It has five standard filters for 440, 675, 870, 940, and 1,020 nm and a polarized filter for 870 nm. The instrument activates every 15 min between 0200 and 1400, but the exact measurement scheduling is preprogrammed by AERONET. The program consists of basic direct sun measurements—triplet observation, standard measurement and Langley (plus basic sky measurements), Langley sky, almucantar, polarization, and principal plane. The procedures for data collection are as described on the AERONET Web site†.

6.4 Radiometer Characterization

Characterization and calibration of field radiometers are crucial elements of a calibration and validation program for ocean color remote sensing satellites. The activities performed in this segment are outlined in the following three subsections.

† Full details are available at `http://aeronet.gsfc.nasa.gov`.

6.4.1 Absolute Calibration

The absolute calibration of the SPMR and SMSR with respect to NIST-traceable standards is performed every six months in the Satlantic optics calibration laboratory (Halifax, Canada). The objective of the absolute calibrations is to find a coefficient for each sensor to relate the raw instrument voltages (in digital counts) to the actual physical quantity of the parameter being measured in that environment. The method for doing this for radiance and irradiance sensors varies slightly and has been documented by Hooker et al. (2002a).

For a radiance sensor (identified by $S_{\rm ID}$), the calibration coefficient is computed using a plaque (identified by $T_{\rm ID}$) with a calibrated reflectance, $R^{\rm cal}_{T_{\rm ID}}$ along with a standard lamp (identified by $L_{\rm ID}$) that has a calibrated irradiance, $E^{\rm cal}_{L_{\rm ID}}(\lambda)$. As a general procedure, the lamp is required to be positioned on axis and normal to the center of the plaque at a distance d. Dark digital voltage levels are recorded with the radiance sensor capped and an average dark level, $\bar{D}_{S_{\rm ID}}(\lambda)$, is taken from these dark samples.

The radiance sensor position allows a 45° view of the plaque with respect to the lamp illumination axis. Once the lamp is powered on, the voltage levels of each of the individual sensor channels are recorded. From these, an average calibration voltage for each channel, $\bar{V}_{S_{\rm ID}}(\lambda)$, is obtained. The calibration coefficient is calculated as:

$$C^{\rm Rad}_{S_{\rm ID}}(\lambda) \;=\; \frac{\frac{1}{\pi} R^{\rm cal}_{T_{\rm ID}}(\lambda)\, E^{\rm cal}_{L_{\rm ID}}(\lambda, 50)}{\bar{V}_{S_{\rm ID}}(\lambda) \;-\; \bar{D}_{S_{\rm ID}}(\lambda)} \left[\frac{50}{d}\right]^2, \qquad (1)$$

where, d is given in centimeters.

For an irradiance sensor (identified by $S_{\rm ID}$), the calibration coefficients are computed using an FEL standard lamp ($L_{\rm ID}$) with a calibrated irradiance $E^{\rm cal}_{L_{\rm ID}}(\lambda, 50)$. As a general procedure, the lamp is required to be on axis and normal to the face plate of the irradiance sensor at a distance, d. Similar to the radiance sensor, dark voltage levels (digital counts) are recorded with the radiance sensor capped and an average dark level, $\bar{D}_{S_{\rm ID}}(\lambda)$, is obtained from these dark samples.

With the lamp powered on, the voltage levels of each of the individual sensor channels are recorded. From these, an average calibration voltage for each channel, $\bar{V}_{S_{\rm ID}}(\lambda)$, is obtained. The calibration coefficient is calculated as:

$$C^{\rm Irr}_{S_{\rm ID}}(\lambda) \;=\; \frac{E^{\rm cal}_{L_{\rm ID}}(\lambda, 50)}{\bar{V}_{S_{\rm ID}}(\lambda) \;-\; \bar{D}_{S_{\rm ID}}(\lambda)} \left[\frac{50}{d}\right]^2, \qquad (2)$$

where, d is given in centimeters.

6.4.2 Stability

The methodology and equipment used for tracking the stability of the main field radiometers is presented in the following three subsections.

6.4.2.1 The SQM-II

The SQM-II is a portable, stable light source based on the design principles established by NASA and NIST with the original SQM (Johnson et al. 1998). The SQM-II was refined and built by Satlantic, Inc. The SQM-II consists of a lamp housing and a power source (deck box), which are connected by a 5 m cable. A serial port provides the capability of monitoring and controlling the system with a PC. An internal memory, a liquid crystal display (LCD), and several buttons on the back allow manual control and monitoring. Several status light-emitting diodes (LEDs) are also used to provide a visual determination of the operational state of the instrument.

The SQM-II has two sets of eight bulbs each. There is no individual bulb control, a set is either completely turned on or off. The light output of the second set, called the high power bank, is about three times brighter than the light output of the first set, named the low power bank. They are often referred to as HiBank and LoBank, respectively. These two lamp banks provide three illumination levels: low illumination when only LoBank is on, medium illumination when only HiBank is on, and high illumination when both lamp banks are on.

A sensitive internal detector at 490 nm is used to monitor the stability of the lamps. The output from this detector and other internal sensors measuring temperatures, voltages and currents are monitored by a 20-bit analog-to-digital converter. The SQM-II setup is described in the *SQM-II User's Manual*.

6.4.2.2 Methodology

To check the stability of the different radiometers in the field and to monitor the performance of the SQM-II itself, a calibration evaluation and radiometric testing (CERT) session and a data acquisition sequence (DAS) have been defined following the procedure described in Mueller and Fargion (2002). A CERT session is a sequence of DAS events, which are executed following a prescribed methodology. Each DAS lasts for 3 min to represent enough data to statistically establish the characteristics of the instrument involved, referred to as a device under test (DUT). This records about 1,000 DUT records and 450 SQM-II records. A typical sequence for each CERT session is as follows:

1. The equipment (lamp power supplies, the SQM-II fan and internal heater power supplies, lamp timers, etc.) is turned on at least 1 h before the CERT session begins. The total number of hours on each lamp set are tracked by recording the starting and the ending of hours on each lamp set. Each lamp bank functions separately, so the state of a given lamp bank is independent of the state of the other bank.

2. The SQM-II lamp bank will remain in this coarse stability state for 1 h, allowing enough time for the lamp and the system to thermally stabilize. It is not recommended that radiometer measurements be taken while in this state because the lamps have not yet reached their highest stability. After one hour, the lamp banks will automatically enter the fine stability state.
3. If the mixture of radiometers used in the CERT session changes over time, at least one radiometer (preferably two of different types, i.e., radiance and irradiance) should be used in all CERT sessions. This would be practically the case when the SPMR system and the buoy radiometers are not calibrated during the same CERT.
4. S. Hooker advises to keep the banks in the fine stability state for another hour before starting the CERT, particularly in highly variable environments. This advice was followed even if the CERT took place in a laboratory. The warm-up period can be considered completed when the internal SQM-II monitor data are constant within 0.1%. The radiometric stability usually coincides with a thermal equilibrium as denoted by the internal thermistors.
5. Inserting a DUT into the SQM-II produces a small reflective loading effect on the light chamber (i.e., some light is reflected back into the light chamber), which affects what the radiometer detects. The reflectivity of a field radiometer, however, is constantly changing over time, because of the normal wear and tear associated with use, which alters the loading effect on the SQM-II monitor detector and the effective light field seen by the radiometer.
6. Upon completion of the warm-up period, SQM-II monitor data are collected for the black glass (radiance) and white (irradiance) fiducials successively. A fiducial is a nonfunctional DUT, whose reflective surface must be carefully maintained over time so that its reflectivity remains essentially constant. It is also important that the position of the fiducial in the compartment is always the same and this is ensured by a fixed collar allowing only one position.
7. Once these control measurements are completed, the individual radiometers (DUTs) are then tested sequentially. This begins with an OCR-200 that is designated specifically for use with the SQM-II and nothing else. Its use is restricted solely to SQM-II sessions to preserve the performance of its original calibration and, hence, serve as a verification of SQM-II stability between sessions.
8. First, the DUT sensor head is inserted and secured in the SQM-II compartment. Data is collected over 3 min. The DUT is secured using the three fasteners on the SQM-II, which clamp on a collar that has been fastened to the DUT. This collar is at a specific distance from the sensor head and of a particular rotational position, determined by the flat side of the collar. This positioning of the flat part of the collar ensures that the DUT always enters the SQM-II in exactly the same way.
9. The DUT is removed from the SQM-II slot and the caps are placed over the sensor heads to block out all possible light to the them. The black fiducial is then placed in the SQM-II and data is again collected from both SQM-II and DUT to provide a dark reading for the DUT and stability check for the SQM-II. Each time any file is recorded, the voltage at the SQM-II internal detector is noted.
10. Once all instruments are tested, the SQM-II monitor data are collected a second time using the black, radiance, and irradiance fiducials successively.
11. As soon as all measurements with a lamp bank are complete and its use is no longer required, the lamps are switched off to minimize aging and possible deterioration. Where an alternative lamp bank combination is required for testing DUTs at a different light intensity, 2 h warm-up time is once again required to reach optimum stability.
12. The practice of using all three light intensity levels was discontinued in 2003, because SQM-II performance changes caused the internal detector of the SQM-II to saturate during HiBank operation, so HiBank measurements were omitted.
13. Before the SQM-II is finally shut down and the CERT session completed, after the lamps are powered down, the ending number of hours on each lamp set is recorded.

The SQM-II operation is precisely described step by step in the *SQM-II User's Manual* edited by Satlantic, although some changes have been made to the method presented here to reduce the duration of each SQM-II session and to accommodate the aforementioned internal detector saturation during HiBank operation.

6.4.2.3 Measurement Schedule

The objective of the scheduling of the SQM-II operations is to monitor the variability and drift of the radiometers during the period of use between the (approximately) biannual absolute calibrations performed by Satlantic in Canada. The data collected in these SQM-II sessions aids in the reduction of uncertainties in the field data caused by changes in the performance of the sensors between calibrations. When differences occur between calibrations, it cannot be assumed that this change has been a gradual and linear process during the period of activity. As soon as possible after the radiometers are received at LOV from Satlantic, they are tested on the SQM-II in the LOV optics laboratory using the method described in Sect. 6.2.2.

Once the sensors have been used in the field, either fixed on the buoy or profiled from the ship, they are subjected to testing on the SQM-II. The exact scheduling of this testing depends on the duration of the field work. For the buoy radiometers, which are intended to be exchanged on a monthly basis, the SQM-II session is performed as soon as possible after they have been taken off the buoy and returned to the lab (once they have been wiped down with soapy water and a soft cloth). For the SPMR and SMSR, the SQM-II session is performed after each cruise.

6.4.3 Immersion Factors

The eighth SeaWiFS Intercalibration Round-Robin Experiment (SIRREX-8) conclusively demonstrated that immersion factors must be determined for each sensor if a less than 3% the uncertainty in irradiance determinations is to be achieved (Zibordi et al. 2002b). A water tank based on the Hooker and Zibordi (2005) design—the so called Compact Portable Advanced Characterization Tank (ComPACT)—was developed and is used for characterizing buoy radiometers.

The objective here is to determine specific sets of coefficients for the radiometers, and, more importantly, to check whether these coefficients are changing over time because of their prolonged deployments at sea. For the moment, the results of these experiments do not show appreciable changes, although confirmation by additional measurements is still pending. More definitive conclusions also depend on future improvements in the reproducibility of the experiments, in order to meet the requested performance levels (Hooker and Zibordi 2005).

6.5 Bio-Fouling

Bio-fouling is a critical aspect of mooring applications. The development of new systems for preventing bio-fouling (chemicals or mechanisms) has not been considered in the project, at least up to now. Minimizing bio-fouling on instruments first requires that the structure they are installed on is kept clean. When the mounting structure is bio-fouled, algal growth restarts more rapidly after the instruments are cleaned, so an effective antifouling paint on the buoy superstructure is required.

Concerning the radiometers, the quality of their measurements is preserved by the following ways:

- Copper sheets have been added around the radiometers' bodies (since June 2005).
- The sensors are cleaned during each monthly maintenance visit by divers equipped with brushes (since July 2006, the cleaning has been performed approximately every two weeks).
- Diffusers or filters are replaced if the absolute calibration indicates it is timely to do so. This operation can be performed after the upper superstructure rotations, which occur about twice a year.
- Glass windows of the radiance sensors are kept as clean and smooth as possible, which is the best antifouling procedure following McLean et al. (1997).

The above procedures are considered sufficient, at least as a first approach, especially given the oligotrophic-to-mesotrophic character of the mooring site. The cleaning of the radiometers every two weeks is the central element in the strategy to eliminate bio-fouling effects from the measurements of radiometric quantities. Concerning the transmissometers, copper rings have been installed around the emission and reception windows. A copper face plate has been installed onto the Hydroscat-II.

All the above devices and procedures have proven to be efficient but cannot totally eliminate bio-fouling, so that corrections for possible residual effects will have to be applied. The total effect of bio-fouling, which can be determined from the comparison of the measurements taken just before and just after cleaning of the sensors, will have to be distributed over time in some manner.

7. DATA ANALYSIS

Data analyses procedures are summarized in the following six subsections. This part is not meant to be exhaustive; only the analyses considered as the most important are presented.

7.1 HPLC

The methods described here were evaluated as part of three international SeaWiFS HPLC Analysis Round-Robin Experiment (SeaHARRE) exercises: SeaHARRE-1 (Hooker et al. 2000), SeaHARRE-2 (Hooker et al. 2005) and SeaHARRE-3 (Hooker et al. 2007). The round robins were based on both natural samples and standard mixtures representing a wide range of Chl a concentrations from the hyper-oligotrophic conditions of the Mediterranean Sea and South Pacific Gyre to the very eutrophic waters of the Benguela, Moroccan, and Chilean upwelling systems. Four to eight laboratories from seven countries have taken part in these activities.

As a result of these exercises, the LOV has demonstrated that satisfactory results are provided for the analysis of Chl a and accessory pigments in seawater samples from different concentration regimes: the method used undergoes detailed quality control procedures, and a series of validation parameters are regularly monitored in order to ensure a good continuity in the data.

7.1.1 Sample Collection

Seawater samples were collected from Niskin bottles and filtered through 25 mm GF/F Whatman filters (0.7 µm porosity). In most cases, 2.8 L were filtered for each sample and the filters were placed in Petri slides, wrapped in aluminium and stored first in liquid nitrogen on board and then in a $-80°$C freezer in the laboratory.

7.1.2 Extraction Procedure

Each filter is placed in 3 mL of methanol (HPLC grade) containing an internal standard†. After 30 min at −20°C, the filters are disrupted by ultrasonication using an ultrasonic probe and returned to the freezer. Another 30 min later, the sample is clarified through a 25 mm GF/C Whatman filter (1.2 µm porosity). The filtrate is finally stored at −20°C until analysis (within 24 h).

7.1.3 HPLC Analysis

All parts of the HPLC system at the LOV are Agilent Technologies products:

- A degasser (1100 model);
- A binary pump (1100 model);
- An autosampler (1100 model) with built-in temperature control (4°C) and automatic injection (Rheodyne valve) for mixing the sample with the ammonium acetate (1 N) buffer;
- A diode array detector (1100 model) with measurements at 222 nm (for the vitamin E acetate internal standard), 440 nm (for carotenoids), and 667 nm (for chlorophylls and degradation products); and
- A fluorescence detector with excitation and emission wavelengths at 417 and 670 nm, respectively.

Two successive analytical methods have been used for pigment analysis. The first method is based on a gradient separation between a methanol:ammonium acetate (70:30) mixture and a 100% methanol solution, comparable to that described by Vidussi et al. (2000), but with a few differences allowing for improvement of sensitivity and peak resolution. Modifications to this method to separate certain peaks and increase sensitivity included a) a flow rate of 0.5 mL min^{-1}, and b) a reversed phase chromatographic C_8 column with a 3 mm internal diameter (Hypersil MOS 3 µm). The gradient used is presented in Table 3. Column temperature is maintained at 25°C and the injection volume is 200 µL.

The second method is also a gradient separation between a methanol:tetrabutyl-amonium acetate (70:30) mixture and a 100% methanol solution, comparable to that described by Van Heukelem and Thomas (2001), except for a few differences allowing improvement of the sensitivity and peak resolution. Modifications to this method include a) a flow rate of 0.55 mL min^{-1}, b) a reversed phase chromatographic C_8 column with a 3 mm internal diameter (Zorbax Eclipse XDB, 3.5 µm). The gradient used is presented in Table 3. Column temperature is maintained at 60°C and the injection volume is 250 µL.

† Samples before March 2003 were analyzed with *trans*-β-apo-8′-carotenal as the internal standard, which was replaced with vitamin E acetate.

Table 3. The gradient used with the HPLC column. The time is in minutes, and the percentages of solvents A and B are given in the last two columns.

Step	*Time*	A [%]	B [%]
1, Start Method 1	0	80	20
2	4	50	50
3	18	0	100
4, End Method 1	22	0	100
1, Start Method 2	0	90	10
2	25	5	95
3, End Method 2	28	5	95

The different pigments that are quantitated are presented in Table 4.

7.1.4 Calibration

Response factors for eight pigment standards provided by DHI Water and Environment (Hørsholm, Denmark) are determined by spectrophotometry (Perkin Elmer) followed by HPLC analysis:

1. Peridinin,
2. 19′-Butanoyloxyfucoxanthin,
3. Fucoxanthin,
4. 19′-Hexanoyloxyfucoxanthin,
5. Alloxanthin,
6. Zeaxanthin,
7. Chlorophyll *b*, and
8. Chlorophyll *a*.

These response factors are then derived to compute the specific absorption coefficients of these eight major pigments for the HPLC system.

Specific absorption coefficients for divinyl chlorophyll *a* and divinyl chlorophyll *b* are computed knowing a) the specific extinction coefficients of chlorophyll *a* and chlorophyll *b*; b) the measurement of the absorption of chlorophyll *a* and divinyl chlorophyll *a* (or chlorophyll *b* and divinyl chlorophyll *b*) at 440 nm when the spectra of both pigments are normalized at their red maxima; and c) that both pigments are considered to have the same molar absorption coefficient at this red maxima. For the remaining pigments, their specific extinction coefficients were either derived from previous calibrations or from the literature (Jeffrey and Vesk 1997).

7.1.5 Quantitation

The Agilent Technologies Chemstation software is used for conducting the analysis, as well as for post-analysis processing. This includes peak integration and spectral identification. Peak identification is manually verified by retention time comparison and observation of the absorption spectra. Quantification is based on peak area related to the

Table 4. The list of pigments detected by HPLC at the LOV, their detection wavelengths, and their possible coelution with another pigment. The variable forms, which are used to indicate the concentration of the pigment or pigment association, are patterned after the nomenclature established by the Scientific Committee for Oceanographic Research (SCOR) Working Group 78 (Jeffrey and Vesk 1997). Abbreviated forms for the pigments are shown in parentheses.

Variable	*Pigment*	*Detection*	*Coelution*
[Chl c_3]	Chlorophyll c_3 (Chl c_3)	440 [nm]	
[Chlide a]	Chlorophyllide a (Chlide a)	667	Coelutes with Chlorophyll c_{1+2}
[Chl c_{1+2}]	Chlorophyll c_{1+2} (Chl c_{1+2})	440	
[Phide a]	Phaeophorbide a (Phide a)	667	Coelutes with Peridinin
[Peri]	Peridinin (Perid)	440	
[But]	19′-Butanoyloxyfucoxanthin (But-fuco)	440	
[Fuco]	Fucoxanthin (Fuco)	440	
[Hex]	19′-Hexanoyloxyfucoxanthin (Hex-fuco)	440	
[Neo+Vio]	Neoxanthin and Violaxanthin (Neo+Viola)	440	Coelution Pair
[Diad]	Diadinoxanthin (Diadino)	440	
[Allo]	Alloxanthin (Allo)	440	
[Diato]	Diatoxanthin (Diato)	440	
[Zea]	Zeaxanthin (Zea)	440	
[Lut]	Lutein (Lut)	440	
[Chl c_1]	Nonpolar chlorophyll c_1 (Chl c_1)	440	
[TChl b]	Total chlorophyll b† (TChl b)	440, 667	Coelution Pair
[Croco]	Crocoxanthin (Croco)	440	
[DVChl a]	Divinyl chlorophyll a (DVChl a)	440	
[Chl a]	Chlorophyll a‡ (Chl a)	440, 667	
[Chl c_2]	Nonpolar chlorophyll c_2 (Chl c_2)	440	
[Caro]	Carotenes§ (Caro)	440	Coelution Pair
[Phytin a]	Phaeophytin a (Phytin a)	667	

† The sum of divinyl chlorophyll b and monovinyl chlorophyll b.

‡ The sum of monovinyl chlorophyll a plus allomers and epimers.

§ The sum of $\beta\beta$-Car plus $\beta\varepsilon$-Car.

specific extinction coefficient and concentrations are given in milligrams per cubic meter. When two pigments tend to coelute, their identification is first done spectrally then they are summed, e.g., chlorophyll c_{1+2}, or total chlorophyll b (chlorophyll b plus divinyl chlorophyll b).

7.1.6 Validation

A solution of methanol containing the internal standard is injected every 12 samples during the analytical sequence. The average of these *control* analyses provides the reference peak area for the internal standard. The standard deviation of these analyses provides information about the precision, as well as the stability of the instrument during the analytical sequence. Total Chl a (TChl a) values are compared to the fluorescence signal from CTD bottle data in order to detect possible inaccuracies. TChl a values are also compared to particulate absorption measurements, which have been carried out on the same filters just before pigment extraction (Sect. 7.2).

7.1.7 Method Performance

This HPLC analytical method has proved to be particularly sensitive, with detection limits of approximately $0.0004\,\mathrm{mg\,m^{-3}}$ for [Chl a] and a resolution between divinyl chlorophyll a and chlorophyll a greater than 1.5, which allow it to be particularly adapted to the oligotrophic waters of the Mediterranean. The precision of the method is characterized by a variation coefficient of about 0.4%.

7.2 Filter Pad Absorption

The following two subsections describe the measurement of absorption by particles, which is performed on the

same filter that is subsequently used for the HPLC pigment analysis previously described.

7.2.1 Laboratory Analyses

The protocol for analyzing the spectral absorption coefficients of particulates is based on the NASA *Ocean Optics Protocols for Satellite Ocean Color Sensor Validation* (Mitchell et al. 2003). Sampling is performed in the same way as for the HPLC pigments as described in Sect. 8.1 where the seawater samples are collected from Niskin bottles and filtered through 25 mm GF/F Whatman filters (0.7 µm porosity). In most cases, 2.8 L are filtered for each sample and the filters placed in petri slides, wrapped in aluminum foil and stored first in liquid nitrogen on board, and then in a −80°C freezer in the laboratory. The sample filters used for the A_p analysis are also used afterwards for HPLC analysis. This method has been tested to ensure that using the same filter for the two methods does not compromise either measure.

The spectrophotometer used is a Perkin Elmer Lambda 19 (L19) dual-path spectrometer with an integrating sphere compartment attached. The instrument scan range is set from 750–350 nm with a scan interval of 1 nm. After a 1 h warm-up period, the machine is ready to use. The samples are taken out of the −80°C freezer and stored temporarily in an ice-cooled cold box. Each sample, in its petri dish, is then placed in a dark box on the bench to defrost for 5 min. This defrosting period is kept to a minimum because the pigment composition once thawed becomes susceptible to degradation which could effect the analyses, particularly the HPLC.

The L19, being a dual-path spectrometer, has a slot for a reference material and another for the sample. These slots are actually the outer walls of the integrating sphere at the two positions where the two beams enter the sphere. For the reference path, rather than use a blank filter, which can create variations in the spectra attributable to differences in the level of moistness of the filter, the pathway is left open (without any filter blank), thus using an *air blank*. In the sample material slot, a blank GF/F filter is used. This blank has been soaked in distilled water for 12 h and had excess water drained off before being placed in the sample slot.

An *autozero* is performed with the blank filter in the sample path and the reference path open, which sets the absorbance values measured at each wavelength to zero. As a verification of this and to provide a baseline, the blank is then scanned to measure absorbance. The spectra produced from this should be flat and close to zero (within 0.005). If this is not the case, the autozero is repeated and the blanks scanned again.

Once satisfactory baselines are achieved, then the sample filters can be scanned. For both cases, two scans are made, which should produce two similar replicates. If similarity is not found, the filter position is checked and the sample scanned again. Drying of the filter between replicates may cause some vertical offsetting, which is acceptable if the spectral shape for each replicate is similar.

The spectra are saved as a file in American Standard Code for Information Interchange (ASCII) format with two columns: wavelength and absorbance. The mean of the absorbance values of replicates for each sample is calculated and any offset from zero removed by subtracting the absorbance value at 750 nm from the entire spectrum.

7.2.2 Data Postprocessing

The optical densities are then corrected for any nonzero signal in the NIR (750 nm), and transformed into absorption coefficients by accounting for the so-called β effect. The total particulate absorption spectra are then numerically decomposed into a phytoplankton and a detritus absorption spectra following Bricaud and Stramski (1990).

7.3 Total Suspended Matter (TSM)

TSM is determined with a gravimetric method based on the protocol described by Strickland and Parsons (1972). Before sampling, 25 mm diameter Whatman GF/F glass fiber filters (0.7 µm particle retention size) are pre-rinsed in methanol, pre-combusted at 450°C for 4 h, and preweighed to six significant digits with a Metler-Toledo electrobalance (ambient temperature and humidity are also recorded).

In the field, 1.5–5.6 L seawater samples (the chosen volume depends on the amount of material in the water) from below the surface are collected in triplicate using vacuum filtration. The filters and filter-rims are rinsed with 20–30 mL of milli-Q water in order to eliminate the presence of salt crystals. They are placed in polycarbonate petri dishes and stored in liquid nitrogen and at −80°C until laboratory analysis. The filters are dried in an oven at 75°C for 24 h and placed in a dessicator before being weighed to six digits of precision (ambient temperature and humidity are recorded). The TSM is calculated as the difference between the sample weight minus the weight before filtration (in grams), and then divided by the filtration volume in cubic meters (concentrations are, therefore, grams per cubic meter).

7.4 AC-9 and ECO-BB3 Data Processing

When a CTD cast is performed, the CTD and AC-9+ start times are not synchronized. In addition, each instrument has a specific time constant and the water circulation in the tubing generates additional temporal offsets. In order to account for these time lags, the vertical profiles for absorption and attenuation must be shifted in order to match the vertical profiles of other data such as the chlorophyll fluorescence and the temperature. The matching is either performed *manually* using clearly identifiable features in the profiles (i.e., peaks) or *automatically* when the time lag between the start of the various

instruments is accurately known. Once the vertical shift has been determined for the AC-9+ data, it is also applied to the ECO-BB3 data.

When all data have been matched in the vertical, the data processing for the AC-9+ essentially follows the protocol described in the WETLabs *AC-9+ User's Guide*, in terms of temperature, salinity, and scattering corrections (for the latter, the so-called *method 3* is used). For the ECO-BB3, the data processing follows the protocols described in the Wetlabs *Scattering Meter, ECO-BB User's Guide*.

For the AC-9+ data, temporal drifts in the absolute calibration of the device (from cruise to cruise) are corrected as described in Oubelkheir et al. (2005), i.e., average absorption and attenuation spectra are determined over depths from 350–400 m immediately after an absolute calibration. These spectra are then used as reference spectra, i.e., all spectra subsequently measured at 400 m are constrained to be equal to the reference spectra. Any subsequent deviation of the coefficients measured at 400 m from these references is attributed to an instrument drift. The deviation, if any, is simply removed from the entire profile.

At the end of these processing steps, a verification of the AC-9+ absorption data is performed by comparing the values at 676 nm to the phytoplankton absorption at the same wavelength, as derived from discrete samples (Sect. 7.2). Attenuation at 660 nm is also compared to the beam attenuation coefficient determined by the C-Star transmissometer (installed on the CTD package since the beginning of 2006).

7.5 AOPs from SPMR Profiles

The SPMR is a central element in the BOUSSOLE activity. It provides reference data against which the data collected from the buoy can be checked, and it also provides water column information that is unobtainable from the buoy (near-surface) measurements.

7.5.1 Measurement Suite

What is measured in the water column is the upward irradiance, $E_u(z,\lambda)$, at 13 wavelengths from 412–865 nm (Table 1), plus the downward irradiance at the same wavelengths, $E_d(z,\lambda)$. The latter is not used in the computation of the reflectance. The above-water downward irradiance, E_s, which is often referred to as a *deck cell* measurement, because is recorded on deck (in this case at the bow of the ship) and again at the same 13 wavelengths.

7.5.2 Corrections and Extrapolations

From the vertical profile of $E_u(z,\lambda)$, the upward irradiance at *null* depth (0^-), i.e., *immediately below the sea surface*, is obtained as (λ is omitted for brevity):

$$E_u(0^-) \;=\; E_u(z_0)\, e^{z K_u}, \tag{3}$$

where z is depth, $E_u(z_0)$ is the shallowest value of $E_u(z)$ for which the tilt is less than 2°, and K_u is the diffuse attenuation coefficient for the upward irradiance computed from the measurements of $E_u(z)$ collected at different depths between z_0 and $z_0 + 20$ m.

Several interpolation procedures designed to derive the $E_u(0^-)$ from the vertical profile of $E_u(z)$ have been tested against *true* values of $E_u(0^-)$ (i.e., values directly measured below the sea surface by installing the radiometer on a floating frame), and the method that eventually provided the closest values to the *true* ones was selected. This experimental work, which is not further detailed here, is just mentioned to indicate that the contribution to the overall uncertainty budget of the extrapolation error is tentatively minimized.

The above-water solar reference data, E_s, are corrected to account for the loss of irradiance at the air–sea interface:

$$E_d(0^-) \;=\; E_s\, \frac{1 \;-\; \bar{\rho}}{1 \;-\; \bar{r}R}, \tag{4}$$

where the mean transmission of the sea surface for sky and Sun irradiance, expressed by $1-\bar{\rho}$, is equal to 0.957 (±3% according to atmospheric turbidity and solar elevation), and the internal reflectance (accounted for by $1-\bar{r}R$, where is $\bar{r} = 0.489$), varies slightly with R. With a mean R value of 3% this term is equal to 0.985 (±1.5% if R varies between 0–6%). Assuming these two terms are constant,

$$E_d(0^-) \;=\; 0.97\, E_s, \tag{5}$$

where the value of E_s is obtained from the first 10 s of recording starting after the release of the SPMR (this corresponds approximately to the upper 5 m of the descent), to which a fit is adjusted in order to eliminate variations in E_s, which are only due to the tilt of the SMSR (which is not installed on a gimbal). This technique provides similar results as compared to just picking the measurements taken for tilt angles less than 1°.

7.5.3 Computed Parameters

The reflectance R is then

$$R \;=\; \frac{E_u(0^-)}{E_d(0^-)}, \tag{6}$$

remembering that before the above ratio is formed, $E_u(0^-)$ is corrected for instrument self shading as per Gordon and Ding (1992). In this correction, the instrument radius, the total absorption coefficient, and the ratio between the direct-sun and diffuse-sky irradiances (r_d) are taken into account. All of the Satlantic sensors used here have a common radius (4.5 cm), the absorption is computed following Morel and Maritorena (2001) using the measured Chl *a* concentration, and r_d is computed following Gregg and Carder (1990).

An average diffuse attenuation coefficient for the downward irradiance in the upper layers is computed as

$$K_d = -\frac{\log\left[E_d(z)/E_d(0^-)\right]}{z}, \quad (7)$$

where z is taken equal to be 20 m to ensure that the perturbations of the light field caused by surface waves are not introducing errors into the computation.

7.6 Buoy Data Preprocessing

The binary log files for the instruments connected to the DATA-100s are converted by a program called `Satcon` into ASCII format files. The `Satcon` program uses the calibration coefficients and format information in the calibration (`*.cal`) files, created by Satlantic during the most recent absolute calibration, to convert the raw counts to physical units. The compass and tilt sensor data are converted by `Satcon` using coefficients and information in a *text definition file* (`*.tdf`), provided by Satlantic. The ASCII files produced by `Satcon` are given the file extension `*.dat`.

The Hydroscat-II log file data are converted to physical units using HOBI Labs' Hydrosoft software and the HOBI Labs calibration files and output to (`*.dat` ASCII) files. There are no valid time values associated with these files, except the time of file creation in the filename.

The CTD `*.log` files do not require preprocessing before they are concatenated and merged with the other instrument data. There is no time data associated with these files except for the file creation time in the log file name.

A Matlab processing script removes header lines from all the ASCII `*.dat` files then, where multiple files for one day exist, these are concatenated into a single file for each day and for each instrument. In order to have a single day file for all the instruments, the timeframe of the 4 m DATA-100 file is used as a standard for each of the other files. The number of rows in the final file, therefore, is always the same as the 4 m DATA-100 file. Two processes are required for integrating the other instrument files, one for the files that have their own time stamps already and one for those that do not. The latter relates to the CTD and Hydroscat-II files.

Where a time stamp is present for an instrument, integrating the data time frame for this instrument into the 4 m DATA-100 timeframe is performed by finding the closest time stamp in the 4 m DATA-100 file that is less than the time stamp for each line of the file of interest and within the same 1 min sampling period.

For the Hydroscat-II and CTD data, which are not time stamped, their integration into the 4 m DATA-100 time base is performed using the proportion of each 1 min 4 m DATA-100 sampling period to the entire day of 4 m DATA-100 data. The progressive proportions of each of these sampling periods for a day of data is then used to divide up the day of CTD and Hydroscat-II data to the same ratio. Once these files are divided into theoretical 1 min slots, the data lines within each slot are then distributed evenly across the true 1 min sampling period of the 4 m DATA-100.

For the seven radiometers (OCR-200 and OCI-200), a dark correction is performed by subtracting, from each radiometer data series, the mean data values collected between the hours of midnight and 0200 hours for each instrument. After processing, general radiometer health can be assessed for each day by monitoring these dark values. The dark values for each instrument are, therefore, saved to a file where they can be easily checked for changes. The buoy data after preprocessing is presented as large (approximately 13 MB) individual files containing all instrument data for a single day from midday to midnight.

7.7 IOPs from the Buoy Data

The processing of the fluorescence and IOP data collected on the buoy simply follows the procedures recommended by the instrument manufacturers, i.e., the Chelsea *User Guide for MINItracka II C* In-Situ *Fluorimeter HB 176* for phytoplankton fluorescence, the Wetlabs *C-Star Transmissometer User Guide* for the beam attenuation coefficient at 660 nm, and the HOBILabs *Hydroscat-II Spectral Backscattering Sensor User's Manual* (Revision F, October 25, 2004) for the backscattering coefficient. Concerning the latter, the recommendations of Mafione and Dana (1997) and Boss and Pegau (2001) are used to transform the measurement of the volume scattering function at 140° into the particle backscattering coefficient.

7.8 AOPs from Buoy Data

The apparent optical properties that are derived from the radiometry measurements collected by the buoy are providing the core of the satellite matchup data set.

7.8.1 Measurement Suite

The in-water optical measurements are made at two depths (nominally 4 and 9 m) and at seven wavelengths from 412–681 nm (Table 1). Three types of measurements are acquired: a) the upward irradiance, $E_u(z,\lambda)$; b) the downward irradiance, $E_d(z,\lambda)$, which is not used in the computation of the reflectance; and c) the upwelled (nadir) radiance, $L_u(z,\lambda)$. The above-water downward irradiance, $E_s(\lambda)$, is recorded on top of the buoy at approximately 4.5 m above the surface (at the same seven wavelengths).

7.8.2 Computed Parameters

The first step in the data processing scheme consists of a data reduction, which aims at producing one representative value for each of the 1 min sequences of acquisition. During these sequences, about 360 measurements are collected (acquisition rate of 6 Hz), which may include some

outliers and are usually noisy because of the fluctuations of the radiative field due to the wave-roughened air–sea interface. Taking the median of the 360 measurements has been found to be a simple and robust way of filtering the data.

From the two values of $E_u(z,\lambda)$, the upward irradiance at null depth $z = 0^-$ (immediately below the sea surface) is obtained as (omitting wavelength for brevity):

$$E_u(0^-) \;=\; E_u(4)\, e^{ZK_u}, \tag{8}$$

where Z is the measurement depth (not exactly 4 m when the buoy is lowered or when swell is going through the superstructure), K_u is the diffuse attenuation coefficient for the upward irradiance computed from the measurements of E_u collected at the two depths. The same extrapolation can be performed from the measurement at 9 m.

From the two values of $L_u(\lambda)$ at 4 and 9 m, the upwelling radiance at null depth is obtained as:

$$L_u(0^-) \;=\; L_u(4)\, e^{ZK_L}, \tag{9}$$

where Z is the measurement depth, and K_L is the diffuse attenuation coefficient for the upwelling radiance computed from the measurements of L_u collected at the two depths.

Before combining these values to the above-water reference measurement, E_s, in order to compute the reflectance, E_s is corrected for the buoy tilt. The correction is a function of the orientation of the two axes of the tilt measurement with respect to the solar azimuth angle, and computes the ratio of the diffuse (not affected by the tilt) to direct (affected) light for clear-sky conditions.

The computation of R, follows (6) and K_d follows (7), where the depth z can be from either measurement depths (nominally 4 and 9 m). This coefficient is also computed between these two measurement depths.

7.9 Sun Photometer Data

The first data set that comes from the processing of the sun photometer data includes the aerosol optical thickness at five wavelengths (Table 1). Numerous methods have been developed in the past years, which are dedicated to the retrieval of information about aerosol types, usually particle size distributions, refractive indices, or phase functions from measurements of sky radiances collected either in the principal plane, following almucantars, or in the solar aureole. Good examples of these activities are provided by Santer and Martiny (2001), Dubovik and King (2000), Dubovik et al. (2000), and Nakajima et al. (1983 and 1996).

A similar method has been developed, which is distinguished by using the degree of polarization, as measured at 870 nm by the sky photometer. Using this additional piece of information, in principle, decreases the ambiguities of the inversion process. In order to find the best candidate aerosol model that allows a reconstruction of the sky radiances distribution observed in the principal plane, the method either uses the trial-and-error principle or a more sophisticated inversion algorithm based on the use of a neural network. A radiative transfer code is used in these inversions, which is based on the successive orders of scattering method and uses the vector theory *Ordres Successifs Océan et Atmosphère*, (OSOA) code (Deuzé et al. 1989 and Chami et al. 2001).

In regards to the neural network approach, which has the advantage of allowing fast processing of time series and has the ability of properly dealing with measurement errors, the important step is the training of the neural network. This training has also been performed by using the OSOA radiative transfer code, and using aerosol models with varying indices of refraction and particle size distributions following either a Jünge model or a log-normal distribution with two modes (small and large particles). A realistic noise that accounts for instrumental errors is added to the synthetic data.

8. INITIAL RESULTS

In the following sections, sample results are provided for the three basic data collection opportunities: the ship campaigns, the buoy daily acquisitions, and the sun photometer data. The purposes of the presentations are to establish the extent of the sampling program, in terms of the type and quality of data products being produced, and to illustrate the site characteristics.

8.1 Data Collection Summary

The following three sections present a quantitative summary of the data collected from the ship, from the buoy, and at the coastal AERONET site.

8.1.1 Ship Data

Table 5 provides a list of monthly maintenance cruises until April 2006 (and continuing since then on a monthly basis), and indicates how many data collection events have been executed for each instrument category. Data collection is either in the form of a vertical profile of an appropriate portion of the water column (SPMR, CTD, and IOPs), individual temporal sequences based on a proper amount of time or number of samples (CIMEL and SIMBADA), or discrete samples of filtered seawater taken from a variety of depth levels (A_p, HPLC, and TSM).

8.1.2 Buoy Data

Table 6 indicates the number of buoy deployment days for the successive deployment sequences. The gap in 2001 is associated with the redesign effort of the original (version 1) buoy to correct some deficiencies noted in the first deployment (but note the continuation of the site characterization during this time period as shown in Table 5).

Table 5. A list of the monthly maintenance cruises from 2001–2005 (inclusive) and the types of measurements collected. The cruise identification (ID) number provides a sequential enumeration of the data collection sequence. All scheduled cruises are shown to establish the level of effort undertaken. If a cruise was cancelled (e.g., ID 27), perhaps because of bad weather or a scheduling conflict, the number of days is shown as zero and there are no data entires for this maintenance cycle. A checkmark indicates data were collected and a numerical value indicates how many discrete samples, profiles, or acquisition sequences were acquired.

Year	*Dates*	*ID*	*Days*	*SPMR*	*CTD*	*IOPs*	*CIMEL*	*SIMBADA*	*Ap*	*HPLC*	*TSM*
2001	22 Jul → 24 Jul	1	3	19				8		9	
	2 Sep → 4 Sep	2	3	21	6			20			
	2 Oct → 4 Oct	3	2	2						20	
	3 Nov → 5 Nov	4	1	14	3					2	
	2 Dec → 4 Dec	5	2	11				7		9	
	12 Dec → 14 Dec	6	0								
2002	21 Jan → 23 Jan	7	3	6	5					13	
	25 Feb → 27 Feb	8	0								
	22 Mar → 24 Mar	9	2	11	2			6		9	
	10 Apr → 12 Apr	10	0								
	20 May → 22 May	11	3	12	2					28	
	26 Jun → 28 Jun	12	4	24	10			11		31	
	20 Jul → 22 Jul	13	3	26	5	✓		10		31	
	2 Sep → 4 Sep	14	3	9	3	✓		7		20	
	5 Oct → 7 Oct	15	2	11	2	✓		3		23	
	26 Oct → 28 Oct	16	0								
	27 Nov → 29 Nov	17	2	14	4	✓				29	
	7 Dec → 9 Dec	18	0								
2003	7 Feb → 9 Feb	19	2	18	4	✓		5	21	47	
	17 Mar → 19 Mar	20	2	8	1	✓		4	20	27	
	5 Apr → 7 Apr	21	1	11	2	✓		12	20	20	
	27 May → 29 May	22	3	36	13	✓		30	14	50	
	27 Jun → 29 Jun	23	3	24	10	✓		25	28	47	
	13 Jul → 15 Jul	24	3	47	14	✓		26	57	87	
	29 Aug → 31 Aug	25	0								
	23 Sep → 25 Sep	26	3	10	9	✓		1	29	36	
	16 Oct → 19 Oct	27	0		1						
	5 Dec → 7 Dec	28	3	12	10	✓			32	48	
	16 Dec → 18 Dec	29	2	12	7				19	37	
2004	28 Jan → 1 Feb	30	5	20	13	✓		5	32	39	
	3 Mar → 7 Mar	31	3	15	9	✓		5	20	32	
	9 Apr → 12 Apr	32	4	11	10	✓			27	36	
	2 Jun → 4 Jun	33	4	30	12	✓			28	34	
	5 Jul → 7 Jul	34	3	11	10	✓			10	43	
	31 Jul → 17 Aug	35†	9	54	92	✓	105	180	247	279	
	15 Oct → 23 Oct	36	3	5	1	✓	6		4	14	
	21 Nov → 24 Nov	37	3	9	11	✓			12	49	
2005	31 Jan → 4 Feb	38	3	13	13	✓			11	43	
	23 Feb → 26 Feb	39	3	5	10	✓	8		14	28	
	25 Mar → 28 Mar	40	3	6	11	✓	5		26	38	
	15 Apr → 18 Apr	41	4	3	8	✓	9		27	36	
	26 May → 28 May	42	3	8	8	✓	12		21	21	
	27 Jun → 29 Jun	43	3	9	12	✓	12		25	33	

† Cruise 35 was the Advanced Optical Properties Experiment (AOPEX). It was carried out on a larger ship (R/V *Le Suroît*), and involved 17 scientists from LOV plus other European and American laboratories. Several additional parameters, such as the volume scattering function of particles, were collected, which are not indicated in this table.

Table 5 (cont.). A list of the monthly maintenance cruises for 2006 and the types of measurements collected.

Year	*Dates*			*ID*	*Days*	*SPMR*	*CTD*	*IOPs*	*CIMEL*	*SIMBADA*	*Ap*	*HPLC*	*TSM*
2005	27 Jul	→	29 Jul	44	3	7	11	✓	5		38	51	
	9 Sep	→	11 Sep	45	3		7	✓	2		19	21	
	8 Oct	→	11 Oct	46	4	7	9	✓	13		22	28	
	5 Nov	→	8 Nov	47	4	15	12	✓	4		30	53	9
	13 Dec	→	16 Dec	48	4	2	6	✓	2		9	10	3
2006	1 Feb	→	4 Feb	49	4	6	9	✓			23	28	4
	28 Feb	→	4 Mar	50	1		7	✓			11	11	
	14 Mar	→	17 Mar	51	4	14	10	✓			20	29	6
	3 Apr	→	6 Apr	52	3	14	10	✓	9		31	36	9

The main purpose of the redesign was to improve the percentage of time for which the stability requirements—in terms of inclination—were satisfied.

Table 6. A summary of the buoy data collected at the BOUSSOLE site.

Year	*Dates*			*ID*	*Days*
2000	20 Jul	→	20 Oct	1	90
2002	16 May	→	6 Jun	2	11
2003	6 Sep.	→	6 Dec	3	90
2004	4 Mar.	→	7 Apr	4	35
	11 May	→	23 Jul	5	72
	5 Aug.	→	31 Dec	6	149
2005	18 Feb	→	2 Jun	7	105
	17 Jun.	→	31 Dec	8	197
2006	1 Jan	→	10 Jun	8	161
	11 Jun.	→	To Date	9	

8.1.3 Sun Photometer Data

Table 7 presents how many days of data collection have been successfully completed at the sun photometer site.

Table 7. A summary of the sun photometer data collected at the *Cap Ferrat* coastal site.

Year	*Dates*			*ID*	*Days*
2002	3 Jul	→	31 Dec	1	181
2003	1 Jan	→	15 Apr	1†	105
2004	6 Jan	→	10 Nov	2	309
2005	16 Feb	→	5 Oct	3	231
	10 Feb	→	29 Mar	4	47
2006	26 May	→	To Date	5	

† The completion of the first deployment sequence.

8.2 Physical Conditions

Figure 13 is a time series of the potential temperature over the upper 200 m of the water column spanning the time period from July 2001 to January 2006. The well-known winter mixing and spring stratification clearly appear, as well as an increase of the summer surface temperature from year to year. The summer of 2003 was one of the warmest recorded over the last several decades in northern Europe, and the signature of this unusual climate is seen here in the temperature record.

Another noteable feature in Fig. 13 is seen in the winter of 2005, when the temperature did not reach the usual 12.9°C minimum, which is in principle a recurrent characteristic of the BOUSSOLE site, because of the occurrence of deep mixing during winter. The latter is the mechanism for the formation of the deep waters in the western Mediterranean basin. The cooling of the surface waters started much earlier than usual in the fall of 2005—as early as mid-December—instead of mid-January or February as in most other years.

8.3 Phytoplankton Pigments

Pigment samples for HPLC analysis have been collected at about 12 depths between the surface and 200 m at the BOUSSOLE site since July 2001. Surface samples at 5 and 10 m depths were collected in triplicate. During certain surveys only surface samples were taken. In the following section, results from these analyses from July 2001 to December 2005 are briefly described.

8.3.1 TChl *a* Seasonal Evolution

During the winter and the start of the spring bloom, moderate to high values for $\left[\text{TChl}\,a\right]$ have been observed, particularly for the month of February, when maximum values at the surface reached 1.34 in 2002 and 2.44 $\text{mg}\,\text{m}^{-3}$ in 2003 (Fig. 14). In February 2002, the water column appeared to have undergone strong vertical mixing just before the start of the survey, with $\left[\text{TChl}\,a\right]$ values averaging 0.845 $\text{mg}\,\text{m}^{-3}$ (±5%) down to 130 m.

March and April are characterized by the spring bloom, which takes place in the near-surface waters, with $\left[\text{TChl}\,a\right]$ values reaching approximately 5 $\text{mg}\,\text{m}^{-3}$. In March 2003, a deep chlorophyll maximum (DCM) already began to form at a depth of 50 m. During summertime, surface

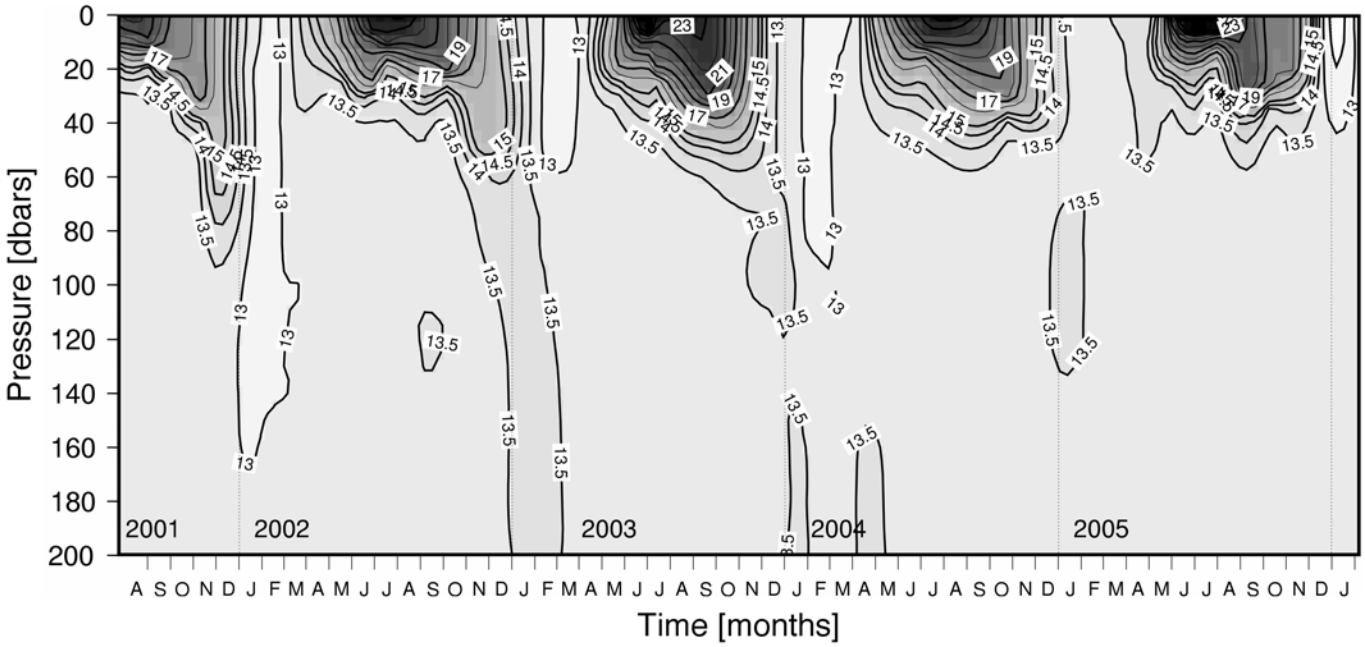

Fig. 13. A time series (July 2001 to June 2005) at the BOUSSOLE site of the potential temperature over the 0–200 m depth range (lighter to darker grays are associated with lower to higher temperatures, respectively).

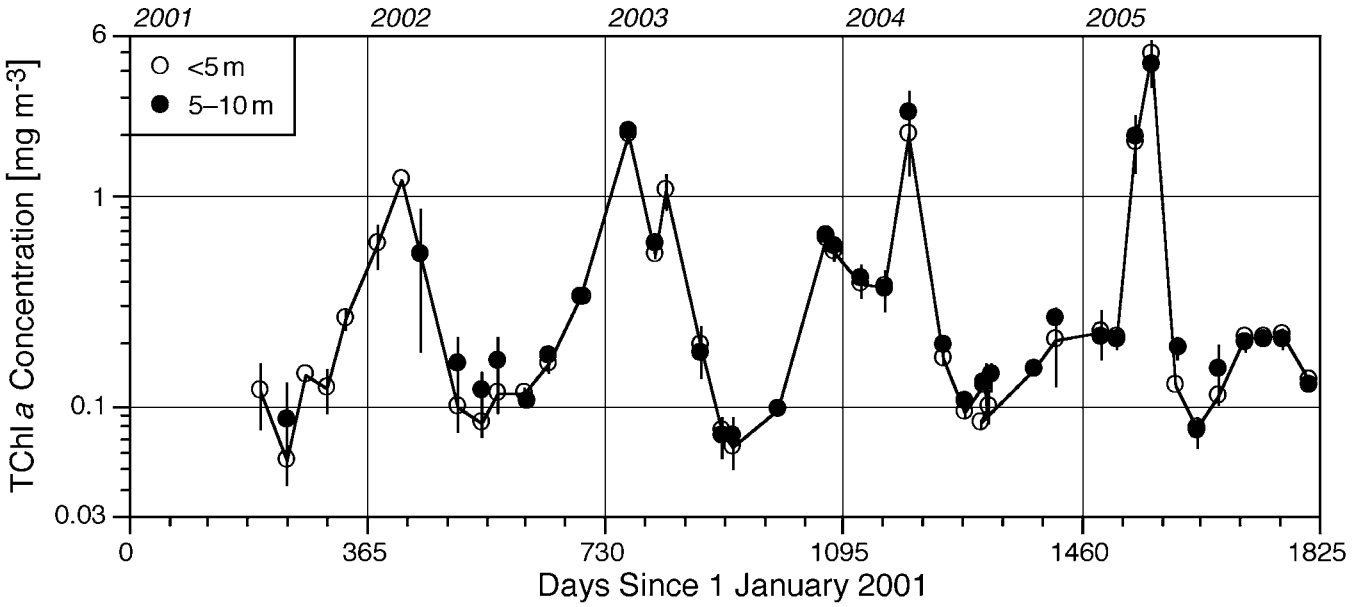

Fig. 14. The variations in the determination of the total chlorophyll *a* concentration between July 2001 and June 2005 at the BOUSSOLE site. Two sampling depths are depicted: depths less than 5 m are represented by the open circles, and depths greater than 5 m and less than 10 m are given by the solid circles. Each point is the average of all the measurements taken during a single cruise to the site. The vertical bars represent one standard deviation with respect to the average for each cruise.

$[\mathrm{TChl}\,a]$ concentrations remain low (0.1–0.2 mg m^{-3} and as low as 0.05 mg m^{-3} in the summer of 2001). Figure 15, however, demonstrates that this trend is not reflected in the deeper samples (below 10 m) where important development of phytoplankton takes place during the oligotrophic conditions of this Mediterranean site. The thickness of the DCM at 50 m tends to decrease towards the end of the summer period.

Autumn marks the transition between stratified summer conditions and winter turbulence (mixing) of the water column, with the progressive increase of surface $[\mathrm{TChl}\,a]$ values.

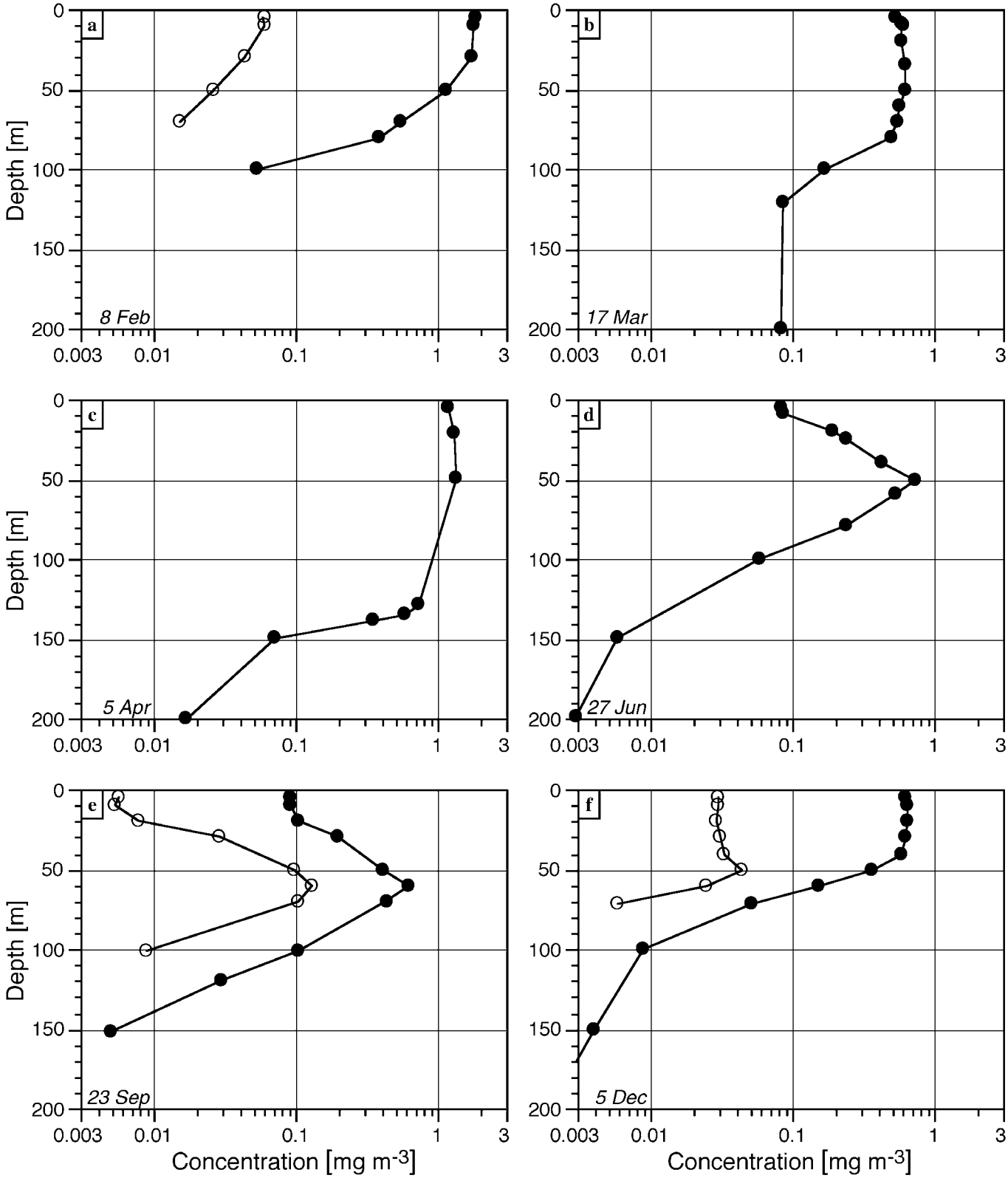

Fig. 15. TChl *a* (solid circles) and divinyl Chl *a* (open circles) over the 0–200 m depth range for the following days in 2003: **a)** 8 February, **b)** 17 March, **c)** 5 April, **d)** 27 June, **e)** 23 September, and **f)** 5 December.

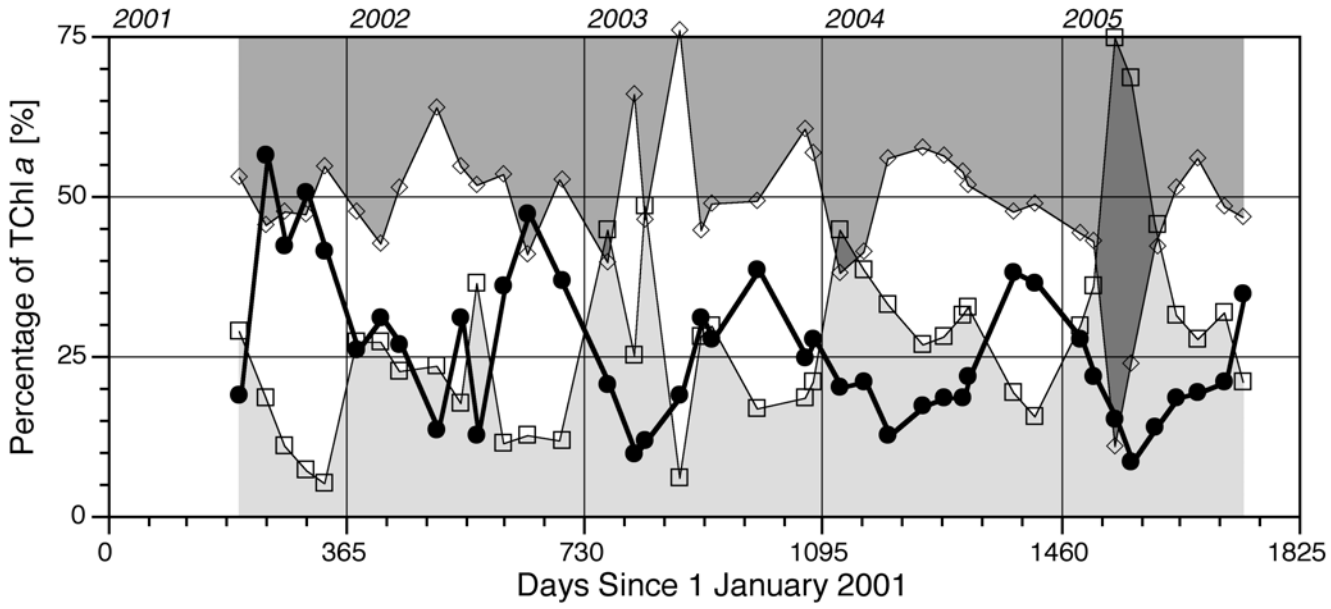

Fig. 16. A time series of average abundances of pico- (circles), nano- (diamonds), and micro- (squares) phytoplankton for surface samples (less than 20 m) between July 2001 and October 2005. Each point is the average over all measurements taken during a cruise. The gray shading is arbitrarily assigned to enhance the interpretation of the time series. The light and middle gray portions show the dominant separation of the community composition (in terms of contribution to the TChl *a* concentration) into a smaller percentage of microplankton and a larger percentage of nanoplankton, respectively. The exceptions are denoted by the occasional reversals highlighted in the darkest gray. The seasonal contributions of the picoplankton are indicated by the bold line.

8.3.2 Changes in Community Structure

Six carotenoids and total chlorophyll *b* were used to partition the phytoplankton into three size classes based on the unique aspects of the pigments used to establish the classification scheme. The fractions of the Chl *a* concentration associated with each of the pico-, nano-, and microplankton classes (f_p, f_n, and f_m, respectively) are derived using the following relationships (Uitz et al. 2006):

$$f_p = \frac{0.86[\text{Zea}] + 1.01[\text{TChl}\,b]}{[\text{DP}]}, \quad (10)$$

$$f_n = \frac{1.27[\text{Hex}] + 0.35[\text{But}] + 0.6[\text{Allo}]}{[\text{DP}]}, \quad (11)$$

and

$$f_m = \frac{1.41[\text{Fuco}] + 1.41[\text{Peri}]}{[\text{DP}]}, \quad (12)$$

where the diagnostic pigment, DP, is simply the sum of the seven pigment concentrations used to distinguish the three size classes.

Figure 16 presents the variations of these three classes for near-surface (between 0–10 m) waters between the middle of 2001 and the end of 2005. Generally, for surface waters, microphytoplankton (characterized by diatoms and dinoflagellates) and nanophytoplankton (characterized by prymnesiophytes and crysophytes) tend to vary in opposition with picophytoplankton (characterized by cyanobacteria at this site). The first are not a dominant class over the studied period, with minimum values in autumn. Nevertheless, at depth, microphytoplankton can reach important proportions relative to the other two classes, particularly in spring. Nanophytoplankton is a dominant class in surface waters over most of the year, except during the autumn when picophytoplankton tend to take over. The DCM, however, is dominated by nanophytoplankton over the whole summer–autumn time period.

The presence of divinyl Chl *a*, which is an indicator of prochlorophytes, has generally been observed during autumn at the DCM and even in surface waters during winter convection. In regards to the presence and concentrations of Chl *a* degradation products (e.g., chlorophyllide *a* and phaeophorbide *a*), they are most often below the detection limits of the HPLC method.

8.4 AOPs from Ship Operations

Figure 17 panels a, b, and c show the July 2001 to August 2004 time series of the reflectance ratio $R(\lambda)/R(560)$, for λ=443, 490, and 510 nm, respectively. Figure 18 shows, for the same time period, the diffuse attenuation coefficients of the upper layers for the wavelengths 412, 490,

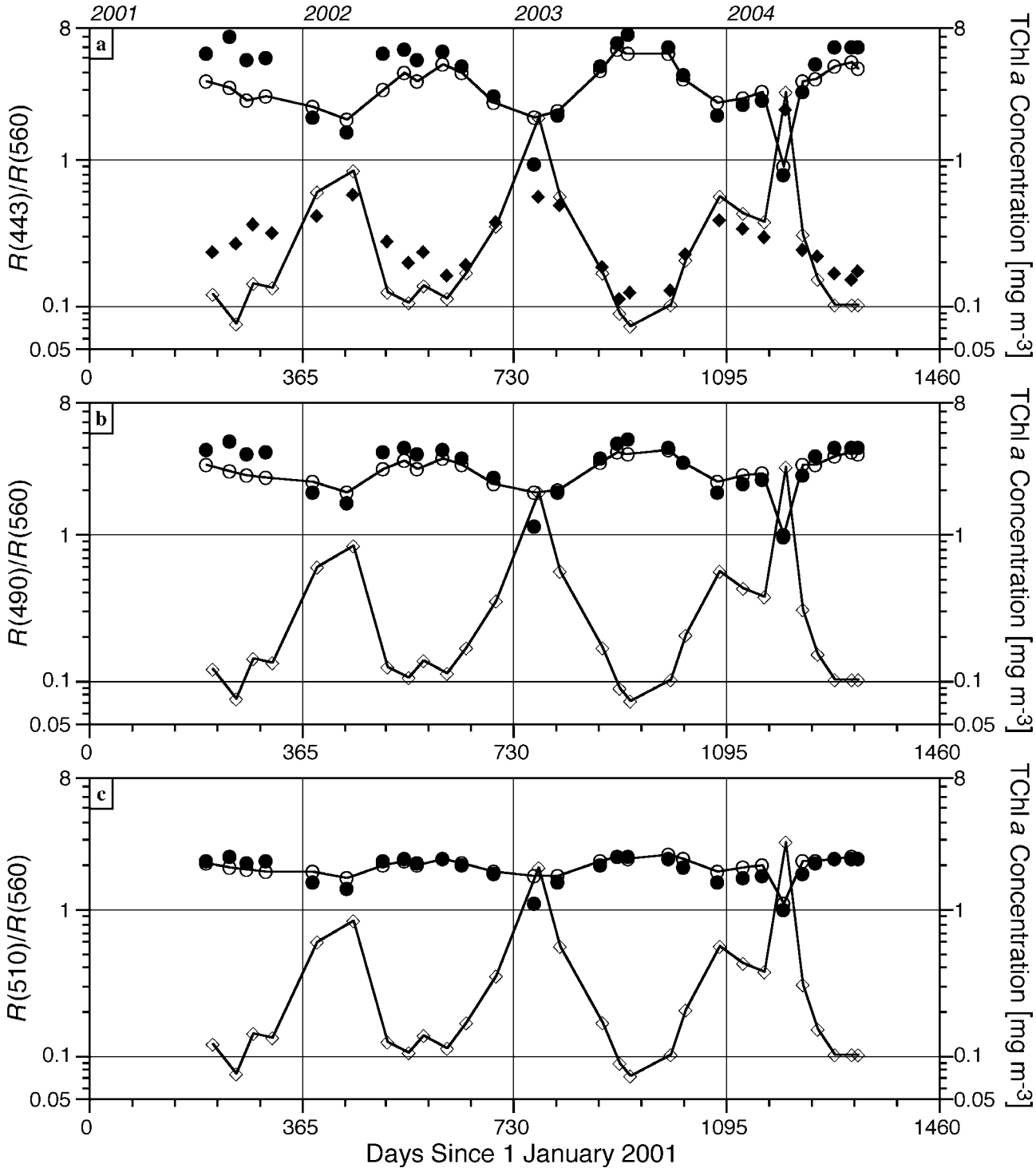

Fig. 17. A times series, from July 2001 to August 2004, showing three reflectance ratios: **a)** $R(443)/R(560)$, **b)** $R(490)/R(560)$, and **c)** $R(510)/R(560)$. The open circles are the average of the *in situ* data (several points per cruises) over each cruise. The open diamonds are for the (HPLC) $\left[\mathrm{TChl}\,a\right]$ values, the solid circles are for the reflectance ratio as computed through a model that is based on the *in situ* $\left[\mathrm{TChl}\,a\right]$ values (Morel and Maritorena 2001), and the solid diamonds are the $\left[\mathrm{TChl}\,a\right]$ values that would be derived through an ocean color algorithm using the *in situ* reflectances ratio.

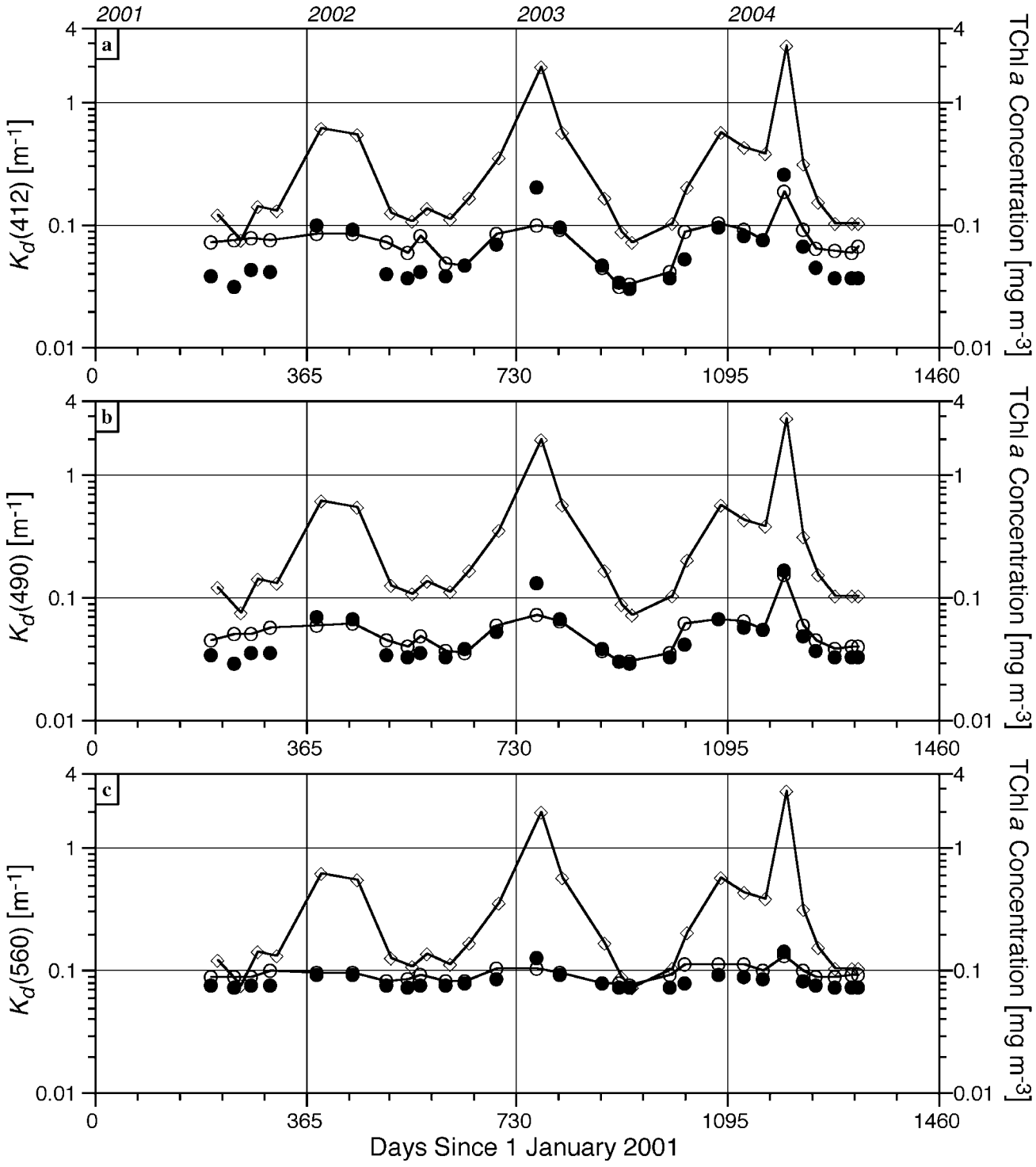

Fig. 18. A times series, from July 2001 to August 2004, showing three diffuse attenuation coefficients: **a)** $K_d(412)$, **b)** $K_d(490)$, and **c)** $K_d(560)$. The open circles are the average of the *in situ* data (several points per cruises) over each cruise. The open diamonds are for the (HPLC) $\left[\text{TChl}\,a\right]$ values, and the solid circles are for the K_d values as computed through a model that is based on the *in situ* $\left[\text{TChl}\,a\right]$ values (Morel and Maritorena 2001).

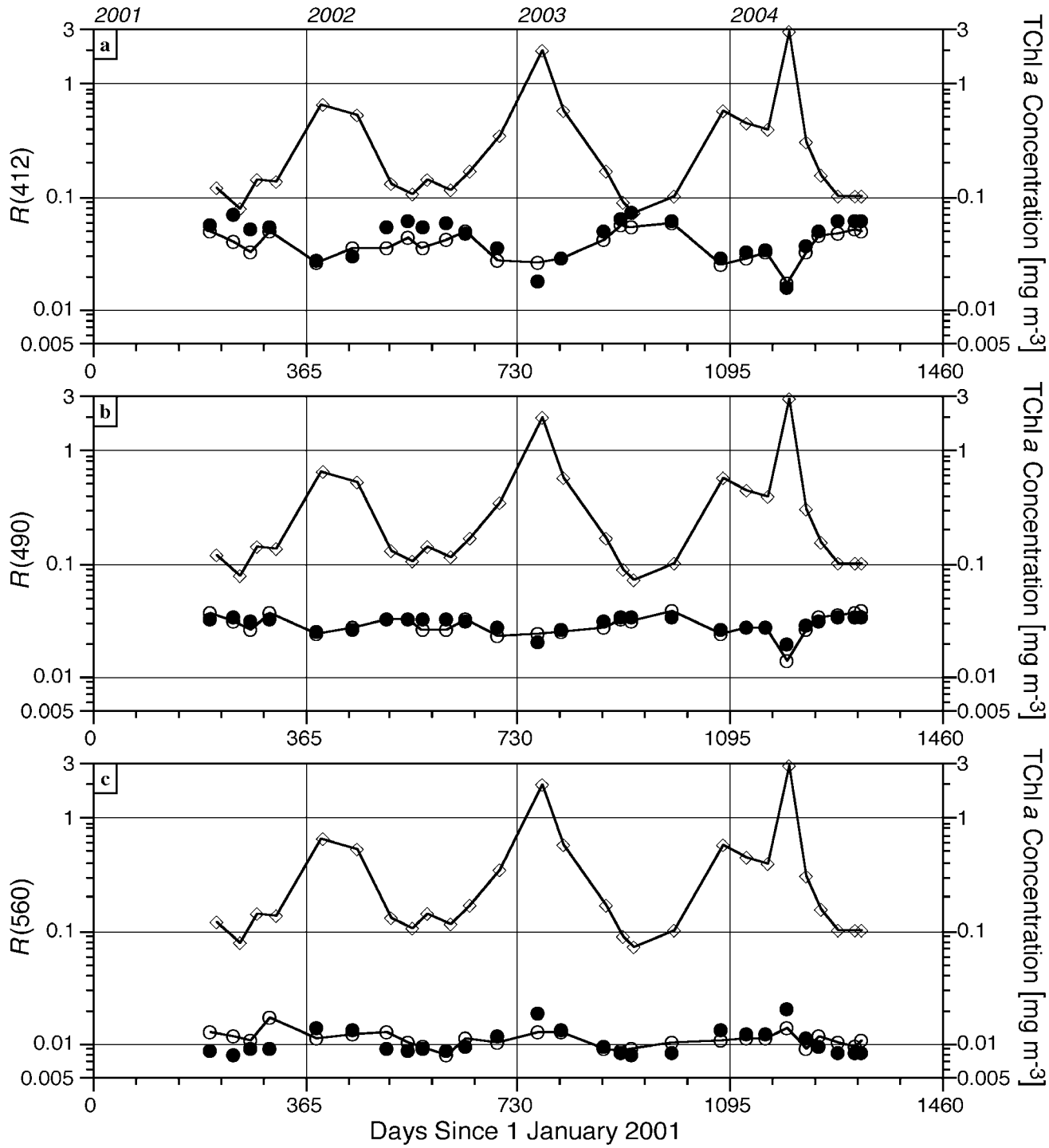

Fig. 19. A times series, from July 2001 to August 2004, showing three irradiance reflectances: **a)** $R(412)$, **b)** $R(490)$, and **c)** $R(560)$. The open circles are the average of the *in situ* data (several points per cruises) over each cruise. The open diamonds are for the (HPLC) $\left[\mathrm{TChl}\,a\right]$ values, and the solid circles are for the R values as computed through a model that is based on the *in situ* $\left[\mathrm{TChl}\,a\right]$ values (Morel and Maritorena 2001).

and 560 nm. Finally, Figure 19 shows the reflectances, $R = E_u(0^-)/E_d(0^-)$, for the same wavelengths. For all of these figures, the open circles are for the *in situ* data, the open diamonds are for the total chlorophyll *a* concentration determined from HPLC analysis, the solid circles are for the AOPs (either R, the ratio of R at two wavelengths, or K_d) as computed through a model that uses the *in situ* Chl *a* concentration as the input variable, and the solid diamonds are the Chl *a* concentration that would be derived through satellite algorithms using the *in situ* reflectance ratios.

The difference between the open and solid circles, therefore, represents the *anomaly* of the measured AOPs as compared to what is predicted by standard (global) bio-optical models, considering the *in situ* Chl *a* concentration. Similarly, the difference between the open and solid diamonds represents the uncertainty in the Chl *a* concentration that is obtained when satellite algorithms, which were derived from global data sets and are based on average global relationships between the reflectance ratios and the Chl *a* concentration, are applied to waters with *anomalous* optical properties.

One striking feature is the large anomaly of the blue-to-green ratio in the summer of 2001, with lower than expected blue-green ratios, as already identified and quantified in Claustre et al. (2002) for the 1999 *Productivité des Systèmes Océaniques Pélagiques* (PROSOPE†) cruise. The reason for the anomaly was attributed to the presence of desert dust particles in the water, which have an enhanced absorption in the blue and an enhanced scattering in the green parts of the spectrum (Claustre et al. 2002). This anomaly is, however, less important during the summer of 2002, it nearly vanishes during the summer of 2003, and appears again in the summer of 2004. The transient character of the anomaly has yet to be confirmed and explained.

Examination of the relationships for the diffuse attenuation coefficients, $K_d(\lambda)$, in Fig. 18 reveals that their values in the summer of 2001 are largely above the modeled values across the entire spectrum, at least from 412–560 nm, and that this difference is disappearing in summer of 2003. Because K_d is largely determined by the absorption properties of the medium, these observations mean that an excess absorption exists at all wavelengths in the July to September period in 2001.

The same feature does not appear in the reflectances (Fig. 19), which are lower than the modeled values in the blue, again during the summer of 2001, yet greater than the modeled values in the green. Because R is, to the first order, proportional to backscattering and inversely proportional to absorption, these observations confirm the presence of an excess of backscattering in the green part of the spectrum. Again, the transient nature of this anomaly remains to be confirmed and explained.

Another anomaly is seen in February 2003 with larger-than-expected blue-green ratios, which is in opposition to the summer anomaly. During the February 2003 cruise, the Chl *a* concentration was as large as $2\,\mathrm{mg\,m^{-3}}$. The reason for this behavior might be in the low scattering coefficients that are typical of a *fresh* phytoplankton bloom, where the proportion of large healthy cells characterized by a low backscattering efficiency is high, and the contribution of small detritus particles is low.

Figure 20 shows the seasonal and interannual evolution of K_d for wavelengths 412, 490, and 560 nm. The time series was established from three years of measurements carried out during the (approximately) monthly maintenance cruises. This parameter is largely determined by the absorption coefficient, and it is thus a good indicator of the concentration of phytoplankton and associated colored dissolved substances. The seasonal cycle appears very clearly, in particular in 2003 and 2004:

- It starts with an intense mixing of water in winter (maximum in February) resulting in almost homogeneous water properties and weak K_d values;
- It continues with the start of the spring bloom in the March–April time period; and
- It then evolves gradually to oligotrophic conditions (with a minimum in Chl *a* concentrations around September), which is characterized by a peak in attenuation at about 50 m depth (coincident with the DCM).

For Chl *a* concentrations lower than $0.1\,\mathrm{mg\,m^{-3}}$ at the surface during the latter oligotrophic period, the global statistical relationships (Morel and Berthon 1989) predict a DCM at approximately 100 m. Its development at a lesser depth at the BOUSSOLE site is due to the fact that the site is in the center of a cyclonic circulation, which is dynamically represented as a dome-like structure that is maintained by significant vertical advection (the vertical ascent of deeper water transports the DCM to a shallower depth).

The interannual variability observed here for K_d seems directly related to the changes of the physical framework. Indeed, the depth of the DCM seems to increase by 2001 to 2004, at the same time as the winter mixing seems to intensify and the spring bloom being more intense. The oligotrophic layer of water characterized by low values of K_d in summer is deeper in 2003 than in 2001 and 2002. An intense mixing in winter on the one hand brings more nutrients to the surface, supporting a stronger bloom, and, on the other hand, more efficiently eliminates the colored dissolved substances accumulated at the surface during summer. This phenomenon has already been shown for dissolved organic carbon (Copin-Montegut and Avril 1993 and Avril 2002) and could explain the changes observed

† Translated as productivity of pelagic oceanic systems. Detailed information about the PROSOPE cruise is available from the `http//www.obs-vlfr.fr` Web site.

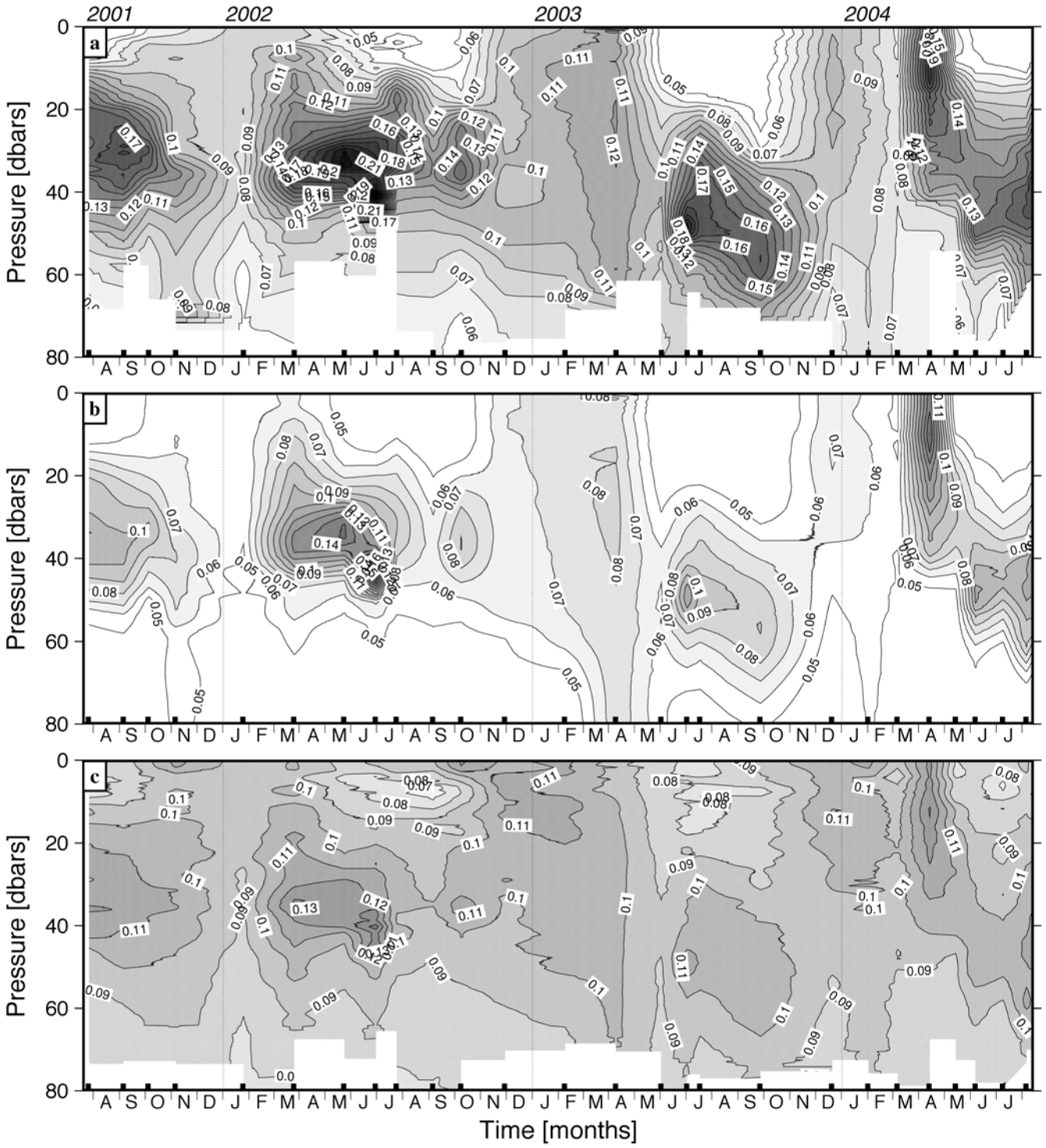

Fig. 20. A time series of the vertical distribution of the diffuse attenuation coefficient (K_d) derived from SPMR E_d vertical profiles at **a)** 412 nm, **b)** 490 nm, and **c)** 560 nm. The small black bars protruding upwards from the x-axis and into the contour maps denote the time of the ship sampling. The units for K_d are per meter.

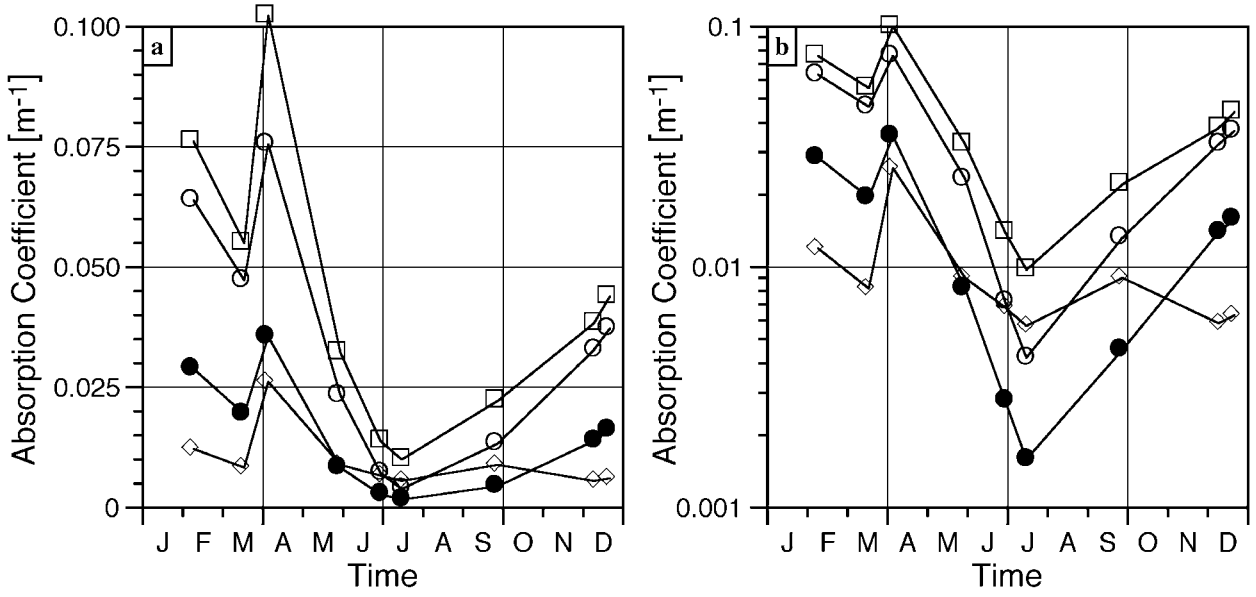

Fig. 21. A time series of data collected in 2003 of the absorption coefficients at 440 nm for total particles (open squares), phytoplankton (open circles) and detritus (open diamonds). The absorption coefficient of phytoplankton at 676 nm is also depicted (solid circles). Two different scales for the y-axis are shown: **a)** a linear scale, and **b)** a logarithmic scale in order to provide a better discrimination of the low values during the summer months.

in the so-called anomalies of the marine reflectance as discussed above.

The interannual variability of the spring bloom, however, is somewhat distorted by an insufficient sampling in spring 2002 and 2003 (bad weather). Consequently, it will probably be necessary to rebuild part of the record by using the vertical profiles of the pigments and the values derived from the satellites, coupled with the relationships between Chl a and K_d that will be established from the existing data.

8.5 IOPs from Ship Operations

An annual cycle of the particulate absorption coefficients at 440 nm is presented in Fig. 21, where the different curves are for total particles (a_p, directly measured on filtered samples), and both the phytoplankton and detrital particles (a_ϕ and a_d, respectively). The latter are derived through a numerical decomposition scheme (Bricaud and Stramski 1990) as presented in Sect. 7.2. An important feature here is the high contribution of the absorption by detrital particles, at least 50% of the total particulate absorption, from about the end of June to the beginning of September.

Figure 22 shows examples of the absorption spectra by particles, either for the total particles or for the phytoplankton or detritus only. The dominant role of phytoplankton in the absorption budget during the spring bloom clearly appears, as well as the progressive increase of that part of absorption that is due to detritus in summer. The exact cause of the background absorption in the ultraviolet (UV) that clearly appears when absorption decreases at other wavelengths (see the summer spectrum) remains to be identified.

Figure 23 presents examples of the total attenuation, scattering, and absorption coefficients for the surface (0–10 m) layer (from the AC-9+). Note the clear identification of the absorption features on the scattering spectrum, and the change in its slope from spring to summer (the increasing slope in summer corresponds to the large contribution of detritus as compared to phytoplankton alone).

Selected observations of the total scattering coefficient at 550 nm, as determined from AC-9+ measurements, are displayed in Fig. 24 as a function of the TChl a concentration, along with the values derived from the Loisel and Morel (1998) relationship. What can be noticed is that the organization of the *in situ* data with respect to the model is providing some clues for their interpretation. For instance, the three lowest values, which correspond to summer, are above the model line; this may be linked to the increasing proportion of detritus during this season. In contrast, the largest value, which corresponds to the spring bloom, is largely below the model line; this may indicate the dominance of large healthy cells with low scattering efficiencies. The other points in the graph, which are closer to the model line, correspond to autumn. This example and the tentative interpretation of the data distribution are provided to illustrate the type of investigations that will be performed with the full data set that is being collected for the BOUSSOLE activity.

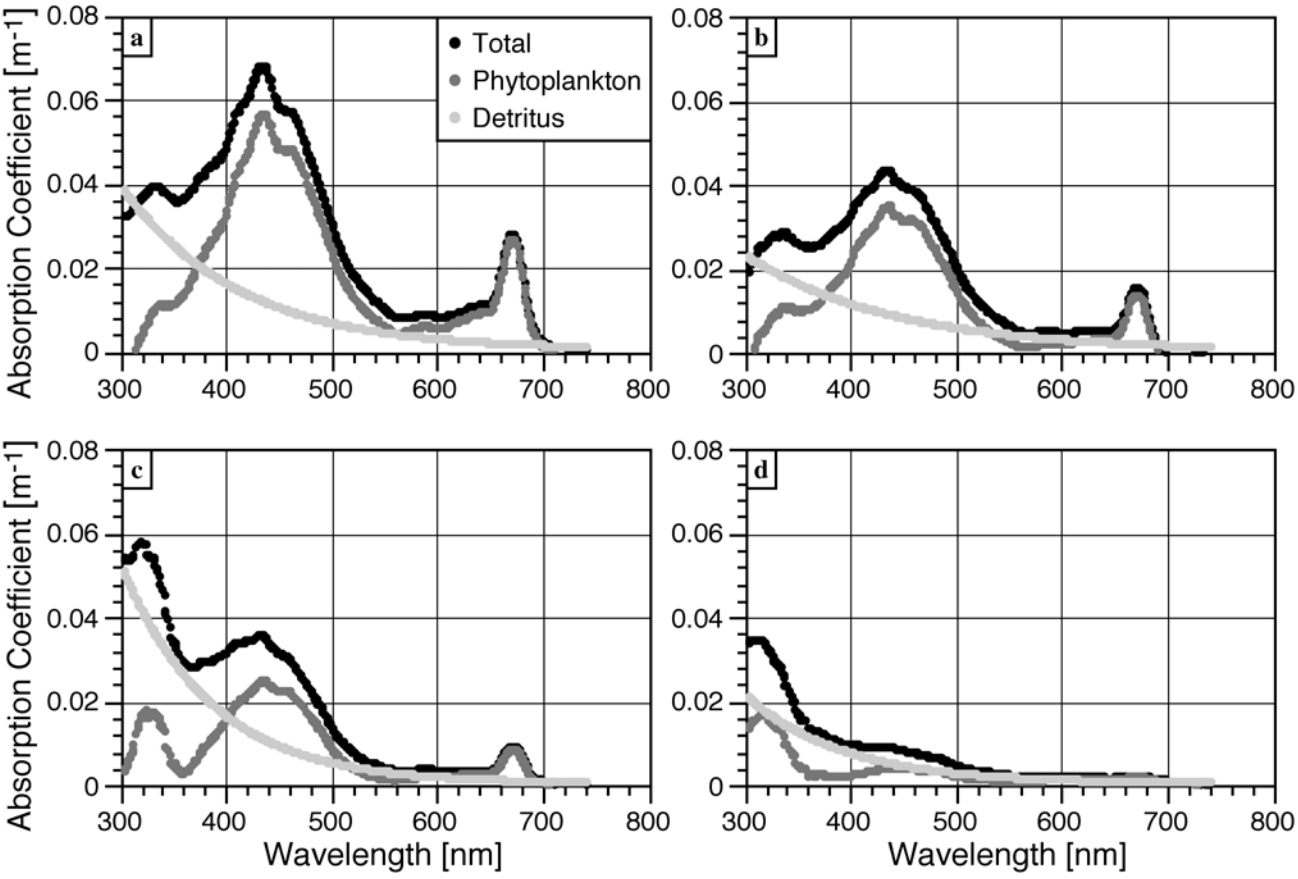

Fig. 22. Spectra of the absorption coefficient of particles at 5 m for 2003: **a)** 8 February, **b)** 17 March, **c)** 29 May, and **d)** 13 July. The $\left[\mathrm{TChl}\,a\right]$ values are 1.85, 0.52, 0.15, and 0.05 mg m^{-3}, respectively.

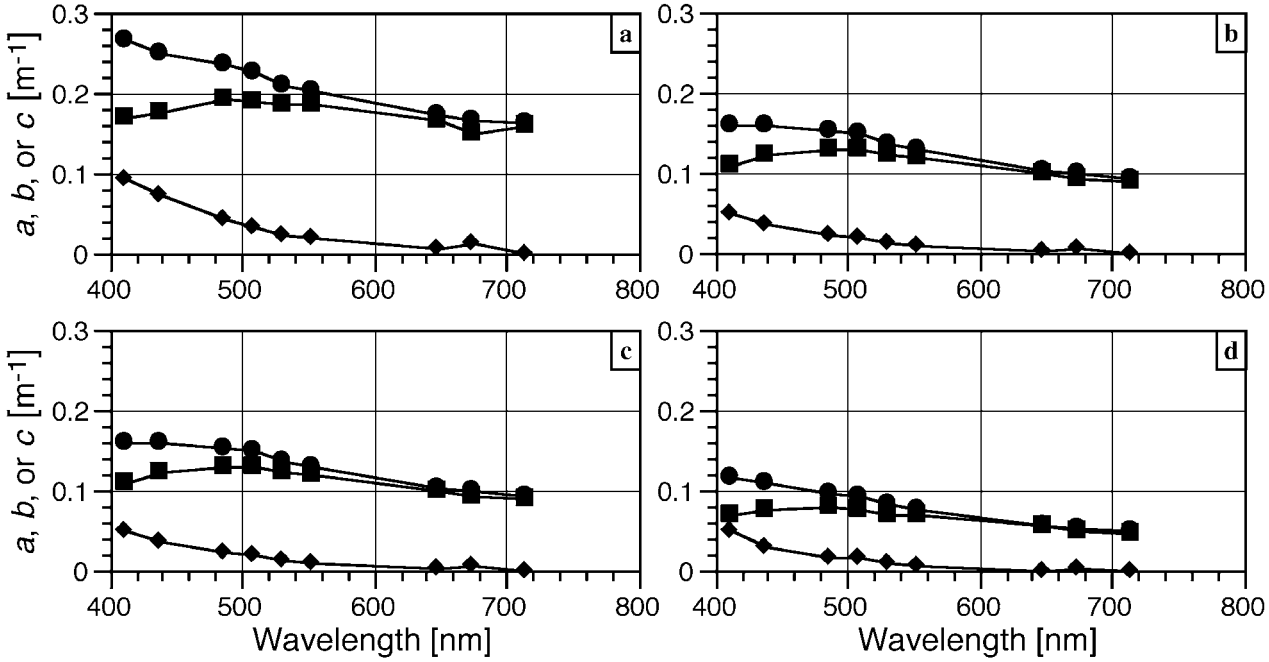

Fig. 23. AC-9+ spectra of the total attenuation (circles), absorption (diamonds), and scattering (squares) coefficients for the near-surface layer (10 m) for four different time periods: **a)** 7 February 2003, **b)** 5 April 2003, **c)** 27 May 2003, and **d)** 31 July 2004.

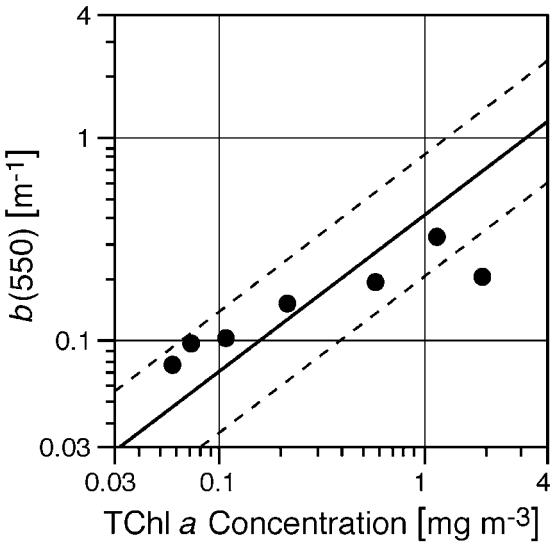

Fig. 24. The total scattering coefficient at 550 nm as a function of the TChl *a* concentration. Solid circles correspond to *in situ* values (AC-9+), and the solid and dashed lines are $b(550)$ values computed from Loisel and Morel (1998) and a factor of two around the modeled values, respectively.

8.6 AOPs from Buoy Data

Before discussing the time series of the reflectances derived from the buoy data, a comparison is performed with the reflectances derived from the SPMR. Although a limited data set has been used here (not the full time series of buoy and SPMR data), the comparison (Fig. 25) shows a good agreement, with a small bias of approximately 2%.

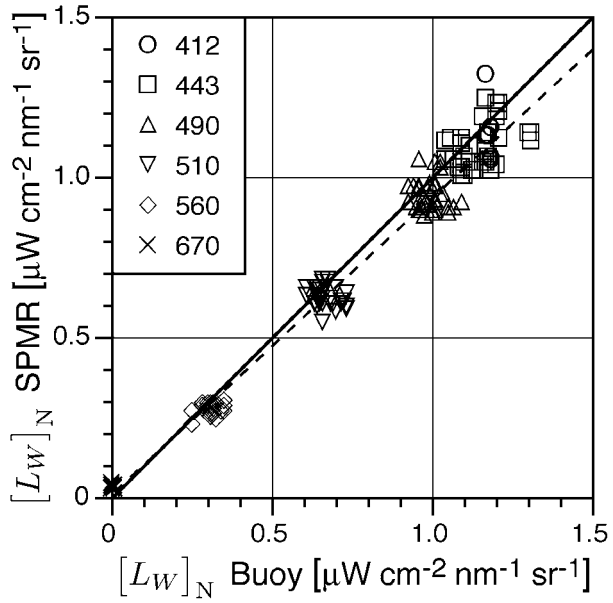

Fig. 25. A comparison of normalized water-leaving radiances from the SPMR and buoy for the wavelengths indicated.

A least squares fit to all the Fig. 25 data (dashed line) has a slope of 0.93, a y-intercept of 0.01, and a coefficient of determination of $r^2 = 0.98$. Further work is needed to unambiguously attribute this bias to either the SPMR or the buoy.

Figure 26 presents a one-month time series of the reflectance at 443 nm and 560 nm, corresponding to the development of the spring bloom in 2004 (March 4 to April 7). The TChl *a* concentration ranges from about 0.2 mg m^{-3} at the beginning of the sequence to about 3.5 mg m^{-3} at the end, and the reflectance in the blue and green domains change accordingly. The reflectance goes from about 3% to less than 1% at 443 nm, and from about 1–2% at 560 nm. Large daily changes also occur, which result from the combined effects of changes in the water optical properties and the daily solar cycle. The latter can be easily removed through an appropriate normalization (Morel and Gentili 1991).

Figure 27 shows a longer time series of the reflectance in the blue (443 nm), which actually corresponds to all the data collected by the buoy in 2005. The full range of variability spans about 1–5% in reflectance. The depression caused by the spring phytoplankton bloom is maximum around mid-April, and the maximum of reflectance occurs at the end of July, when the TChl *a* concentration is close to its annual minimum (about 0.1 mg m^{-3}). Note that the reflectance significantly decreases during August, whereas the TChl *a* concentration does not increase and remains close to 0.1 mg m^{-3}. This phenomenon is another illustration of what has been already discussed in Sect. 8.4 (*anomalies* in the blue-to-green ratio).

8.7 IOPs from Buoy Data

Figure 28 displays the record of the phytoplankton fluorescence (dashed curve) and of the beam attenuation coefficient at 660 nm (solid curve), during a one-month period corresponding to the development of the spring bloom in 2004 (March 4 to April 7; same as in Fig. 26). The TChl *a* concentration is from about 0.2 mg m^{-3} at the beginning of the sequence to about 3.5 mg m^{-3} at the end.

The fluorescence varies in a complex manner. For instance, the depression of the fluorescence signal around noon, which depends on the actual irradiance at the sea surface, is well pronounced. It may actually lead to variations within a day that are larger than the day-to-day change of the average fluorescence. A practical consequence is that the signal during the day cannot be used as a proxy of the Chl *a* concentration. Night values are better adapted for that purpose, and indeed they seem to be well correlated to the evolution of the Chl *a* concentration (not shown here).

The beam attenuation coefficient at 660 nm is a proxy of the particle load, and varies closely with the fluorescence values recorded at night. The bloom produces a ten-fold increase in $c(660)$, from 0.2–2.0 m^{-1}, mostly occurring between days 90 and 95. Daily changes are also

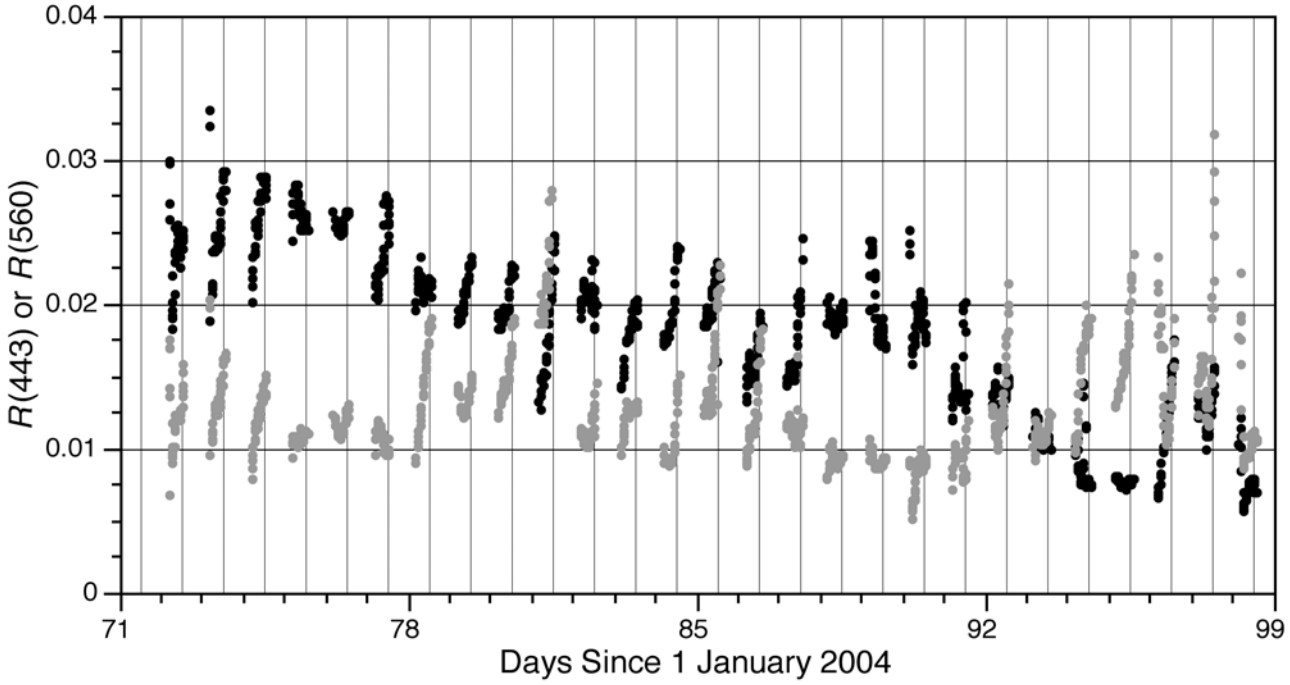

Fig. 26. An approximately 4-week buoy time series of $R(443)$ and $R(560)$, indicated as black and gray circles, respectively. The thin vertical lines indicate solar noon.

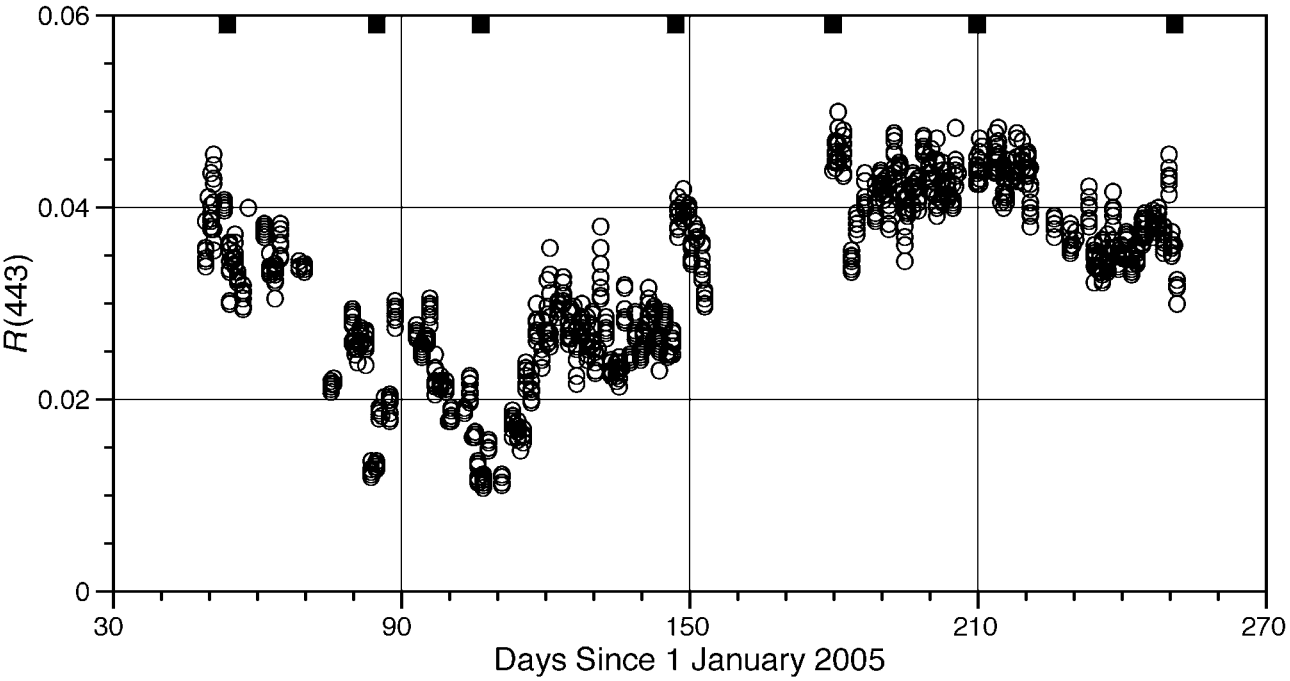

Fig. 27. A time series of all the reflectance data in the blue part of the spectrum (443 nm) collected by the buoy around noontime in 2005. The black squares at the top of the plot denote the occurrences of the monthly maintenance cruises.

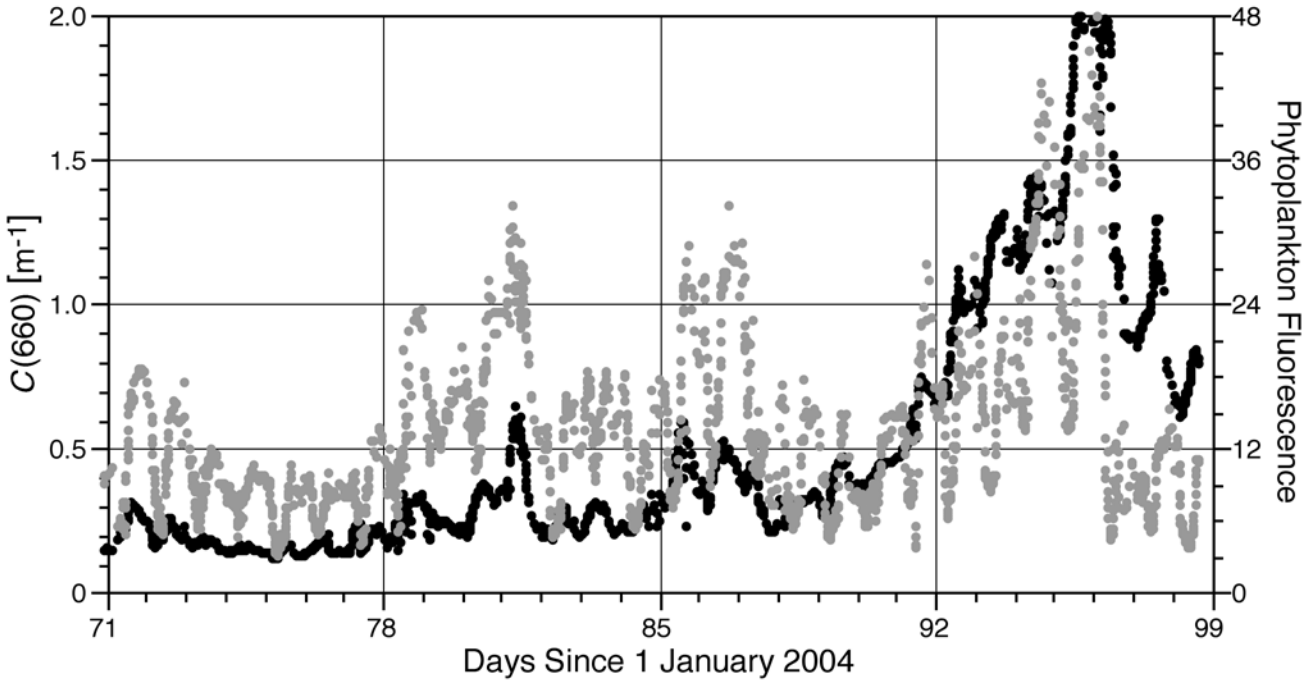

Fig. 28. An approximately 4-week buoy time series of the beam attenuation coefficient at 660 nm (black circles) and the phytoplankton fluorescence (gray circles). The latter is presented in relative units.

clearly shown, with a great variety of shapes, however, and sometimes with very fast increases (day 95 for instance) or dramatic declines (day 96). The maximum is usually occurring around noon or a few hours after noon. Inherently to Eulerian measurements at a fixed moored station, these changes are the result of the local phytoplankton growth and of lateral advection of water masses.

8.8 Sun Photometer Data

Figure 29 illustrates the overall data set that has been collected up to now at the *Cap Ferrat* sun photometer site. What is shown is the aerosol optical thickness as derived by the AERONET project through their standard procedures. The monthly AOT averages are usually minimum in January or February, and several relative maxima occur in spring (March or April), summer (usually July), and fall (October–November). The corresponding monthly averages of the Angström exponent (not shown) are always above $1.0\,\mathrm{m}^{-1}$, which indicates the persistence of small particles throughout the year.

The ability of the inversion method, which was developed as part of the BOUSSOLE project and uses ground-based data to get aerosol optical properties (Sect. 7.7), is demonstrated using days corresponding to MERIS overpasses. The results are presented in Fig. 30 for sequences of principal planes corresponding to high solar zenith angles (typically above 70°) to better cover the backscattering region of measurements and to include the scattering angle of 150°. Table 8 presents the values of the retrieved refractive index for these sequences. The agreement between measurements and predictions is good, especially in the backward direction for sky radiances. The degree of polarization is also accurately retrieved, especially at 90°, which is of interest for classifying particle types.

These examples demonstrate it is possible to obtain some information on the refractive indices of aerosols by using the inversion method and, thus, to get the aerosol phase function. Such information can be used to predict the angular distribution of the radiance and the degree of polarization, thus, it is likely that ground-based photometer measurements can be used for the vicarious calibration of satellite ocean color sensors (Sect. 10).

9. SATELLITE VALIDATION

Match-up analyses of the water-leaving radiances, as well as for the Chl *a* concentrations, have been performed for the MERIS, SeaWiFS, and MODIS-A data products. The analyses all follow the same procedure, wherein a 5×5 pixel box is extracted from the level-2 product (see below), and directly compared to the same quantity as derived from the *in situ* data (ship or buoy). For the SeaWiFS and MODIS-A sensors, the criteria used for a given comparison point to be excluded in the final analysis are described by Bailey et al. (2000). They are essentially the same for MERIS data, except the flags are not identical.

The combination of data availability, orbit characteristics, and the quality criteria used in match-up process yields 68 matchups for MERIS (data from September 2003 to December 2005), 89 matchups for SeaWiFS (data from

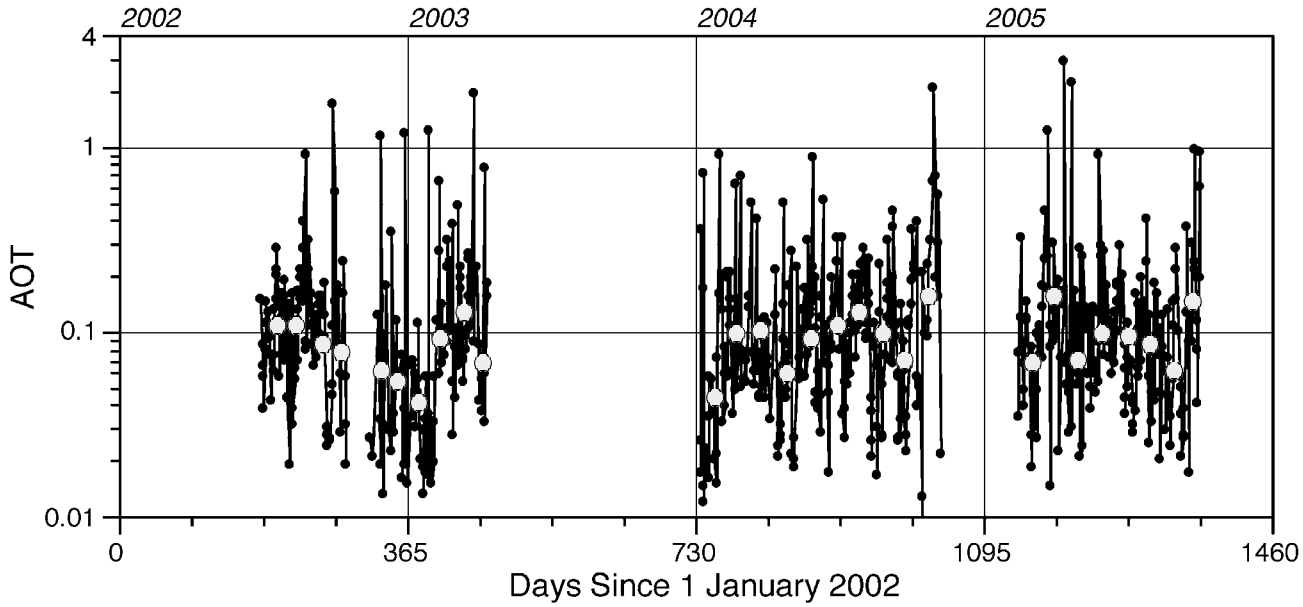

Fig. 29. The full time series of the AOT at the AERONET *Cap Ferrat* coastal site with monthly averages shown as the larger open circles. The corresponding calendar years are given along the top of the plot.

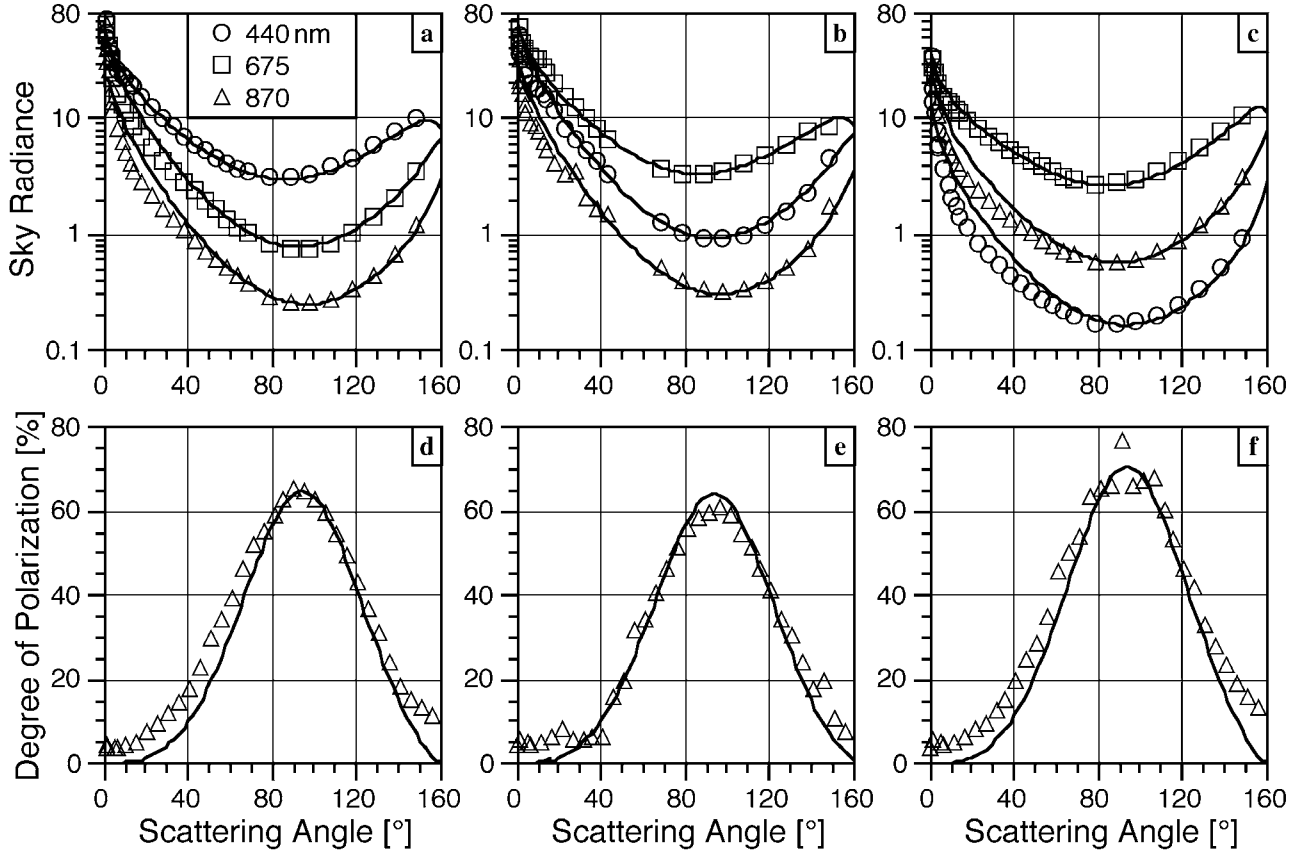

Fig. 30. Three examples of reconstructing sky radiances (in units of microwatts per square centimeter per nanometer per steradian) in the principal plane and at three wavelengths (curves), as compared to the direct measurements of the sun photometer (symbols), from which the inversion procedure (Sect. 7.7) infer an aerosol type: **a)** 11 July, **a)** 7 September, and **c)** 26 September 2002. The corresponding polarization rate at 870 nm is shown in panels **d**–**f**.

Table 8. The aerosol optical properties returned by the inversion algorithm for three days of measurements. These parameters were used in the computations presented in Fig. 30. The complex refractive index, $m_r - jm_i$, aerosol optical depth at 675 nm, and the Angström exponent, α, measured by the AERONET radiometer are presented along with the solar zenith angle, θ_s.

Year	*Date*	*Time* [GMT]	$m_r - jm_i$	$\tau_a(675)$	α	θ_s [°]
2002	11 July	1736	$1.44 - j0.0049$	0.0955	1.562	72.34
2002	7 September	1627	$1.41 - j0.00001$	0.1143	1.686	72.79
2002	26 September	1567	$1.51 - j0.0090$	0.0385	1.459	72.82

September 2003 to December 2004) and 65 matchups for MODIS-A (data from September 2003 to May 2005). The data used are a function of the satellite mission. For MERIS, level-2 1 km reduced resolution data processed by the MERIS Ground Segment Simulator (MEGS) prototype version 7.4.1 are used. For SeaWiFS, level-2 merged local area coverage (MLAC) data from reprocessing 5 (completed March 2005) are used, and for MODIS-A, level-2 global area coverage (GAC) data from reprocessing 1 (completed February 2005) are used.

The MERIS data provide the water-leaving radiance reflectance, ρ_w, defined as (again ignoring the spectral dependence for brevity):

$$\rho_w(\theta_v, \theta_s, \Delta\phi) \;=\; \pi \, \frac{L_W(\theta_v, \theta_s, \Delta\phi)}{E_s(\theta_s)}, \qquad (13)$$

where neither L_W nor E_d are normalized to a zenith Sun or to a nadir viewing angle. It is worth noting as well that the MERIS data have still not been vicariously calibrated.

The SeaWiFS and MODIS-A data provide the fully normalized water-leaving radiance, $\left[L_W(\lambda)\right]_{\rm N}$, which are defined (without the spectral dependence) as:

$$\left[L_W\right]_{\rm N} \;=\; \frac{L_W}{t_d(\theta_s)\cos\theta_s} \, \frac{\Re_0}{\Re(\theta', W)} \, {\rm fn}(f/Q), \qquad (14)$$

where $\Re$ is a geometrical factor accounting for all of the refraction and reflection effects at the air–sea interface, $\Re_0 = \Re(\theta' = 0)$, and fn(f/Q) provides the functional dependence on the bidirectional nature of the light field. The latter is defined as

$${\rm fn}(f/Q) \;=\; \frac{f_0(W, C_a)}{Q_0(W, C_a)} \left[\frac{f(\theta_s, W, C_a)}{Q(\theta_s, \theta', \Delta\phi, W, C_a)} \right]^{-1}, \qquad (15)$$

where C_a is the Chl a concentration, W is wind speed, Q is the ratio of upward irradiance to upwelling radiance (subscript 0 means for a Sun at zenith and a nadir view), f is a factor relating the irradiance reflectance R to the inherent optical properties, and other symbols are describing the geometry of the problem. The transformations needed to derive fully compatible quantities between the satellite and the *in situ* measurements (i.e., accounting for the bidirectional nature of the light field) are not detailed here.

Concerning the water-leaving radiances or reflectances, results are displayed as scatterplots of the satellite-derived versus *in situ* measurements in Fig. 31 for MERIS, SeaWiFS, and MODIS-A (all wavelengths presented together). The associated statistics are provided separately for each wavelength, as well as for the full data set, in Tables 9–11, for MERIS, SeaWiFS, and MODIS-A, respectively.

The overall agreement between the satellite-derived and the *in situ* reflectances or radiances is similar for the three satellites, and for SeaWiFS and MODIS-A, it is close to what has been already reported elsewhere. Consequently, a table-by-table discussion of the statistics within the tables is not presented, but some specific points are noted:

- The MERIS data products for the red bands (620, 665, and 681 nm) are overestimated by a factor of about two, which is not seen for the other satellite data products;
- The MERIS data products for the blue wavelengths appear to be overestimated;
- The MODIS-A data products exhibit the smallest amount of dispersion around the 1:1 line; and
- The SeaWiFS and MODIS-A data products exhibit a slight underestimation in the blue domain (the slopes of the overall fit are slightly less than 1).

The TChl a matchups for the three sensors are presented in Fig. 32, where all available comparison points are shown regardless of the environmental conditions, and in Fig. 33, where only a quality-assured subset of data is shown based on the criteria used for the reflectance matchups. The number of match-up points in Figures 32 and 33, respectively, are 34 and 9 for MERIS, 52 and 14 for SeaWiFS, and 39 and 9 for MODIS-A.

10. VICARIOUS CALIBRATION

The TOA vicarious radiometric calibration is a challenging process, for which high-quality data from several sources have to be brought together, to form input to, and boundary conditions of, radiative transfer calculations. These calculations are supposed to provide the TOA radiances, which are compared to the same quantities as measured by the spaceborne sensor. The principle of this calibration is given below, before a tentative performance

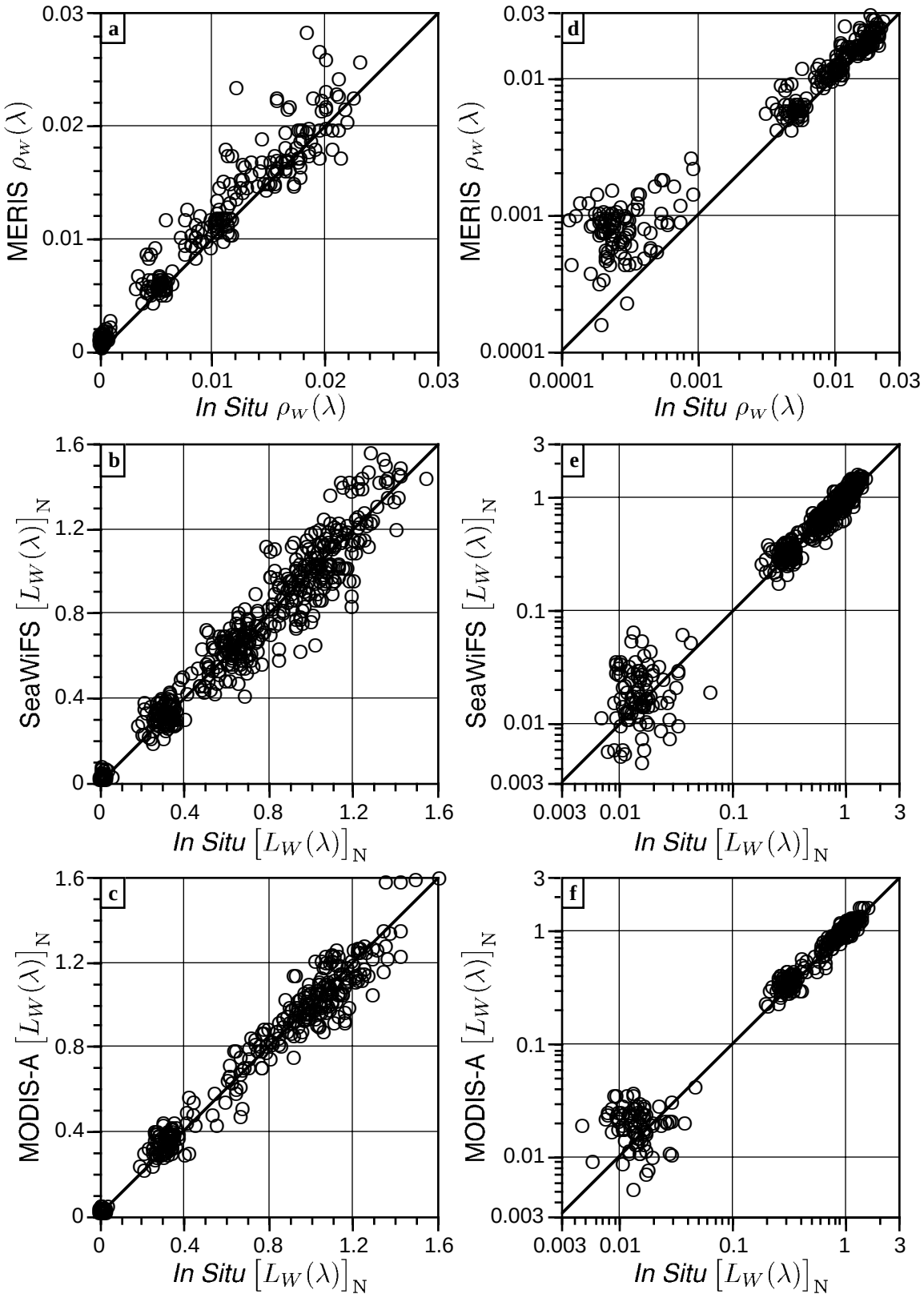

Fig. 31. Satellite matchups at the BOUSSOLE site for **a)** MERIS $\rho_w(\lambda)$ values (412, 443, 490, 510, 560, 670, and 683 nm); **b)** SeaWiFS $\left[L_W(\lambda)\right]_N$, values (412, 443, 490, 510, 555, and 670 nm); and **c)** MODIS-A $\left[L_W(\lambda)\right]_N$ values (412, 443, 488, 510, 551, 670, and 683 nm). The solid line is the 1:1 line. Logarithmic scales for panels **a**–**c** are shown in panels **d**–**f**, respectively, in order to magnify the low values in the red domain.

Table 9. The match-up statistics for MERIS. The statistical parameters include the relative percent difference (RPD) plus four linear fit parameters: the coefficient of determination, r^2; the slope, m; the y-intercept, y_0; and the root mean square (rms) error.

λ	*No.*	*Mean*	RPD	*Linear Fit Parameters*				*In Situ*		*Satellite*	
[nm]	*Pts.*	*Ratio*	[%]	r^2	m	y_0	*rms*	*Min.*	*Max.*	*Min.*	*Max.*
412	29	1.26	25.69	0.638	0.84	0.0055	0.00468	0.00512	0.02420	0.00760	0.02784
443	55	1.10	10.42	0.722	0.86	0.0033	0.00275	0.00415	0.02357	0.00615	0.02372
490	55	1.09	8.62	0.750	0.79	0.0037	0.00181	0.00448	0.01772	0.00621	0.01852
510	55	1.13	12.58	0.437	0.56	0.0053	0.00169	0.00496	0.01277	0.00653	0.01281
560	55	1.14	14.36	0.237	0.44	0.0036	0.00111	0.00332	0.00815	0.00401	0.00869
620	7	1.93	92.53	0.074	0.76	0.0008	0.00076	0.00051	0.00094	0.00070	0.00213
665	55	3.42	241.51	0.022	0.46	0.0008	0.00074	0.00013	0.00076	0.00029	0.00186
681	55	5.32	431.90	0.509	1.24	0.0007	0.00083	0.00001	0.00163	0.00033	0.00261
709	7	2.00	99.62	0.228	1.24	0.0002	0.00042	0.00013	0.00061	0.00007	0.00111
All	*373*			*0.938*	*1.02*	*0.0009*					

Table 10. The match-up statistics for SeaWiFS.

λ	*No.*	*Mean*	RPD	*Linear Fit Parameters*				*In Situ*		*Satellite*	
[nm]	*Pts.*	*Ratio*	[%]	r^2	m	y_0	*rms*	*Min.*	*Max.*	*Min.*	*Max.*
412	48	0.95	−5.10	0.770	1.16	−0.20	0.169	0.367	1.545	0.263	1.548
443	98	0.99	−0.96	0.795	0.96	0.03	0.119	0.280	1.430	0.314	1.525
490	98	1.00	−0.20	0.673	0.78	0.19	0.100	0.315	1.194	0.384	1.189
510	98	0.99	−1.49	0.403	0.57	0.25	0.078	0.335	0.848	0.359	0.796
555	98	1.01	1.08	0.123	0.37	0.19	0.054	0.187	0.498	0.173	0.436
670	95	1.37	36.70	0.026	0.22	0.02	0.014	0.007	0.065	0.004	0.061
All	*535*			*0.950*	*0.97*	*0.01*					

Table 11. The match-up statistics for MODIS-A.

λ	*No.*	*Mean*	RPD	*Linear Fit Parameters*				*In Situ*		*Satellite*	
[nm]	*Pts.*	*Ratio*	[%]	r^2	m	y_0	*rms*	*Min.*	*Max.*	*Min.*	*Max.*
412	42	0.95	−4.62	0.864	1.03	−0.06	0.120	0.405	1.605	0.282	1.590
443	85	0.98	−2.13	0.824	0.91	0.07	0.094	0.310	1.495	0.286	1.585
488	85	1.00	−0.10	0.795	0.79	0.19	0.069	0.354	1.174	0.372	1.228
551	85	1.08	8.31	0.242	0.59	0.15	0.049	0.196	0.380	0.208	0.432
667	84	1.48	48.44	0.003	0.06	0.02	0.010	0.005	0.048	0.005	0.040
All	*381*			*0.975*	*0.96*	*0.02*					

budget is proposed and preliminary results are shown for the MERIS sensor.

10.1 Principles

Two main *vicarious*† calibration paths exist to produce ocean color products of the desired accuracy, i.e., water-leaving radiances within an uncertainty of about 5% in the blue for an oligotrophic ocean (Gordon 1997, and Antoine and Morel 1999). The first one is usually referred to as *vicarious calibration*, and consists in forcing the satellite-derived water-leaving radiances to agree with a set of *in situ* water-leaving radiances (match-up analyses). A set of vicarious calibration coefficients is obtained, which is applied to the TOA radiances measured by the sensor. The second procedure, which is also an indirect (vicarious) calibration is sometimes referred to as a *vicarious radiometric calibration*, and consists in simulating the TOA signal that the sensor should measure under certain conditions, and to compare it to the measured signal.

One of the difficulties of the first type of vicarious calibration is that it is dependent upon the procedure used

† The *true*, direct, calibration in principle consists in measuring the signal from a well-known standard, and is performed before launch for spaceborne sensors. After launch, only indirect (*vicarious*) procedures are possible.

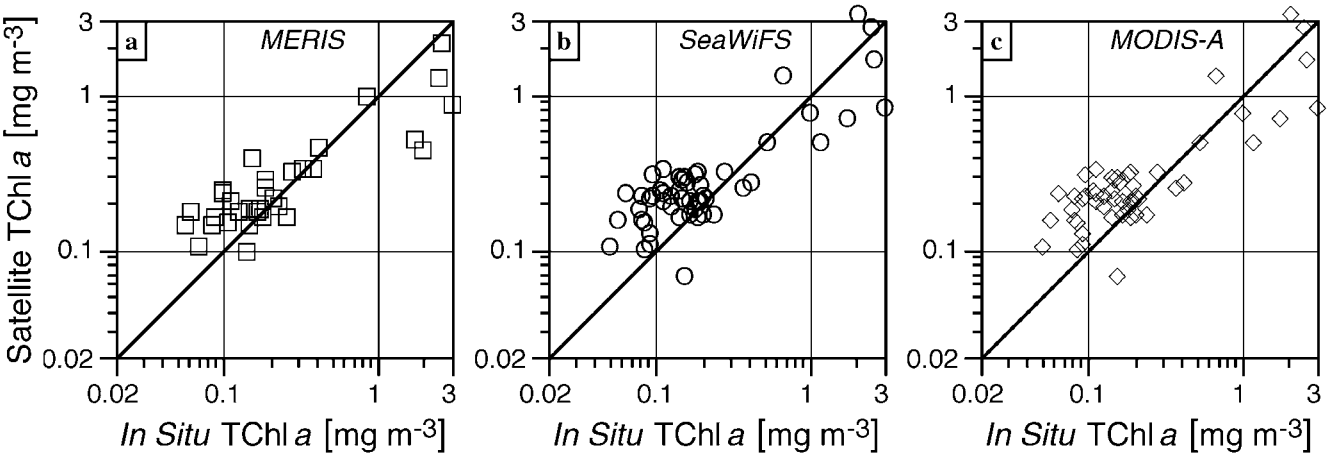

Fig. 32. *In situ* (HPLC) TChl *a* concentration matchups with respect to satellite-derived values at the BOUSSOLE site for **a)** MERIS ($N = 34$), **b)** SeaWiFS ($N = 52$), and **c)** MODIS-A ($N = 39$). The temporal coverage is from July 2001 to the end of 2005 for MERIS and MODIS-A, and 2004 for SeaWiFS.

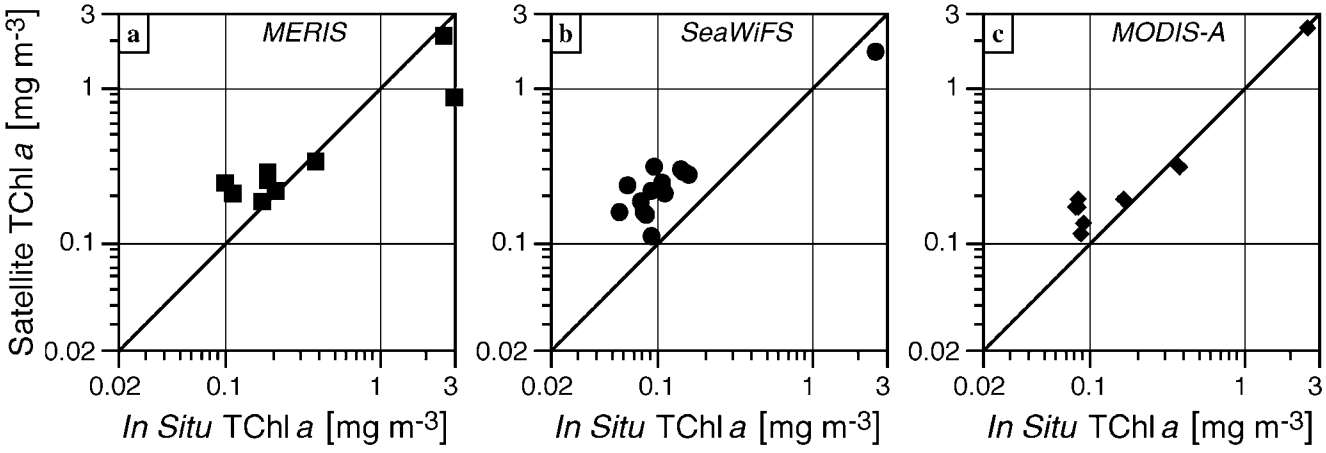

Fig. 33. The quality-assured *in situ* (HPLC) TChl *a* concentration matchups shown in Fig. 32 for **a)** MERIS ($N = 9$), **b)** SeaWiFS ($N = 14$), and **c)** MODIS-A ($N = 9$).

for the atmospheric correction of the TOA observations. Even if it is admittedly less dependent upon the selected set of *in situ* water-leaving radiances, these measurements also contribute to the final accuracy. Besides the fact that atmospheric measurements are not needed, the advantage of this technique is that the marine signals delivered by several sensors using different atmospheric correction algorithms can be cross-calibrated† provided the same set of *in situ* water-leaving radiances is used to perform the vicarious calibration (presently true for the SeaWiFS and MODIS-A sensors).

An inconvenience of the vicarious radiometric calibration is that it requires a set of *in situ* measurements which are usually difficult to collect, among other things, because a high accuracy is required. In addition to the in-water measurements of the water-leaving radiances, this data set includes sea state and atmospheric pressure, ozone concentration, aerosol optical thickness, aerosol type, and even aerosol vertical profile if the aerosols reveal to be absorbing. If this data set is successfully assembled, the advantage of the vicarious radiometric calibration is that it is independent of the atmospheric correction algorithms, so that the TOA signals of various sensors can be cross-calibrated. Then it is up to any user to apply its preferred atmospheric correction to these TOA signals. The marine signals in that case might be inconsistent if significant differences exist in the various atmospheric corrections.

The greatest difficulty of the vicarious radiometric calibration lies in the estimation of the aerosol optical thickness, phase function, and single scattering albedo. These parameters are accessible through the inversion of sun photometer measurements, yet uncertainties inevitably occur

† Except in situations where the atmosphere would be significantly different from the atmosphere present when performing the *in situ* measurements used for the vicarious calibration exercise.

when applying such methods, for example because of multiple scattering, perturbations from the ground reflectance, or uncertainties in the photometer calibration. Assembling all data needed for these vicarious calibration experiments are often compromised only because aerosol parameters are not accurate enough. The principle is illustrated on Fig. 34. A practical example is provided later on in Sects. 10.3 and 10.4.

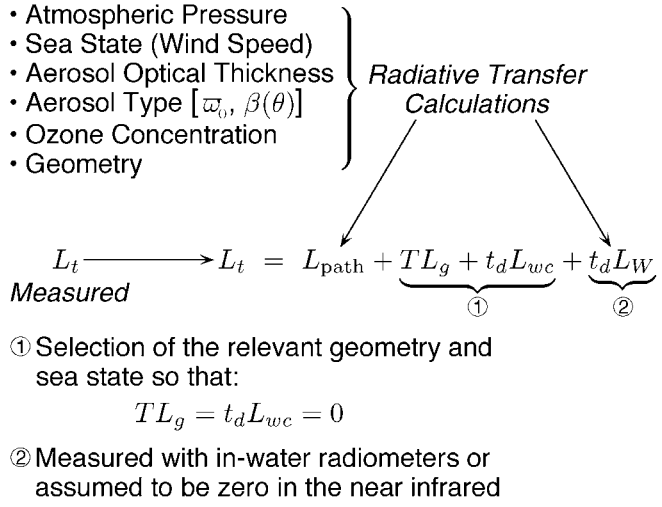

Fig. 34. The overall logic of the TOA vicarious radiometric calibration process. L_t is the total (TOA) radiance, L_g is the radiance contribution from sun glint, and L_{wc} is the radiance from white caps. The direct and diffuse atmospheric transmittances are denoted by T and t_d, respectively.

The Rayleigh scattering above clear waters method actually follows the same principle as the full radiometric vicarious calibration (the scheme displayed just above), but by using assumptions about, instead of measurements of, the various input parameters. This is particularly critical for the water-leaving radiances and the aerosol parameters. The final accuracy of this method cannot be better than that of the vicarious calibration procedure, except in a situation where the measurements used in the latter would be of very poor quality (or even erroneous).

10.2 Performance Budgets

It is in practice impossible to establish an *a priori* full performance budget, which should account for both unpredicted or unknown experimental sources of error (such as unidentified calibration deficiencies, difficulties encountered at sea, etc.) and theoretical limitations of the measurements themselves. The former are not totally known before starting the measurement sessions.

The budget presented below is, therefore, a tentative one, and any number provided in terms of percent error should be considered with caution. When the information necessary to confidently estimate the contribution of a given process to the error budget was missing or insufficiently known, this contribution has been assigned a somewhat optimistic value.

Each term that may impact the modeling of the TOA radiance (L_t), which is the sum of the atmospheric path radiance ($L_{\rm path}$) and of the product of the water-leaving radiance (L_W) by the atmospheric diffuse transmittance (t_d), is examined below. At the end, the uncertainties on all terms are considered as random, gaussian distributed, independent one of each other, so that the final error budget is computed as the square root of the sum of the squares of the individual error terms. The extent to which deviation from this hypothesis may impair the correctness of the final error budget has not been assessed.

The various uncertainty estimates discussed below, as well as the overall uncertainty budgets, are summarized in Tables 12 and 13.

Table 12. Theoretical and tentative uncertainty budget for vicarious calibration in the near infrared. In this case, L_W is assumed to be 0 (i.e., the wavelength is 865 nm in the near infrared).

Source of Uncertainty	u_{L_t}
AOT	2.00
Aerosol Type	5.00
Atmospheric Pressure	0.20
Sea Surface State	0.50
Ozone	0.00
Radiative Transfer	0.00
Overall Uncertainty	*5.41*

10.2.1 In-Water Measurements

The routine operations on the BOUSSOLE buoy should provide the measurements of E_d, E_u, and L_u (nadir) at 5 and 9 m. The basic operation consists of estimating the water-leaving radiance, L_W, from these in-water measurements, and in particular from L_u. Evaluation of above-water techniques for the measurement of L_W will also be tentatively set up (using a SIMBADA instrument), and will be examined later (Sect. 10.2.2). The uncertainty in L_u is estimated to be about 5% when carefully performing the measurements with well-calibrated instruments.

10.2.1.1 Extrapolation to Null Depth

Here the problem is to compute the diffuse attenuation coefficient for the radiance along the nadir direction, K_L, from the measurements performed at two depths on the buoy (nominally 5 and 9 m). Denoting this value as $K_L^{5,9}$, it is in principle used to compute the upwelling nadir radiance just below the surface, $L_u(0^-)$, through

$$L_u(0^-) \;=\; L_u(Z)\, e^{K_L^{5,9}(Z)}, \qquad (16)$$

where Z is about 5 m.

Table 13. Theoretical and tentative uncertainty budgets for in-water (left column), above-water (middle column), and Rayleigh scattering above clear water vicarious calibration (right column) experiments. For all three activities, L_W is 15% of L_t, u_{L_W} is the uncertainty expressed as a percentage of L_W, and u_{L_t} is the uncertainty expressed as a percentage of L_t.

In-Water *Uncertainty Source*	u_{L_W} [%]	u_{L_t} [%]	*Above-Water* *Uncertainty Source*	u_{L_W} [%]	u_{L_t} [%]	*Rayleigh Scattering* *Uncertainty Source*	u_{L_W} [%]	u_{L_t} [%]
Measurement of L_u	5.0	0.75	Measurement of L_W	10.0	1.50	Assumption about L_W†	30.0	4.50
Extrapolation to 0^+	3.0	0.45						
Bidirectionality	2.0	0.30	Bidirectionality	2.0	0.30			
Atmos. Transmittance	2.0	0.30	Atmos. Transmittance	2.0	0.30	Atmos. Transmittance	3.0	0.45
AOT		1.00	AOT		1.00	AOT Extrap. from NIR		2.00
Aerosol Type		2.00	Aerosol Type		2.00	Aerosol Type		5.00
Atmospheric Pressure		0.20	Atmospheric Pressure		0.20	Atmospheric Pressure		0.50
Sea Surface State		0.50	Sea Surface State		0.50	Sea Surface State		1.00
Ozone		0.50	Ozone		0.50	Ozone		0.50
Radiative Transfer		0.00	Radiative Transfer		0.00	Radiative Transfer		0.00
Overall Uncertainty		*2.55*	*Overall Uncertainty*		*2.82*	*Overall Uncertainty*		*7.14*

† With *a priori* knowledge of the area under examination.

Three important points intervene here: a) the intercalibration of the instruments at the two depths, which is assumed to be properly established; b) the correct estimation of the depth of the measurements†; and c) the adequacy of $K_L^{5,9}$ to perform the extrapolation of L_u from 5 m to just below the sea surface.

For clear waters (i.e., K_L about $0.02\,\mathrm{m}^{-1}$ in the blue), a large uncertainty of 1 m on the exact depth of measurement would lead to an error equal to e^{K_L}, i.e., a 2% uncertainty on the estimation of $L_u(0^-)$. Conversely, if it is assumed that Z is correctly estimated, an uncertainty of 10% on K_L would lead to an uncertainty equal to $e^{-0.1K_LZ}$, i.e., an uncertainty of 1% on $L_u(0^-)$ if Z is taken equal to 5 m (or 2% if Z is 10 m). These numbers become 2.5% and 5% for $K_L = 0.05$, i.e., for mesotrophic waters, also typical of the BOUSSOLE site when the TChl *a* concentration reaches about $0.3\,\mathrm{mg\,m}^{-3}$.

The attenuation coefficient for the upwelling nadir radiance is known to vary a bit within the very upper layers of the ocean (2–5 m), so that it is timely to examine whether or not $K_L^{5,9}$ remains the relevant coefficient to perform the extrapolation of L_u measured at 5 m to the 0^- level. The results of radiative transfer computations (Hydrolight code) show that a maximum difference of 5% exists between $K_L^{5,9}$ and $K_L^{0,5}$ for a TChl *a* concentration of $0.3\,\mathrm{mg\,m}^{-3}$ and a solar zenith angle of 45°, which translates into a maximum error in $L_u(0^-)$ of 1.25% when using $K_L^{5,9}$ to perform the extrapolation, and when K_L is about $0.05\,\mathrm{m}^{-1}$ (i.e., a TChl *a* concentration of $0.3\,\mathrm{mg\,m}^{-3}$). This error could be significantly reduced by correcting the values of $K_L^{5,9}$ following what can be learned from the results of radiative transfer computations.

At the end, assuming an average error of 3% on the estimation of $L_u(0^-)$, because of uncertainties in the extrapolation to the 0^- level, seems realistic.

10.2.1.2 Bidirectional and Transmission Effects

The in-water measurements provide the upwelling radiance at nadir, which has to be transformed into the upwelling radiance for the direction below water (θ') corresponding to an above-water zenith angle (θ), itself corresponding to a given viewing angle from the satellite, θ_v. The transformation is simply performed by ratioing the Q-factor at nadir to the Q-factor for the direction θ'. The uncertainty is here only in the relative values of Q at these two directions (in a match-up configuration, the difference between both will be minimized, i.e., $\theta < 20°$). In the blue domain, where the geometry of the light field does not depend very much on the particle phase function, the ratio of the Q-factors is probably correct to within a small amount, so a 2% uncertainty is assumed here.

The last step to get the water-leaving radiance is to multiply $L_u(\theta')$ by the expression $\big(1-\rho(\theta')\big)n_w^{-2}$, which accounts for the transmission across the interface, where $\rho(\theta')$ is the Fresnel reflection coefficient for the water–air interface and n_w is the refractive index of water. This step does not introduce any error as far as $\theta' < 20°$ and the sea surface is approximately flat (wind speed less than 15 kts).

10.2.1.3 Atmospheric Transmittance

The water-leaving radiance, L_W, has to be multiplied by the atmospheric diffuse transmittance, t_d, before it can

† The distance between the two depths of measurements is exactly known; the depth in question here is the depth Z from which the extrapolation to just below the surface is performed through $L_u(0^-) = L_u(Z)e^{K_LZ}$.

be added to the atmospheric path radiance. If the expression in use for computing t_d is considered valid (Wang 1999), the largest source of uncertainty is the aerosol optical thickness, which has a small impact on t_d. A factor of two change in τ_a (from 0.1 to 0.2), for example, translates as a 2% error on t_d at 443 nm, which results in a 2% uncertainty on the product $t_d L_W$.

In the green domain (e.g., at approximately 550 nm), another source of uncertainty is the ozone content of the atmosphere. When $\lambda = 550$ nm, the Rayleigh optical thickness is about 0.09 and the ozone optical thickness is approximately 0.03 for an ozone content of 350 DU. The uncertainty in $t_d(550)$ corresponding to an uncertainty of 50 DU would be of the order of 0.5% for viewing angles less than 45° (with, for instance, $t_d = e^{-(0.5\tau_r+\tau_{oz})/\cos\theta_v}$).

10.2.2 Above-Water Measurements

The uncertainty to which L_W is derived from the radiance measured above the sea surface (which includes L_W and surface reflection effects), can be considered as being on the order of about 10% (Hooker et al. 2002b and Hooker and Morel 2003), even when performed in well-controlled experimental conditions and in excellent environmental conditions. A careful implementation of the required metrology and proper removal of glint effects during data processing can reduce the uncertainties to the same order as the calibration uncertainty (Hooker et al. 2004) for above- or in-water radiometers.

Because above-water measurements are collected well above the sea surface, the uncertainty attached to the extrapolation of in-water measurements from depth to just beneath the surface does not enter into account. The same uncertainty is attached to the determination of bidirectional effects (Q factors), as well as to the calculation of the atmospheric diffuse transmittance.

10.2.3 Atmospheric Path Radiance

The uncertainties assoicated with computing the atmospheric path radiance are examined based on the uncertainties in the parameters used in the computations.

10.2.3.1 Atmospheric Pressure

Atmospheric pressure, P, is known to within 0.5% (i.e., 5 hPa). The changes in the path reflectance due to changes in P can be expressed as (Antoine and Morel 1998):

$$\frac{\Delta L_{\rm path}}{\Delta P} \;=\; 1 \;+\; \frac{\Delta P}{P}\eta_r, \qquad (17)$$

where η_r is the ratio of the Rayleigh optical thickness to the total (aerosol plus Rayleigh) optical thickness. In the worst case, where $\eta_r = 1$ (no aerosols), the uncertainty in P is transferred onto $L_{\rm path}$, but is actually a little less as shown by Gordon et al. (1988). It will also be less as soon as the AOT is not zero. A 0.2% uncertainty is assumed here when the atmospheric pressure is known (local measurements from the Meteo buoy near the BOUSSOLE site).

10.2.3.2 Sea Surface State

Quantification of the uncertainty due to an incorrect representation of the sea surface state is not really possible, and it would be probably useless because of the large uncertainties that remain in the parameterization of the surface wave slope probability distribution as a function of the wind speed. A tentative value of 0.5% is assumed here for the uncertainty introduced by these surface effects in the computation of L_t at the TOA level, with the underlying assumption that experiments are only performed for days of calm weather.

10.2.3.3 Aerosol Optical Thickness

The AOT should be known to less than 0.01 in absolute units (Fargion and Mueller 2000). The relative changes in $L_{\rm path}$ due to changes in AOT in the blue and green domains (i.e., around 440 and 550 nm, respectively), $\Delta L_{\rm path}/\Delta\tau_a$, are of the order of 0.1, e.g., as shown in Fig. 5 in Antoine and Morel (1998). An uncertainty of 0.01 in τ_a should, therefore, translate as an uncertainty of 0.001 in $L_{\rm path}$, which corresponds to about 1% of $L_{\rm path}(443)$ and 2% of $L_{\rm path}(550)$ when $\tau_a = 0.1$. The uncertainties are slightly less if τ_a is larger. These two values (1% and 2%) are adopted here, while noting that the corresponding numbers become 2–3% at 865 nm.

10.2.3.4 Aerosol Type

Retrieving the aerosol type, actually the aerosol volume scattering function (VSF) and single scattering albedo, is much more difficult than retrieving the AOT. The reasons for the difficulty are, a) the retrieval is based on inversion of sky radiance measurements, which are delicate to perform with the desired calibration constraints, and b) the inversion itself necessarily uses assumptions and is also subject to uncertainties.

In order to minimize the impact of uncertainties on the aerosol type, situations where the satellite data and external information (wind direction, independent observations, etc.) are both available are selected, in such a way that there is a high likelehood of the presence of maritime aerosols. Note that information about the relative humidity (RH) at the sea level will be available from the measurements of the Meteo buoy located in the vicinity of the BOUSSOLE mooring.

It is, therefore, considered here that the uncertainty is entirely due to the uncertainty on RH (the value itself or the vertical profile), for maritime aerosols conforming to the description of Shettle and Fenn (1979). From the results of radiative transfer simulations performed with these models, it appears that an uncertainty of 15% in the relative humidity (RH equal to 70% or 99% instead of 80%)

leads to a 2% uncertainty in the computation of $L_{\text{path}}(443)$ when $\tau_a < 0.1$ and $\theta_s < 40°$. This uncertainty is closer to 5% in the NIR ($\lambda = 865\,\text{nm}$).

Maintaining this level of uncertainty means that the vicarious calibration experiments have to be performed for τ_a values as low as possible and for high solar elevations (the minimum solar zenith angle at the BOUSSOLE site is about 21°).

10.2.3.5 Ozone Content

The importance of ozone content is investigated here in terms of its effect on the calculation of L_{path} (the other effect has been already considered in the calculation of the atmospheric diffuse transmittance). Ozone does not strongly affect the blue bands, which are the most critical for ocean color applications. A null impact on L_{path} is considered here.

For the green band, the problem is different because the ozone absorption is there at its maximum, with an optical thickness of about 0.03 at 550 nm when the total ozone amount is equal to 350 DU. The impact on L_{path} remains, however, extremely weak, i.e., less than a 5% difference between L_{path} for an atmosphere with a standard ozone amount (350 DU) and an ozone-free atmosphere. The typical uncertainties in the ozone amount (i.e., ±20 DU) should, therefore, be without significant impact on the computation of L_{path} (less than 0.5%).

The calibration uncertainty has been already considered when examining the uncertainty due to incorrect determination of the AOT and aerosol type. In principle, a valid radiative transfer code, when fed with accurate input, provides an exact answer in terms of radiance. It is, therefore, assumed that the modeling itself does not introduce any additional uncertainty.

10.2.4 Marine Contribution to Total Radiance

In clear oligotrophic waters, $L_W(\lambda)$ reaches a maximum value in the blue part of the spectral domain, and corresponds to about 15% of the TOA total radiance at 440 nm when the AOT is 0.05. Conversely, $L_W(\lambda)$ experiences minimum values in the green domain, and corresponds, for example, to about 5% of the TOA total radiance at 550 nm when the AOT is 0.3. Consequently, the various uncertainties in the estimation of $L_W(\lambda)$ as given above, in terms of percentages, correspond to uncertainties in $L_t(\lambda)$ ranging from 0.15% to 0.05%.

The various terms are summarized in the Tables 12 and 13, and are based on three different configurations concerning the estimation of the marine and atmospheric contributions to the TOA total radiance: in-water measurements of $L_u(\lambda)$ and measurements of the aerosol properties, above-water measurements of $L_W(\lambda)$ and measurements of the aerosol properties, and, finally (and tentatively), estimated values for the water-leaving radiance and aerosol properties (the so-called *Rayleigh scattering above clear water* technique).

10.2.5 Conclusions

In summary, the values in Tables 12 and 13 show that a 2–3% uncertainty in the simulation of the TOA total radiance can be reached in extremely favorable conditions. Considering the possible type and range of uncertainties that are possible in the entire exercise, a more realistic estimate of the accuracy to which the vicarious calibration can be performed would be approximately 5% in the visible part of the spectrum.

10.3 A Practical Example

The inversion algorithm suggested in Sect. 7.7 not only permits the characterization of the microphysical properties of the aerosols providing the refractive index, but also supplies knowledge about the aerosol phase function, which is a key parameter in the estimation of the atmospheric radiance and transmittance. The proposed algorithm can thus be used to lead a vicarious calibration of ocean color sensors.

The focus here is on the vicarious calibration of the MERIS NIR band at 865 nm. The sun photometer (Sects. 3.3, 4.3, and 5.3) is used to provide the necessary information about the aerosol properties. The procedure for the vicarious calibration is outlined as follows:

1. The aerosol refractive index is derived with the inversion algorithm.
2. The optical depth and Angström exponent are measured.
3. The TOA radiance is computed with the OSOA radiative transfer model for similar geometries of MERIS scenes on the basis of the aerosol optical properties, which is compared with the TOA signal recorded by MERIS.

Some restrictions and assumptions should be made, however, to apply the vicarious calibration technique:

4. The ocean is assumed to be black at 865 nm which is realistic in the Mediterranean Sea (open-ocean waters), so no marine signal is included in the computations.
5. The MERIS images are selected for geometrical conditions based on avoiding glint in the vicinity of the ground photometer.
6. Because of the proximity of the land in each image, the aerosol properties may exhibit a strong spatial variability at the land–ocean interface, so the aerosol model derived from the coastal sun photometer will be applicable to MERIS marine pixels only if the aerosols in the study area are spatially homogeneous (this constraint substantially reduced the number of available images for the calibration exercise).

Table 14. Computational aspects used in the OSOA radiative transfer model for the calculation of the top of atmosphere radiance in the MERIS geometry: τ_a at 675 nm (measured); α (measured); θ_s (in degrees); viewing zenith angle (in degrees); relative azimuth, $\Delta\phi$, between sun and satellite (in degrees); scattering angle, θ_d, (in degrees); aerosol model (complex refractive index $m_r - jm_i$) derived by the neural network. The time corresponding to MERIS overpass (t_M) and to the chosen sequence of principal plane measurements (t_P) is indicated in GMT (the year is 2002).

Date	t_M	t_P	τ_a	α	θ_s	θ_v	$\Delta\phi$	θ_d	$m_r - jm_i$
11 July	1000	0839	0.134	1.34	29.5	7.7	25.3	157.2	$1.46 - j0.009$
7 September	0935	1616	0.097	1.59	45.1	39.0	38.6	153.8	$1.41 - j0.000$
26 September	0938	1027	0.041	1.29	50.5	35.7	45.4	146.4	$1.55 - j0.004$
1 October	1021	1125	0.074	1.61	48.7	26.8	123.3	113.8	$1.52 - j0.011$
12 October	1021	1122	0.037	1.02	56.0	39.1	49.4	140.7	$1.57 - j0.008$

7. For each selected image, a subscene of 10×10 pixels is extracted far enough from the coastline (typically at a distance greater than 6 km) to avoid the adjacency effects on the radiance measured by the satellite sensor caused by the radiometrically *brighter* land (Santer and Schmechtig 2000).
8. After correction for the eccentricity of the Earth orbit, the TOA radiance is averaged over this subscene.

The inversion algorithm is applied on ground-based measurements collected at the time of the satellite overpass (around 1000 GMT for the Villefranche site) so the simulated radiance is consistent with MERIS data. Nevertheless, occasionally measurements are not available at the time of overpass; either they are missing or of bad quality. In such situations, the aerosol model derived from the inversion of the closest (in time) measurements of satellite overpass is used to reconstruct the TOA signal. This is possible as long as stable conditions are observed during the day. The daily variation of the Angström exponent is used to check this assumption.

10.4 Preliminary Results

Table 14 lists the computational aspects used in the OSOA model (geometry, aerosol refractive index, and optical depth) to predict the TOA radiance corresponding to MERIS observations. Only five matchups were available at the time of this preliminary analysis, depending on the quality of ground measurements and MERIS scenes. It should be noted that on 7 September 2002, the ground measurements made on the morning showed questionable data. Because $\tau_a(675)$ and α were stable all along this day—$\tau_a(675)$ varied from 0.097 to 0.119, and α varied from 1.45 to 1.69—the aerosol model derived from the measurements collected at the end of the day (at 1616 GMT) was used, because it includes the maximum value of the scattering angle (150°).

Table 15 presents a comparison between MERIS TOA radiances and OSOA calculations. The agreement is very good and remains below 5%. Gordon (1998) showed that for a given absolute calibration uncertainty in the NIR domain, the calibration error progressively decreases with decreasing wavelength. More recently, Wang and Gordon (2002) demonstrated that a calibration uncertainty of ±15% at 865 nm leads to an acceptable calibration uncertainty smaller than 3% at 412 nm. The results presented here are, therefore, within the accuracy requirements for the NIR band. Those results are still preliminary, however, because the number of available match-up data is not significant enough to draw rigorous conclusions about the MERIS calibration.

Table 15. The comparisons between the TOA radiances computed from OSOA radiative transfer calculations (L_O) or from MERIS (L_M) at 865 nm (expressed in units of $\mathrm{mW\,m^{-2}\,nm^{-1}\,sr^{-1}}$). The relative difference, $\Delta L/L$, corresponds to the ratio $(L_M - L_O)/L_M$.

Date	L_M	L_O	$\Delta L/L$ [%]
11 Jul.	4.4248	4.2194	4.64
7 Sep.	4.2832	4.4165	−3.11
26 Sep.	2.7727	2.8420	−2.50
1 Oct.	2.7479	2.7362	0.42
12 Oct.	2.7550	2.7337	0.77

As a future activity, the vicarious calibration method will be extended to the visible bands. In the visible part of the spectrum, the marine signal is not equal to zero, so the additional difficulty will be to get simultaneous in-water radiometric measurements in order to reconstruct the total TOA radiances as the sum of the atmospheric signal (calculated using the same technique as the NIR band) and the marine signal multiplied by a diffuse transmittance. To achieve this task, the continuous record collected by the BOUSSOLE buoy will provide the needed information on the signal exiting the water and will increase the number of matchups needed to perform a relevant vicarious calibration of MERIS.

Acknowledgments

The BOUSSOLE project was established thanks to the work of numerous individuals, as well as the support and funding of several agencies and institutions. The latter are listed in the foreword of this report. Specifically, the following contracts are acknowledged: CNES (the French space agency) provided funds through the *Terre Atmosphère Ocean Biosphère* and *Terre Océan Surfaces Continentales et Atmosphère* scientific committees, ESA through the European Space Research and Technology Center contract 14393/00/NL/DC, including contract change notices #1, #2, and #3, European Space Research Institute through contract 17286/03/I-OL, and NASA through a Letter of Agreement. Funding was also obtained from the French *Commission Spécialisée Océan Atmosphère* committee and the *Observatoire Océanologique de Villefranche*. INSU provided ship time for the monthly cruises.

The crews and captains of the following ships are also warmly thanked for their help at sea: the *Castor-02* from the Fosevel Marine company (buoy and mooring operations), the INSU R/V *Téthys-II* (regular monthly cruises), and the *GG-IX* from the Samar company (on demand short operations on site). Pilots and crew members of the Valair and Commerçair helicopter companies are also thanked for their willingness in accomplishing survey missions above the BOUSSOLE site. Emmanuel Bosc, Maria Vlachou, Guillaume Lecomte, who have occasionally helped in collecting the SIMBADA data, are also acknowledged.

The French institute IFREMER and the Norwegian MARINTEK company are also thanked for their help and fairness in the engineering studies that were ordered to them after the major failure of the first buoy in spring of 2002.

The data that are collected for several years near the BOUSSOLE site by the French weather forecasting agency, Meteo France, and which are provided in near-real time on the Internet, have been of great help in the day-to-day management of the monthly cruises, as well as in the analysis of the buoy behavior.

Two companies have contributed signifcantly to the BOUSSOLE project: ACRI-in/Genimar (Sophia Antipolis, France) contributed to the buoy conception, and Satlantic Inc. (Halifax, Canada) was responsible for the buoy centralized acquisition system and the radiometers. Their help is specifically acknowledged here.

Glossary

AC-9	Absorption and Attenuation Meter
AC-9+	Absorption and Attenuation Meter (with data handling)
AERONET	Aerosol Robotic Network
AOP	Apparent Optical Property
AOPEX	Advanced Optical Properties Experiment
AOT	Aerosol Optical Thickness
ARGOS	Not an acronym, but the name given to the data collection and location system on the NOAA operational satellites.
ASCII	American Standard Code for Information Interchange
BOUSSOLE	*Bouée pour l'acquisition de Séries Optiques à Long Terme* (buoy for the acquisition of a long-term optical series).
C-star	WETLabs transmissometer
CDOM	Colored Dissolved Organic Matter
CE-317	CIMEL Electronique (sun photometer model) 317
CE-318	CIMEL Electronique (sun photometer model) 318
CERT	Calibration Evaluation and Radiometric Testing
CIMEL	Not an acronym, but the name of a French company manufacturing sun photometers.
CNES	*Centre National des Etudes Spatiales* (French space agency).
CNRS	*Centre National de la Recherche Scientifique* (French national center for scientific research).
CoASTS	Costal Atmosphere and Sea Time Series
ComPACT	Compact Portable Advanced Characterization Tank
CTD	Conductivity, Temperature, and Depth
CZCS	Coastal Zone Color Scanner
DACNet	Data Aquisition and Control Network
DAS	Data Acquisition Sequence
DATA-100	(Satlantic) Data (acquisition series) 100 (unit)
DCM	Deep Chlorophyll Maximum
DHI	Not an acronum, but the name of the DHI Water and Environment Institute in Denmark.
DOC	Dissolved Organic Carbon
DP	Diagnostic Pigment
DUT	Device Under Test
DYFAMED	*Dynamique des Flux Atmosphériques en Méditerranée* (dynamics of atmospheric fluxes in the Mediterranean).
ECO-BB3	Three-channel backscattering (meter)
ESA	European Space Agency
EZ-III	Compass and two-axis tilt sensor
FEL	Not an acronym, but a lamp designator.
GAC	Global Area Coverage
GF/F	Not an acronym, but a specific type of glass fiber filter manufactured by Whatman.
GMT	Greenwich Mean Time
GPS	Global Positioning System
GUI	Graphical User Interface
HOBI Labs	Hydro-Optics, Biology, and Instrumentation Laboratories
HPLC	High Performance Liquid Chromatography
Hydroscat-II	HOBI Labs Hydroscat-II backscattering meter
ID	Identification
IFREMER	*Institut Français de Recherce pour l'Exploitation de la Mer* (French research institute for exploitation of the sea)
INSU	*Institut National des Sciences de l'Univers* (French national institute of sciences of the universe).
IOCCG	International Ocean Color Coordinating Group
IOP	Inherent Optical Property
IR	Infrared
JGOFS	Joint Global Ocean Flux Study
L19	(Perkin Elmer) Lambda 19 (spectrometer)
LCD	Liquid Crystal Display
LED	Light-Emitting Diode
LOV	*Laboratoire d'Océanographie de Villefranche* (Oceanographic Laboratory of Villefranche)

MARINTEK Marine Technology Research Institute
MEGS MERIS Ground Segment Simulator
MERIS Medium Resolution Imaging Spectrometer
MINItracka Not an acronym, but a fluorometer manufactured by Chelsea Company.
MLAC Merged Local Area Coverage
MOBY Marine Optical Buoy
MODIS Moderate Resolution Imaging Spectroradiometer
MODIS-A MODIS instrument on the Aqua satellite.
MVDS Multichannel Visible Detector System

NASA National Aeronautics and Space Administration
NIR Near-Infrared
NIST National Institute of Standards and Technology
NOAA National Oceanic and Atmospheric Administration

OCI-200 Satlantic Ocean Color Irradiance-200 series (sensor)
OCI-1000 Satlantic Ocean Color Irradiance-1000 series (sensor)
OCR-200 Satlantic Ocean Color Radiance-200 series (sensor)
OSOA *Ordres Successifs Océan Atmosphére* (ocean atmosphere successive orders)

PAR Photosynthetically Available Radiation
PARASOL Polarization and Anisotropy of Reflectances for Atmospheric Sciences coupled with Observations from a Lidar
PC Personal Computer
POLDER Polarization and Directionality of the Earth Reflectance
PROSOPE *Productivité des Systèmes Océaniques Pélagiques* (productivity of pelagic oceanic systems)

R/V Research Vessel
RAM Random Access Memory
RH Relative Humidity
rms Root Mean Square

SBE Seabird Electronics
SCOR Scientific Committee for Oceanographic Research
SeaHARRE SeaWiFS HPLC Analysis Round-Robin Experiment
SeaWiFS Sea-viewing Wide Field-of-view Sensor
SIMBAD Satellite Validation for Marine Biology and Aerosol Determination
SIMBADA Second-generation SIMBAD
SIMBIOS Sensor InterComparison and Merger for Biogeochemical Studies
SIRREX SeaWiFS Intercalibration Round-Robin Experiment
SMSR SeaWiFS Multichannel Surface Reference
SPMR SeaWiFS Profiling Multichannel Radiometer
SQM SeaWiFS Quality Monitor
SQM-II Second generation SQM
SST Sea Surface Temperature
STAM Satlantic Telemetry Acquisition Manager

TOA Top of Atmosphere
TSM Total Suspended Matter

UPMC *Université Pierre et Marie Curie* (translated as University of Pierre and Marie Curie)
UV Ultraviolet

VSF Volume Scattering Function

WCF WETLabs CDOM Fluorometer
WETLabs Western Environmental Technology Laboratories

Symbols

$a(\lambda)$ The spectral absorption coefficient.
$a_d(\lambda)$ The spectral absorption coefficient for detritus.
$a_p(\lambda)$ The spectral absorption coefficient for all particles.
$a_\phi(\lambda)$ The spectral absorption coefficient for phytoplankton.

$b(\lambda)$ The spectral scattering coefficient.
$b_b(\lambda)$ The spectral backscattering coefficient.

$c(\lambda)$ The spectral attenuation coefficient.
C_a The chlorophyll a concentration.

$E_d(\lambda)$ The spectral downward irradiance.
$E_s(\lambda)$ The spectral downward irradiance above the sea surface.
$E_u(\lambda)$ The spectral upward irradiance.

f The f-factor $(R/(b_b/a))$.

$K_d(\lambda)$ The spectral diffuse attenuation coefficient for downward irradiance.
$K_L(\lambda)$ The spectral diffuse attenuation coefficient for upwelling radiance.
$K_u(\lambda)$ The spectral diffuse attenuation coefficient for upward irradiance.

L_g The radiance due to sun glint at the TOA.
$L_{\mathrm{path}}(\lambda)$ The spectral path radiance at the TOA.
L_t The total radiance at the TOA.
$L_u(\lambda)$ The spectral upwelling radiance.
$L_W(\lambda)$ The spectral water-leaving radiance.
$[L_W(\lambda)]_{\mathrm{N}}$ The spectral normalized water-leaving radiance.
L_{wc} The radiance due to white caps at the TOA.

m The slope of a linear regression fit.
m_i The imaginary part of the complex refractive index of aerosols.
m_r The real part of the complex refractive index of aerosols.

n_w The refractive index of sea water.

P The atmospheric pressure.

$Q(\lambda)$ The spectral Q-factor (E_u/L_u).
Q_n The Q-factor at nadir $(\theta' = 0^\circ)$.

$\bar{r}$ The average reflection coefficient for upward irradiance from below the sea surface.
r^2 The regression coefficient of determination.
R The irradiance reflectance.
$\Re(\theta')$ A geometrical factor accounting for all refraction and reflection effects at the air–sea interface.
$\Re_0$ $\Re(\theta' = 0)$.
r_d The radius of the SPMR radiometer.

S Salinity.

T The total transmittance along a pixel-to-satellite sensor path.

t_d The diffuse transmittance along a pixel-to-satellite sensor path.

$[\mathrm{TChl}\,a]$ The total chlorophyll a concentration.

y_0 The y-intercept of a linear regression fit.

z Depth.

α The aerosol Angström exponent.

$\Delta\phi$ The relative azimuth difference angle.

η_r The ratio of the Rayleigh optical thickness to the total (i.e., aerosol plus Rayleigh) optical thickness.

θ' The in-water refracted viewing angle $\sin^{-1}\theta_v/1.34$.

θ_d The scattering angle.

θ_s The solar zenith angle.

θ_v The satellite viewing zenith angle.

λ Wavelength.

$\bar{\rho}$ The average reflection coefficient for downward irradiance across the air–sea interface.

$\rho(\theta)$ The Fresnel reflection coefficient for incident angle θ.

τ_a Aerosol optical thickness.

References

Aiken, J., D.G. Cummings, S.W. Gibb, N.W. Rees, R. Woodd-Walker, E.M.S. Woodward, J. Woolfenden, S.B. Hooker, J-F. Berthon, C.D. Dempsey, D.J. Suggett, P. Wood, C. Donlon, N. Gonzalez-Benitez, I. Huskin, M. Quevedo, R. Barciela-Fernandez, C. de Vargas, and C. McKee, 1998: AMT-5 Cruise Report. *NASA Tech. Memo. 1998–206892, Vol. 2,* S.B. Hooker and E.R. Firestone, Eds., NASA Goddard Space Flight Center, Greenbelt, Maryland, 113 pp.

Antoine, D., and A. Morel, 1998: Relative importance of multiple scattering by air molecules and aerosols in forming the atmospheric path radiance in the visible and near-infrared parts of the spectrum. *Appl. Opt.,* **37,** 2,245–2,259.

——, and ——, 1999: A multiple scattering algorithm for atmospheric correction of remotely-sensed ocean colour (MERIS instrument): Principle and implementation for atmospheres carrying various aerosols including absorbing ones. *Int. J. Remote Sens.,* **20,** 1,875–1,916.

Avril, B., 2002: DOC dynamics in the northwestern Mediterranean Sea. *Deep-Sea Res. II,* **49,** 2,163–2,182.

Bailey, S.W., C.R. McClain, P.J. Werdell, and B.D. Schieber, 2000: Normalized water-leaving radiance and chlorophyll *a* match-up analyses. *NASA Tech. Memo. 2000–206892, Vol. 10,* S.B. Hooker and E.R. Firestone, Eds., NASA Goddard Space Flight Center, Greenbelt, Maryland, 45–52.

Barlow, R., H. Sessions, N. Silulwane, H. Engel, S.B. Hooker, J. Aiken, J. Fishwick, V. Vicente, A. Morel, M. Chami, J. Ras, S. Bernard, M. Pfaff, J.W. Brown, and A. Fawcett, 2003: BENCAL Cruise Report. *NASA Tech. Memo. 2003–206892, Vol. 27,* S.B. Hooker and E.R. Firestone, Eds., NASA Goddard Space Flight Center, Greenbelt, Maryland, 64 pp.

Barnard, A.H., J.R. Zaneveld, and W.S. Pegau, 1999: *In situ* determination of the remotely sensed reflectance and the absorption coefficient: Closure and inversion. *Appl. Opt.,* **38,** 5,108–5,117.

Berthon, J-F., G. Zibordi, J.P. Doyle, S. Grossi, D. van der Linde, and C. Targa, 2002: Coastal Atmosphere and Sea Time Series (CoASTS), Part 2: Data Analysis. *NASA Tech. Memo. 2002–206892, Vol. 20,* S.B. Hooker and E.R. Firestone, Eds., NASA Goddard Space Flight Center, Greenbelt, Maryland, 25 pp.

Boss, E., and W.S. Pegau, 2001: The relationship of light scattering at an angle in the backward direction to the backscattering coefficient. *Appl. Opt.,* **40,** 5,503–5,507.

Bricaud, A., and D. Stramski, 1990: Spectral absorption coefficients of living phytoplankton and nonalgal biogenous matter: A comparison between the Peru upwelling area and the Sargasso Sea. *Limnol. Oceanogr.,* **35,** 562–582.

Chami, M., R. Santer, and E. Dilligeard, 2001: Radiative transfer model for the computation of radiance and polarization in an ocean-atmosphere system: Polarization properties of suspended matter for remote sensing. *Appl. Opt.,* **40,** 2,398–2,416.

Clark, D.K., H.R. Gordon, K.J. Voss, Y. Ge, W. Broenkow, and C. Trees, 1997: Validation of atmospheric correction over the oceans. *J. Geophys. Res.,* **102,** 17,209–17,217.

——, M.A. Yarbrough, M. Feinholz, S. Flora, W. Broenkow, Y.S. Kim, B.C. Johnson, S.W. Brown, M. Yuen, and J.L. Mueller, 2003: "MOBY, a Radiometric Buoy for Performance Monitoring and Vicarious Calibration of Satellite Ocean Color Sensors: Measurement and Data Analysis Protocols." In: Ocean Optics Protocols for Satellite Ocean Color Sensor Validation, Rev. 4, Vol. VI, *NASA Tech. Memo. 2003–211621,* NASA Goddard Space Flight Center, Greenbelt, Maryland, 3–34.

Claustre, H., A. Morel, S.B. Hooker, M. Babin, D. Antoine, K. Oubelkheir, A. Bricaud, K. Leblanc, B. Quéguiner, and S. Maritorena, 2002: Is desert dust making oligotrophic waters greener? *Geophys. Rev. Lett.,* **29,** 107-1–107-4.

Copin-Montegut, G., and B. Avril, 1993: Vertical distribution and temporal variation of dissolved organic carbon in the North-Western Mediterranean Sea. *Deep-Sea Res.,* **40,** 1,963–1,972.

Deschamps, P-Y., B. Fougnie, R. Frouin, P. Lecomte, and C. Verwaerde, 2004: SIMBAD: A field radiometer for satellite ocean-color validation. *Appl. Opt.,* **43,** 4,254–4,268.

Deuze J.L., M. Herman, and R. Santer, 1989: Fourier series expansion of the radiative transfer equation in the atmosphere-ocean system. *J. Quant. Spectrosc. Radiat. Transfer,* **41,** 483–494.

Dubovik, O., and M.D. King, 2000: A flexible inversion algorithm for retrieval of aerosol optical properties from Sun and sky radiance measurements. *J. Geophys. Res.,* **105,** 20,673–20,696.

——, A. Smirnov, B.N. Holben, M.D. King, Y.J. Kaufman, T.F. Eck, and I. Slutsker, 2000: Accuracy assessment of aerosol optical properties retrieval from AERONET sun and sky radiance measurements. *J. Geophys. Res.,* **105,** 9,791–9,806.

Fargion, G.S., and J.L. Mueller, 2000: Ocean Optics Protocols for Satellite Ocean Color Sensor Validation, Revision 2. *NASA Tech. Memo. 2001–209955,* NASA Goddard Space Flight Center, Greenbelt, Maryland, 184 pp.

Gordon, H.R., 1997: Atmospheric correction of ocean color imagery in the Earth observing system era. *J. Geophys. Res.,* **102,** 1,7081–1,7106.

——, 1998: In-orbit calibration strategy for ocean color sensors. *Remote Sens. Environ.,* **63,** 265–278.

——, J.W. Brown, and R.H. Evans, 1988: Exact Rayleigh scattering calculations for use with the Nimbus-7 Coastal Zone Color Scanner. *Appl. Opt.,* **27,** 862–871.

——, and G.C. Boynton, 1997: Radiance-Irradiance inversion algorithm for estimating the absorption and backscattering coefficients of natural waters: homogeneous waters. *Appl. Opt.,* **36,** 2,636–2,641.

——, and Ding, 1992: Self-shading of in-water optical instruments. *Limnol. Oceanogr.,* **37,** 491–500.

Gregg, W.W., and K.L. Carder, 1990: A simple spectral solar irradiance model for cloudless maritime atmospheres. *Limnol. Oceanogr.,* **35,** 1,657–1,675.

Hooker, S.B., W.E. Esaias, G.C. Feldman, W.W. Gregg, and C.R. McClain, 1992: An Overview of SeaWiFS and Ocean Color. *NASA Tech. Memo. 104566, Vol. 1,* S.B. Hooker and E.R. Firestone, Eds., NASA Goddard Space Flight Center, Greenbelt, Maryland, 24 pp., plus color plates.

——, and J. Aiken, 1998: Calibration evaluation and radiometric testing of field radiometers with the SeaWiFS Quality Monitor (SQM). *J. Atmos. Oceanic Technol.,* **15,** 995–1,007.

——, H. Claustre, J. Ras, L. Van Heukelem, J-F. Berthon, C. Targa, D. van der Linde, R. Barlow, and H. Sessions, 2000: The First SeaWiFS HPLC Analysis Round-Robin Experiment (SeaHARRE-1). *NASA Tech. Memo. 2000–206892, Vol. 14,* S.B. Hooker and E.R. Firestone, Eds., NASA Goddard Space Flight Center, Greenbelt, Maryland, 42 pp.

——, S. McLean, J. Sherman, M. Small, G. Lazin, G. Zibordi, and J.W. Brown, 2002a: The Seventh SeaWiFS Intercalibration Round-Robin Experiment (SIRREX-7), March 1999. *NASA Tech. Memo. 2002–206892, Vol. 17,* S.B. Hooker and E.R. Firestone, Eds., NASA Goddard Space Flight Center, Greenbelt, Maryland, 69 pp.

——, G. Lazin, G. Zibordi, and S. McLean, 2002b: An evaluation of above- and in-water methods for determining water-leaving radiances. *J. Atmos. Oceanic Technol.,* **19,** 486–515.

——, and A. Morel, 2003: Platform and environmental effects on above- and in-water determinations of water-leaving radiances. *J. Atmos. Oceanic Technol.,* **20,** 187–205.

——, G. Zibordi, J-F. Berthon, and J.W. Brown, 2004: Above-water radiometry in shallow, coastal waters. *Appl. Opt.,* **43,** 4,254–4,268.

——, L. Van Heukelem, C.S. Thomas, H. Claustre, J. Ras, L. Schlüter, J. Perl, C. Trees, V. Stuart, E. Head, R. Barlow, H. Sessions, L. Clementson, J. Fishwick, C. Llewellyn, and J. Aiken, 2005: The Second SeaWiFS HPLC Analysis Round-Robin Experiment (SeaHARRE-2). *NASA Tech. Memo. 2005–212785,* NASA Goddard Space Flight Center, Greenbelt, Maryland, 112 pp.

——, and G. Zibordi, 2005: Advanced methods for characterizing the immersion factor of irradiance sensors. *J. Atmos. Oceanic Technol.,* **22,** 757–770.

——, L. Van Heukelem, C.S. Thomas, H. Claustre, J. Ras, L. Schlüter, L. Clementson, J-F. Berthon, D. Van der Linde, R. Barlow, H. Sessions, J. Perl, and C. Trees, 2007: The Third SeaWiFS HPLC Analysis Round-Robin Experiment (SeaHARRE-3). *NASA Tech. Memo.,* NASA Goddard Space Flight Center, Greenbelt, Maryland, (in prep.).

IOCCG, 1998: Minimum Requirements for an Operational Ocean-Colour Sensor for the Open Ocean. *Reports Int. Ocean-Colour Coord. Group, Rept. No. 1,* Int. Ocean-Colour Coord. Group, Nova Scotia, Canada, 46 pp.

——, 1999: Status and plans for satellite ocean-colour missions: Considerations for complementary missions. *Reports Int. Ocean-Colour Coord. Group, Rept. No. 2,* Int. Ocean-Colour Coord. Group, Dartmouth, Canada, 47 pp.

Jeffrey, S.W., and M. Vesk, 1997: "Introduction to Marine Phytoplankton and Their Pigment Signatures." In: *Phytoplankton Pigments in Oceanography: Guidelines to Modern Methods.* S.W. Jeffrey, R.F.C. Mantoura, and S.W. Wright, Eds., UNESCO Publishing, Paris, 37–84.

Johnson, B.C., P-S. Shaw, S.B. Hooker, and D. Lynch, 1998: Radiometric and engineering performance of the SeaWiFS Quality Monitor (SQM): A portable light source for field radiometers. *J. Atmos. Oceanic Technol.,* **15,** 1,008–1,022.

Leathers, R.A., and N.J. McCormick, 1997: Ocean inherent optical property estimation from irradiances. *Appl. Opt.,* **36,** 8,685–8,698.

Loisel, H., and A. Morel, 1998: Light scattering and chlorophyll concentration in case 1 waters: A reexamination. *Limnol. Oceanogr.,* **43,** 847–858.

Maffione, R.A., and D.R. Dana, 1997: Instruments and methods for measuring the backward-scattering coefficient of ocean waters. *Appl. Opt.,* **36,** 6,057–6,067.

Marty, J.C., 2002: Preface to volume 49 number 11: DYFAMED time-series program (France JGOFS). *Deep-Sea Res. II,* **49,** 1,963–1,964.

McClain C.R., 1998: "SIMBIOS Background." In: C.R. McClain and G.S. Fargion, Eds., SIMBIOS Project 1998 Annual Report, *NASA Tech. Memo. 1999–208645,* NASA Goddard Space Flight Center, Greenbelt, Maryland, 1–2.

——, W.E. Esaias, W. Barnes, B. Guenther, D. Endres, S. Hooker, G. Mitchell, and R. Barnes, 1992: Calibration and Validation Plan for SeaWiFS. *NASA Tech. Memo. 104566, Vol. 3,* S.B. Hooker and E.R. Firestone, Eds., NASA Goddard Space Flight Center, Greenbelt, Maryland, 41 pp.

McLean, S., B. Schofield, G. Zibordi, M. Lewis, S. Hooker, and A. Weidemann, 1997: Field evaluation of anti-biofouling compounds on optical instrumentation. *SPIE Proc. Ocean Optics XIII,* **2963,** 708–713.

Mitchell, B.G., M. Kahru, J. Wieland, and M. Stramska, 2003: "Determination of Spectral Absorption Coefficients of Particles, Dissolved Material and Phytoplankton for Discrete Water Samples." In: Mueller, J.L., G.S. Fargion, and C.R. McClain, Eds., Ocean Optics Protocols for Satellite Ocean Color Sensor Validation. *NASA Tech. Memo. 2003–211621/Rev4-Vol.IV,* NASA Goddard Space Flight Center, Greenbelt, Maryland, 39–64.

Morel, A., and J-F. Berthon, 1989: Surface pigments, algal biomass profiles, and potential production of the euphotic layer: Relationships reinvestigated in view of remote-sensing applications. *Limnol. Oceanogr.,* **34,** 1,545–1,562.

——, and B. Gentili, 1991: Diffuse reflectance of oceanic waters: its dependance on sun angle as influenced by molecular scattering contribution. *Appl. Opt.,* **30,** 4,427–4,438.

——, and S. Maritorena, 2001: Bio-optical properties of oceanic waters: A reappraisal. *J. Geophys. Res.,* **106,** 7,763–7,780.

Mueller, J.L., and G.S. Fargion 2002: Ocean Optics Protocols for Satellite Ocean Color Sensor Validation, Revision 3. *NASA Tech. Memo. 2002–210004,* NASA Goddard Space Flight Center, Greenbelt, Maryland, 308 pp.

Nakajima, T., M. Tanaka, and T. Yamauchi, 1983: Retrieval of the optical properties of aerosols from aureole and extinction data. *Appl. Opt.,* **22,** 2,951–2,959.

——, G. Tonna, R. Rao, P. Boi, Y. Kaufman, and B. Holben, 1996: Use of sky brightness measurements from ground for remote sensing of particulate polydispersions. *Appl. Opt.,* **35,** 2,672–2,686.

Oubelkheir, K., H. Claustre, M. Babin, and A. Sciandra, 2005: The comparative bio-optical and biogeochemical properties of contrasted trophic regimes. *Limnol. Oceanogr.,* **50,** 1,795–1,809.

Rast, M., J.L. Bézy, and S. Bruzzi, 1999: The ESA Medium Resolution Imaging Spectrometer MERIS: A review of the instrument and its mission. *Int. J. Remote Sens.,* **20,** 1,681–1,702.

Robins, D.B., A.J. Bale, G.F. Moore, N.W. Rees, S.B. Hooker, C.P. Gallienne, A.G. Westbrook, E. Maranón, W.H. Spooner, and S.R. Laney, 1996: AMT-1 Cruise Report and Preliminary Results. *NASA Tech. Memo. 104566, Vol. 35,* S.B. Hooker and E.R. Firestone, Eds., NASA Goddard Space Flight Center, Greenbelt, Maryland, 87 pp.

Santer, R., and C. Schmechtig, 2000: Adjacency effects on water surfaces: Primary scattering approximation and sensitivity study. *Appl. Opt.,* **39,** 361–375.

——, and N. Martiny, 2003: Sky radiance measurements for ocean colour calibration-validation. *Appl. Opt.,* **42,** 896–907.

Shettle, E.P., and R.W. Fenn, 1979: Models for the aerosols of the lower atmosphere and the effects of humidity variations on their optical properties. *Environmental Research Papers, No. 676, AFGL–TR–79–0214,* Air Force Geophysics Laboratory, Hanscom AFB, Massachusetts, 31 pp.

Strickland, J.D.H., and T.R. Parsons, 1972: *A Practical Handbook of Sea Water Analysis.* Fish. Res. Board. Canada, 181–184.

Uitz, J., H. Claustre, A. Morel, and S.B. Hooker, 2006: Vertical distribution of phytoplankton communities in open ocean: An assessment based on surface chlorophyll. *J. Geophys. Res.,* **111,** C08005, doi:10.1029/2005JC003207.

Van Heukelem, L., and C.S. Thomas, 2001: Computer-assisted HPLC method development with applications to the isolation and analysis of marine phytoplankton pigments. *J. Chrom. A.,* **910,** 31–49.

Vidussi, F., H. Claustre, B.B. Manca, A. Luchetta, and J-C. Marty, 2001: Phytoplankton pigment distribution in relation to upper thermocline circulation in the eastern Mediterranean Sea during winter. *J. Geophys. Res.,* **106,** 19,939–19,956.

Wang, M., 1999: Atmospheric correction of ocean color sensors: computing atmospheric diffuse transmittance, *Appl. Opt.,* **38,** 451–455.

——, and H.R. Gordon, 2002: Calibration of ocean color scanners: How much error is acceptable in the near infrared? *Remote Sens. Environ.,* **82,** 497–504.

Zibordi, G., J-F. Berthon, J.P. Doyle, S. Grossi, D. van der Linde, C. Targa, and L. Alberotanza 2002a: Coastal Atmosphere and Sea Time Series (CoASTS), Part 1: A Tower-Based Long-Term Measurement Program. *NASA Tech. Memo. 2002–206892, Vol. 19,* S.B. Hooker and E.R. Firestone, Eds., NASA Goddard Space Flight Center, Greenbelt, Maryland, 29 pp.

——, D. D'Alimonte, D. van der Linde, J-F. Berthon, S.B. Hooker, J.L. Mueller, G. Lazin, and S. McLean, 2002b: The Eighth SeaWiFS Intercalibration Round-Robin Experiment (SIRREX-8), September–December 2001. *NASA Tech. Memo. 2002–206892, Vol. 21,* S.B. Hooker and E.R. Firestone, Eds., NASA Goddard Space Flight Center, Greenbelt, Maryland, 39 pp.

REPORT DOCUMENTATION PAGE

Form Approved
OMB No. 0704-0188

The public reporting burden for this collection of information is estimated to average 1 hour per response, including the time for reviewing instructions, searching existing data sources, gathering and maintaining the data needed, and completing and reviewing the collection of information. Send comments regarding this burden estimate or any other aspect of this collection of information, including suggestions for reducing this burden, to Department of Defense, Washington Headquarters Services, Directorate for Information Operations and Reports (0704-0188), 1215 Jefferson Davis Highway, Suite 1204, Arlington, VA 22202-4302. Respondents should be aware that notwithstanding any other provision of law, no person shall be subject to any penalty for failing to comply with a collection of information if it does not display a currently valid OMB control number.
PLEASE DO NOT RETURN YOUR FORM TO THE ABOVE ADDRESS.

1. REPORT DATE *(DD-MM-YYYY)*	2. REPORT TYPE	3. DATES COVERED *(From - To)*
29-12-2006	Technical Memorandum	

4. TITLE AND SUBTITLE

BOUSSOLE: A Joint CNRS-INSU, ESA, CNES, and NASA Ocean Color Calibration and Validation Activity

5a. CONTRACT NUMBER

5b. GRANT NUMBER

5c. PROGRAM ELEMENT NUMBER

6. AUTHOR(S)

David Antoine, Malik Chami, Hervé Claustre, Fabrizio d'Ortenzio, André Morel, Guislain Bécu, Bernard Gentili, Francis Louis, Joséphine Ras, Emmanuel Roussier, Alec J. Scott, Dominique Tailliez, Stanford B. Hooker, Pierre Guevel, Jean-François Desté, Cyril Dempsey and Darrell Adams

5d. PROJECT NUMBER

5e. TASK NUMBER

5f. WORK UNIT NUMBER

7. PERFORMING ORGANIZATION NAME(S) AND ADDRESS(ES)

Goddard Space Flight Center
Greenbelt, MD 20771

8. PERFORMING ORGANIZATION REPORT NUMBER

2007-00282-0

9. SPONSORING/MONITORING AGENCY NAME(S) AND ADDRESS(ES)

National Aeronautics and Space Administration
Washington, DC 20546-0001

10. SPONSORING/MONITOR'S ACRONYM(S)

11. SPONSORING/MONITORING REPORT NUMBER

TM-2006-214147

12. DISTRIBUTION/AVAILABILITY STATEMENT

Unclassified-Unlimited, Subject Category: 48
Report available from the NASA Center for Aerospace Information, 7115 Standard Drive, Hanover, MD 21076. (301) 621-0390

13. SUPPLEMENTARY NOTES

See title page for author affiliations.

14. ABSTRACT

This report presents the (BOUSSOLE) project, the primary objectives of which are to provide a long-term time series of optical properties in support of a) calibration and validation activities associated with satellite ocean color missions, and b) bio-optical research in oceanic waters. The following are included in the report: 1) an introduction to the rationale for establishing the project; 2) a definition of vicarious calibration and the specific requirements attached to it; 3) the organization of the project and the characteristics of the measurement site—in the northwestern Mediterranean Sea; 4) a qualitative overview of the collected data; 5) details about the buoy that was specifically designed and built for this project; 6) data collection protocols and data processing techniques; 7) a quantitative summary of the collected data, and a discussion of some sample results, including match-up analyses for the currently operational ocean color sensors, namely MERIS, SeaWiFS, and MODIS; and 8) preliminary results of the vicarious radiometric calibration of MERIS, including a tentative uncertainty budget. The results of this match-up analysis allow performance comparisons of various ocean color sensors to be performed, demonstrating the ability of the BOUSSOLE activity, i.e., combining a dedicated platform and commercial-off-the-shelf instrumentation, to provide data qualified to monitor the quality of ocean color products on the long term.

15. SUBJECT TERMS

BOUSSOLE, calibration and validation, ocean, Mediterranean Sea, buoy, MERIS

16. SECURITY CLASSIFICATION OF:			17. LIMITATION OF ABSTRACT	18. NUMBER OF PAGES	19b. NAME OF RESPONSIBLE PERSON
a. REPORT	b. ABSTRACT	c. THIS PAGE			Stanford B. Hooker
Unclassified	Unclassified	Unclassified	Unclassified	59	19b. TELEPHONE NUMBER *(Include area code)* (301) 286-9503